JPL D-15745 / CL# 25-2371
EOS MLS DRL 601 (part 1)
ATBD-MLS-01

Earth Observing System (EOS)
Microwave Limb Sounder (MLS)

An Overview of the EOS MLS Experiment

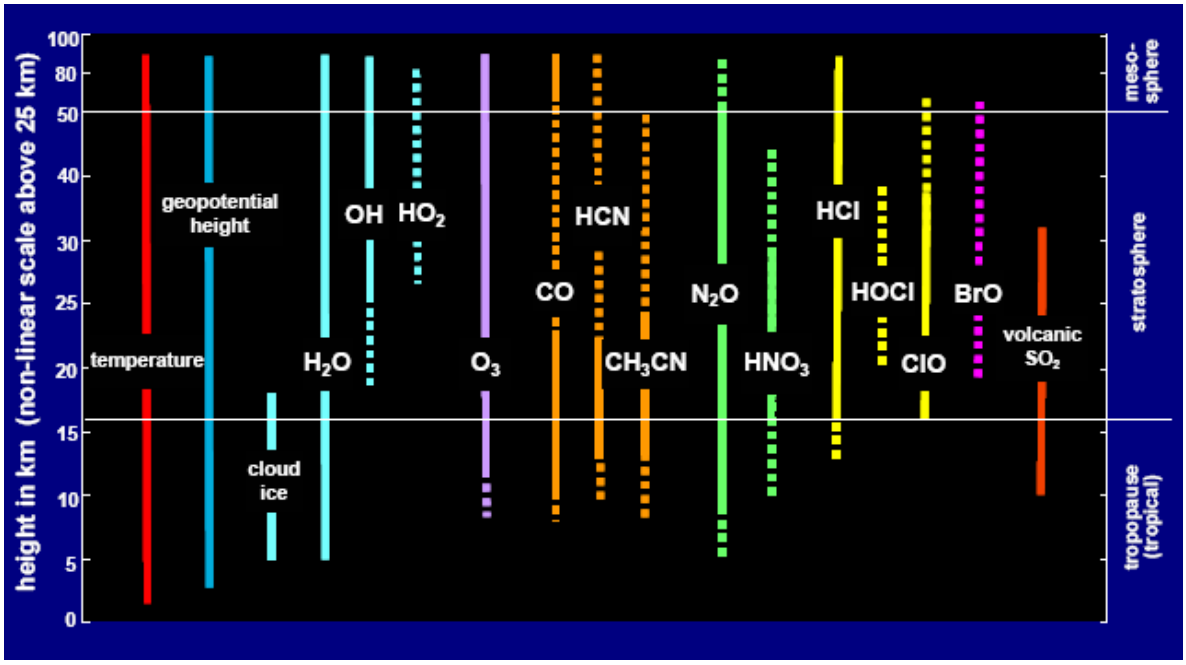

J.W. Waters, L. Froidevaux, R.F. Jarnot, W.G. Read, H.M. Pickett, R.S. Harwood, R.E. Cofield, M.J. Filipiak, D.A. Flower, N.J. Livesey, G.L. Manney, H.C. Pumphrey, M.L. Santee, P.H. Siegel, D.L. Wu

Version 2.0a: 2 September 2004 draft (changes accepted 9 June 2025)

Jet Propulsion Laboratory
California Institute of Technology
Pasadena, California 91109-8099

[this document is available at http://mls.jpl.nasa.gov]

The research was carried out at the Jet Propulsion Laboratory, California Institute of Technology, under a contract with the National Aeronautics and Space Administration (80NM0018D0004).

Release Record

Version	date released	comments
1.0	15 Jan 1999	Initial version
1.1	15 Oct 1999	Released following formal review of Version 1.0 by NASA board reviewing the EOS CHEM Algorithm Theoretical Basis Documents (ATBDs). This document received top grade of 'A' from the review board. The two recommendations by the board that apply to this document are italicized below, and are followed by the non-italicized response of the MLS team. • *A more complete (compared to that in the ATBD's) validation plan should be developed for the experiment.* This has been planned all along, and is being done. The EOS MLS data validation plan is a separate document. • *It might be prudent to use a prototype 240 GHz radiometer to make balloon or aircraft measurements prior to launch to ensure there are no surprises in this region of the spectrum*. Although this would possibly be a worthwhile activity, it is outside the scope of available resources and time. The lines to be measured by the 240 GHz radiometer are strong, and the spectral region has been sufficiently characterized in the laboratory that we feel the risk of surprises is acceptably small, and any that occur can be adequately accommodated after launch (as was done for UARS MLS in the case of volcanic SO_2, HNO_3, upper tropospheric water vapor and CH_3CN). No changes to the document were needed as a result of these recommendations. Changes from Version 1.0 are described below, and reflect expected progress since its release. General changes: (a) Titles for the categories of scientific objectives have been updated (in sections 1 and 4). Discussion of the objectives, in section 4, has been rewritten around key scientific questions. (b) The 'secondary' geophysical data products of Version 1.0 have now been set as standard data products, and 'secondary' products have been deleted. This resulted in updates to (1) overall schedule in section 1, (2) text and table 5-1 in section 5.1, and (3) section 8. (c) Updates made, as needed, for references and personnel. Formats of some tables changed. Relatively insignificant updates to some figures and tables. Additional specific changes: (1) Section 3: rearranged order of figures; added Figure 3-5 and text addressing stability of antenna reflectivity and its contribution to calibration stability. (2) Added sentences in first paragraph of section 5.1 stating the reasons for choosing the particular radiometers. (3) Table 5-5 giving estimated power, mass and data rate updated to the 'best estimates' presented at September 1999 MLS Critical Design Review, and current allocations have been added. These estimates are now well within the current allocations, but time-sharing is still identified to give 10% margin on power required at this stage of development. (4) Added sentences at end of section 7.1 stating that production data processing will be done at the MLS Science Investigator-led Processing System (SIPS) in Pasadena, California, and that the data will be transferred to the GSFC DAAC for archive and public distribution.

Release Record (continued)

Version	date released	comments
2.0	no formal release	Modifications since last version: (1) Replacing figures on title page with updated color versions, added co-authors (2) Changing name of 'CHEMISTRY' mission to 'Aura', following decision made by NASA (3) Updated and reorganized personnel tables, and moved to new separate section at end of document. (4) Removed Figure 5-3 from the previous versions, as the information in it was redundant with what was in the previous Figure 5-4. The previous Figure 5-3 is now Figure 5-3, and the following figures in section 5 were renumbered accordingly. (5) Updated the following figures: 3-2, 4-1, 5-1, 5-4, 5-6, 5-7 (including adding photographs of the MLS flight instrument), 6-2, 6-3, 7-1 (6) Updated the following tables: 5-2, 5-5, 8-1 (7) Combined material in Tables 8-2 through 8-5 (measurement precision examples) into a single table 8-2. (8) Updated chapter 4 with material from the EOS MLS Scientific Objectives document (9) Updated sections 7 and 8 on data processing and data products (10) Added table of acronyms (11) Updated references
2.0a	9 June 2025	Accepted changes from (never released) 2.0.

TABLE OF CONTENTS

1. Introduction

This document gives an overview of the Earth Observing System (EOS) Microwave Limb Sounder (MLS) experiment. It is intended to provide general information for a wide range of readers including MLS team members, additional scientists who may be using MLS data in their research, and programmatic officials. It also provides introductory and supporting information for the other EOS MLS Data Processing Algorithm Theoretical Basis Documents [Filipiak et al., 2004; Jarnot, et al., 2004a; Jiang, 2004; Livesey and Snyder, 2004; Read et al., 2004a; Schwartz et al., 2004; Wu and Jiang, 2004a]. These documents, and other information on MLS, are available at the MLS web site http://mls.jpl.nasa.gov.

EOS MLS is on the NASA EOS Aura satellite mission launched 15 July 2004, with an operational period planned to extend at least 5 years. The overall scientific objectives of the EOS MLS investigation are to provide information for

- determining if stratospheric ozone chemistry is recovering as expected,
- helping understand ozone and pollution in the upper troposphere, and
- improving knowledge of processes that affect climate variability.

MLS and the Aura mission contribute to the following three of the four areas of 'particular scientific and practical importance' identified in the US Global Change Research Program [Subcommittee on Global Change Research 1998]:

- changes in ozone, UV radiation, and atmospheric chemistry,
- decade-to-century climate change,
- seasonal-to-interannual climate variability.

MLS Data will be made publicly available through the NASA Goddard Space Flight Center (GSFC) Earth Science (GES) Distributed Active Archive Center (DAAC).

MLS is a collaboration between the United States and the United Kingdom. The California Institute of Technology Jet Propulsion Laboratory (JPL) has overall responsibility for its development and implementation. The University of Edinburgh (U of E) Institute of Atmospheric and Environmental Science has responsibility for aspects of data processing algorithm development, data validation, and scientific studies. Production processing of MLS data is by the 'Science Investigator-led Processing System' (SIPS) approach implemented by Raytheon Information Technology and Scientific Services (RITSS) under contract to the JPL MLS Science Team. The Aura mission is managed by GSFC; information on the mission is available at http://eos-aura.gsfc.nasa.gov.

Section 2 of this document gives the EOS MLS heritage, and section 3 gives a general description of the measurement technique. Section 4 describes the scientific objectives in detail. Section 5 describes the instrument, and section 6 the measurement coverage. Sections 7, 8 and 9 respectively, describe the data processing, data products, and data validation. Section 10 lists MLS personnel.

EOS MLS is a greatly enhanced version of the Upper Atmosphere Research Satellite (UARS) MLS experiment. It provides measurements of several stratospheric chemical species (O_3, H_2O, OH, HO_2, HCl, HOCl, ClO, BrO, N_2O, HNO_3, CO, HCN, CH_3CN, volcanically-injected SO_2), temperature and geopotential height. It measures upper tropospheric H_2O, cloud ice, temperature, O_3, CO, and – under enhanced conditions such as biomass burning events followed by lofting of chemicals into this region – HCN and CH_3CN. Attempts will be made to obtain N_2O, HNO_3 and HCl measurements down into the upper troposphere. Mesospheric temperature, H_2O, OH, HO_2, O_3, HCl, CO, HCN and geopotential height are measured.

Companion instruments to MLS on Aura are the infrared High Resolution Dynamics Limb Sounder (HIRDLS), the infrared Tropospheric Emission Spectrometer (TES), and the ultraviolet/visible Ozone Monitoring Instrument (OMI). HIRDLS provides unique high-resolution measurements that are important for improving understanding of the dynamics of the upper troposphere and stratosphere, and provides additional important stratospheric species not measured by MLS. TES provides unique global measurements of tropospheric chemical species, and additional stratospheric products. OMI measures total column ozone, continuing the long record from the Total Ozone Mapping Spectrometer (TOMS), along with information on the vertical distribution of ozone and other column measurements. The four Aura instruments synergistically provide a powerful set of measurements for understanding atmospheric global change. Figure 1-1 shows the suite of Aura measurements.

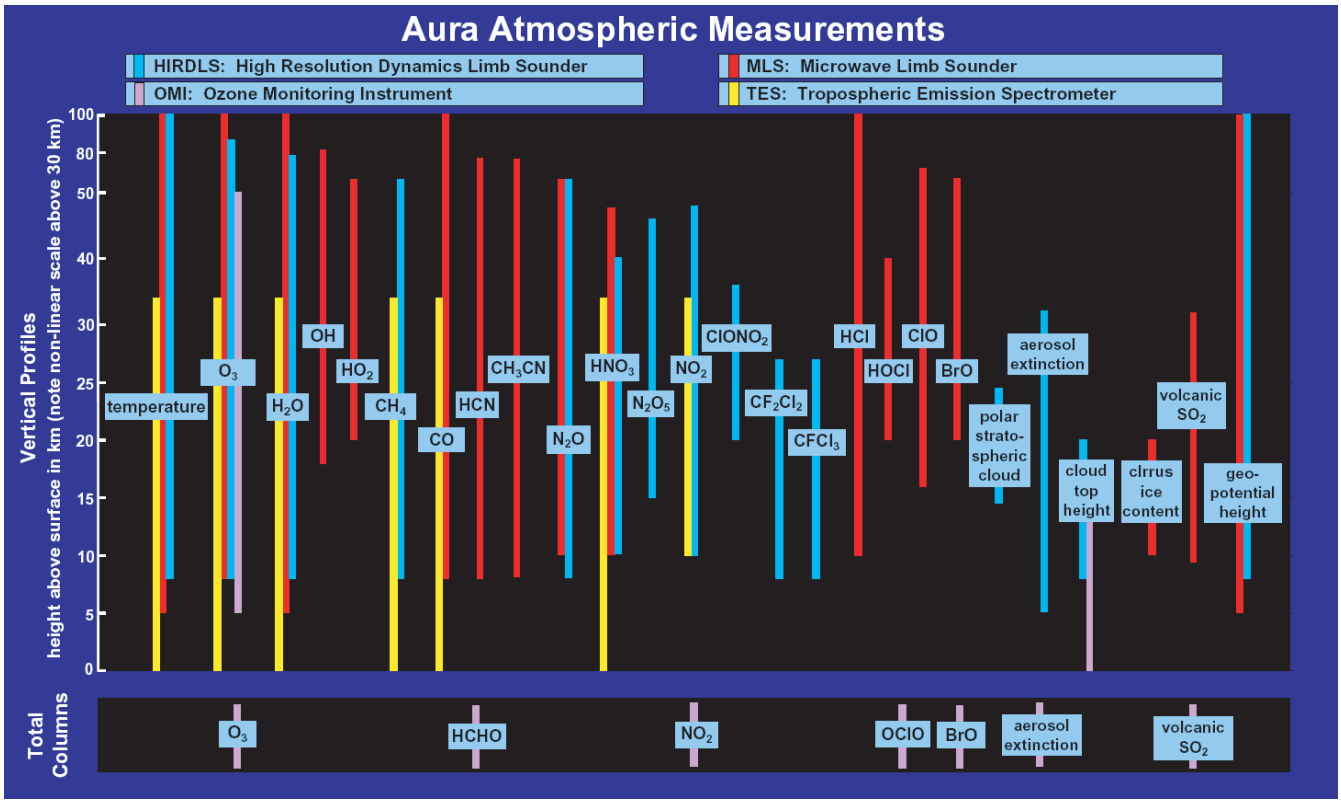

Figure 1-1. EOS Aura atmospheric measurements. Note that the vertical scale is non-linear above 25 km.

2. Heritage

EOS MLS has heritage from a number of aircraft and balloon experiments, and especially from the MLS experiment on the Upper Atmosphere Research Satellite (UARS).

Development of the MLS experiments began at the Jet Propulsion Laboratory in the mid-1970s and included instruments deployed on aircraft (e.g., Waters et al. [1979]) and balloon (e.g., Waters et al. [1981]) prior to application of the technique from space. The MLS instrument launched 12 September 1991 on UARS (e.g., Reber et al. [1993]) was the first application of the microwave limb sounding technique from space. The UARS MLS instrument is described by Barath et al. [1993] and uses ambient-temperature double-sideband heterodyne radiometers that operate near 63, 183 and 205 GHz. The primary data products for which UARS MLS was designed are stratospheric ClO, O_3, H_2O and atmospheric pressure at the tangent point of the observation path (to provide a vertical reference for the other measurements). Temperature was also obtained from the 63 GHz radiometer that provides the pressure measurement.

Validation of the UARS MLS primary data products, and their accuracies and precisions, are described in the *Journal of Geophysical Research* special issue (volume 101, number D6, 30 April 1996) on UARS data evaluation: temperature/pressure by Fishbein et al. [1996]; O_3 by Froidevaux et al. [1996], who also describe the retrieval algorithms that were used, Cunnold et al. [1996a,b], and Ricaud et al. [1996]; H_2O by Lahoz et al. [1996]; ClO by Waters et al. [1996]. Figure 2-1 shows the agreement obtained between MLS and some other well-calibrated measurements of the stratospheric O_3 profile. Additional data products obtained from UARS MLS, beyond those for which the instrument was primarily designed, include SO_2 injected into the stratosphere by volcanoes [Read et al. 1993], upper tropospheric H_2O [Read et al. 1995; 2001; 2004b,c), stratospheric HNO_3 (e.g., Santee et al. [1995, 2004]), temperature variances associated with atmospheric gravity waves in the stratosphere and mesosphere (e.g., Wu and Waters [1996]), stratospheric CH_3CN [Livesey et al. 2001, 2004a], and cloud ice near the tropopause [Wu et al., 2004]. Livesey et al. [2003] describe the latest version (V5) of the UARS MLS data products.

More than 200 refereed scientific publications using UARS MLS data have been published to date, and an updated publication list is kept on the MLS web site (http://mls.jpl.nasa.gov). Waters et al. [1999] give a summary of scientific results, and the following paragraphs discuss two examples.

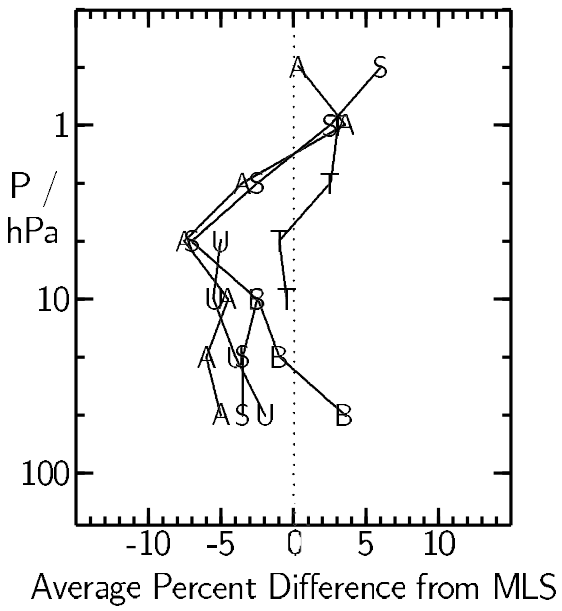

Figure 2-1. Results of comparing UARS MLS (Version 3) ozone with other well-calibrated near-coincident measurements (adapted from Froidevaux et al. [1996], and Cunnold et al. [1996a]). Points A are the average differences for SAGE II measurements, selected in low-aerosol situations, covering 25 N to 55 N latitudes, and made between September 1991 and December 1993. Points T are average differences for 295 Table Mountain (34 N), California, lidar profiles. Points B are average differences for 42 Boulder (40 N) ozonesondes. Points U are average differences for 8 balloon-borne ultraviolet photometer profiles, and Points S are average differences for 5 balloon-borne submillimeter limb sounder profiles.

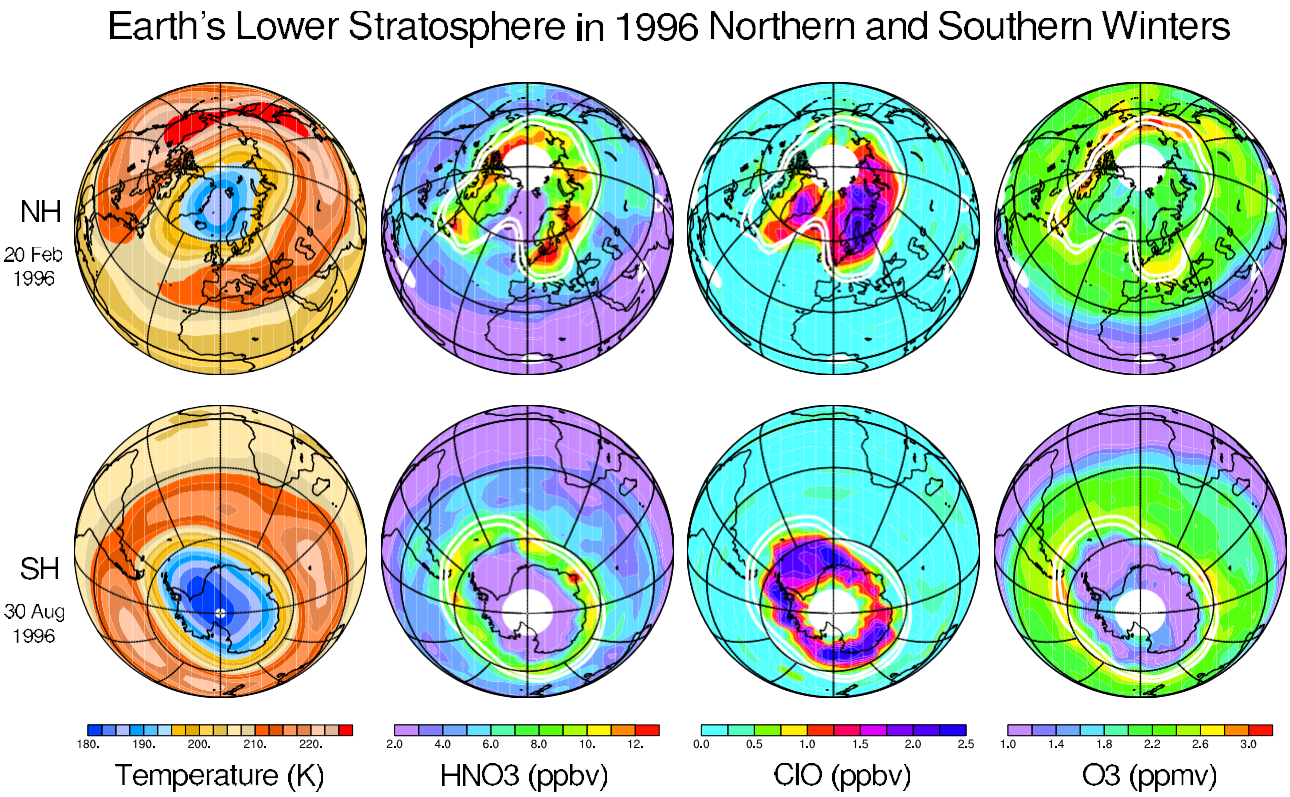

Figure 2-2. Earth's lower stratosphere in the Northern Hemisphere on 20 February 1996 (top) and in the Southern Hemisphere on 30 August 1996 (bottom). Measurements are interpolated to the 465 K potential temperature surface (~18 km), and white contours indicate potential vorticity values representative of the polar vortex edge. The HNO_3, ClO and O_3 data are from UARS MLS, and the temperature data are from operational analyses of the U.S. National Center for Environmental Prediction (NCEP). Temperatures in the blue and violet color ranges allow formation of polar stratospheric clouds from HNO_3 and H_2O; heterogeneous chemistry on these clouds leads to enhanced ClO that causes chemical depletion of O_3. HNO_3 also provides a source of NO_x, which quenches ClO and reduces the amount of ozone destruction. Both HNO_3 and O_3 increase in the lower stratospheric vortices during early winter due to downward transport of air rich in these species. The amount of ozone destruction each winter in the polar vortices depends on the duration of ClO enhancement, which is longer for the Antarctic than the Arctic. This difference is traceable to the Antarctic lower stratosphere being colder, and remaining cold for longer, than the Arctic.

Figure 2-2 illustrates some MLS results that have advanced our understanding of global-scale destruction of ozone by chlorine chemistry. The MLS maps for 20 February 1996, one of the coldest days in the Arctic in recent years, show many similarities to the Antarctic in regards to processes leading to substantial ozone depletion. MLS measurements have shown that enhancement of ozone-destroying ClO throughout the Arctic winter vortex, similar to that in the Antarctic, is a recurrent feature. Only occasionally, however, have reductions in Arctic HNO_3 of the amount shown in the top row of Figure 2-2 been observed by MLS. The abundances of HNO_3 and ClO are very sensitive to temperature (for the range of temperatures experienced in the Arctic winter lower stratosphere), and a small amount of Arctic cooling could cause much greater removal of Arctic HNO_3, longer duration of enhanced ClO and O_3 destruction, and greater similarity to current Antarctic conditions.

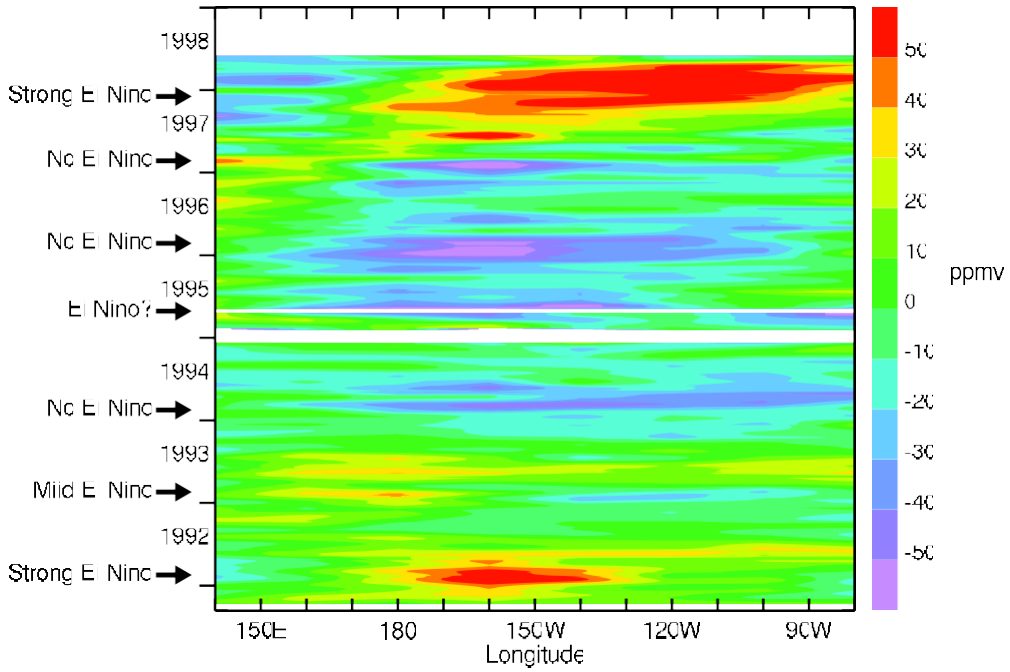

Figure 2-3. Correlation between variations in tropical Pacific upper tropospheric water vapor and El Niño sea surface temperature events. Data shown here are deviations from the mean in upper tropospheric water vapor at 215 hPa pressure (~11 km height) within 5 degrees of the equator as measured by UARS MLS. The vertical axis is time, covering late September 1991 through early June 1998. The horizontal axis is longitude in the tropical Pacific region. Labels along the left axis indicate whether or not an El Niño event in sea surface temperature occurred each year. Note the large increases in upper tropospheric water vapor during the 1991-92 and, especially, the 1997-98 El Niño events.

Figure 2-3 shows some UARS MLS results for upper tropospheric water vapor. Upper tropospheric water vapor, especially in the tropics, is thought to play a major role in feedback mechanisms affecting global warming. As is clear from this figure, there is strong correlation between El Niño sea surface temperature anomalies and upper tropospheric water vapor anomalies as observed by MLS. Improved understanding of these couplings, to which the MLS data are contributing, may help improve the ability to predict climate variations on seasonal-to-interannual time scales.

EOS MLS is improved over UARS MLS in having:

(1) additional stratospheric measurements for chemical composition and dynamical tracers,
(2) more and better upper tropospheric measurements,
(3) better global and temporal coverage, and better spatial resolution, and
(4) better precision for measurements of temperature, O_3, ClO, upper tropospheric H_2O, and perhaps others.

These improvements are possible because of:

(1) advances in microwave technology since development of the UARS instrument,
(2) better understanding of the technique's capabilities as a result of UARS experience,
(3) design of EOS MLS for upper tropospheric and lower stratospheric measurements,
(4) the EOS near-polar orbit, which allows nearly pole-to-pole coverage on each orbit, and
(5) measurements being made in the orbit plane, allowing more accurate handling of gradients in the direction along the measurement track.

Measurements in the 640 GHz band used in EOS MLS have been made from balloon by Stachnik et al. [1992], and in the 2.5 THz OH band by Pickett [1999].

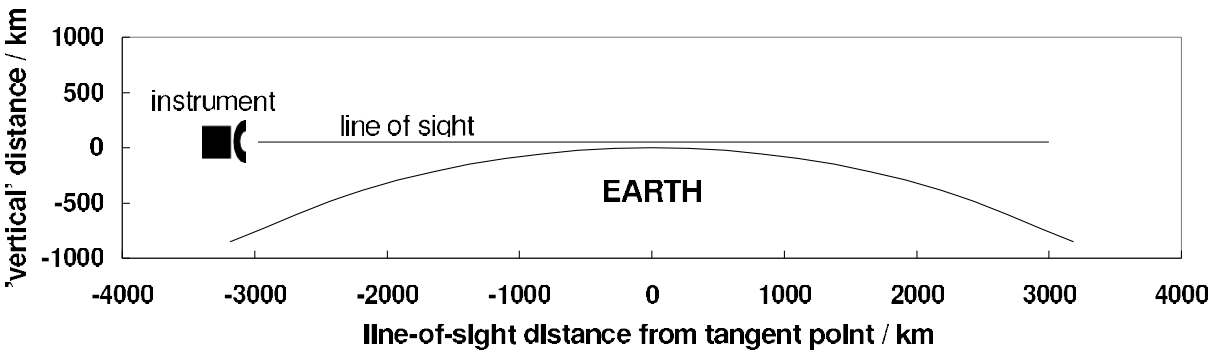

Figure 3-1. MLS measurement geometry. The geometry is drawn to scale with an instrument in 705 km altitude orbit (that of the Aura satellite) and the line of sight having 50 km tangent height. The size of the instrument is grossly exaggerated, of course. The orbit plane for EOS MLS is the plane of the paper, whereas for UARS MLS the orbit plane is perpendicular to the plane of the paper.

3. Measurement Technique

Microwave limb sounding obtains remote measurements of atmospheric parameters by observing millimeter- and submillimeter-wavelength thermal emission (radiances) as the instrument field-of-view (FOV) is scanned through the atmospheric limb from above. Figure 3-1 shows the geometry.

Features of the technique, described further by Waters (1993), include:

1. the ability to measure many atmospheric gases, with emission from molecular oxygen (and other molecules) providing temperature and pressure;
2. reliable measurements, even in the presence of heavy aerosol, cirrus or polar stratospheric clouds that degrade shorter-wavelength ultraviolet, visible and infrared techniques;
3. the ability to make measurements at all times of day and night, and to provide global coverage on a daily basis;
4. the ability to spectrally resolve emission lines at all altitudes, which allows measurements of very weak lines in the presence of nearby strong ones and thus measurements of chemical species with very low atmospheric abundances;
5. composition measurements that are relatively insensitive to uncertainties in atmospheric temperature;
6. a very accurate spectral line data base (e.g., Pickett et al. [1992], Oh and Cohen [1994], Drouin [2004]; Drouin et al. [2004]). (The spectroscopic data base for tropospheric 'continuum' measurements at MLS wavelengths is being established [DeLucia, et al. 2004]);
7. instrumentation that has very accurate and stable calibration (For example, analyses of UARS MLS measured 'space radiances', as discussed later in this section, indicate less than 0.02% change in antenna mirror reflectivity over a 5-year period in orbit. This, in turn, implies an upper limit of 0.02% change in calibration due to mirror degradation, which is thought to be the largest contributor to calibration changes); and
8. instrumentation that has adequate sensitivity, without necessarily requiring cooling, and good vertical resolution set by size of the antenna.

The widths of spectral lines in the millimeter and submillimeter-wavelength spectral regions used by MLS are dominated by pressure (collisional) broadening throughout the troposphere and stratosphere, resulting in the linewidth being a nearly exponentially decreasing function of height up to ~50-70 km. Doppler broadening dominates the linewidth at higher altitudes. Figure 3-2 on the next page shows linewidth variation with height for some representative spectral lines measured by EOS MLS.

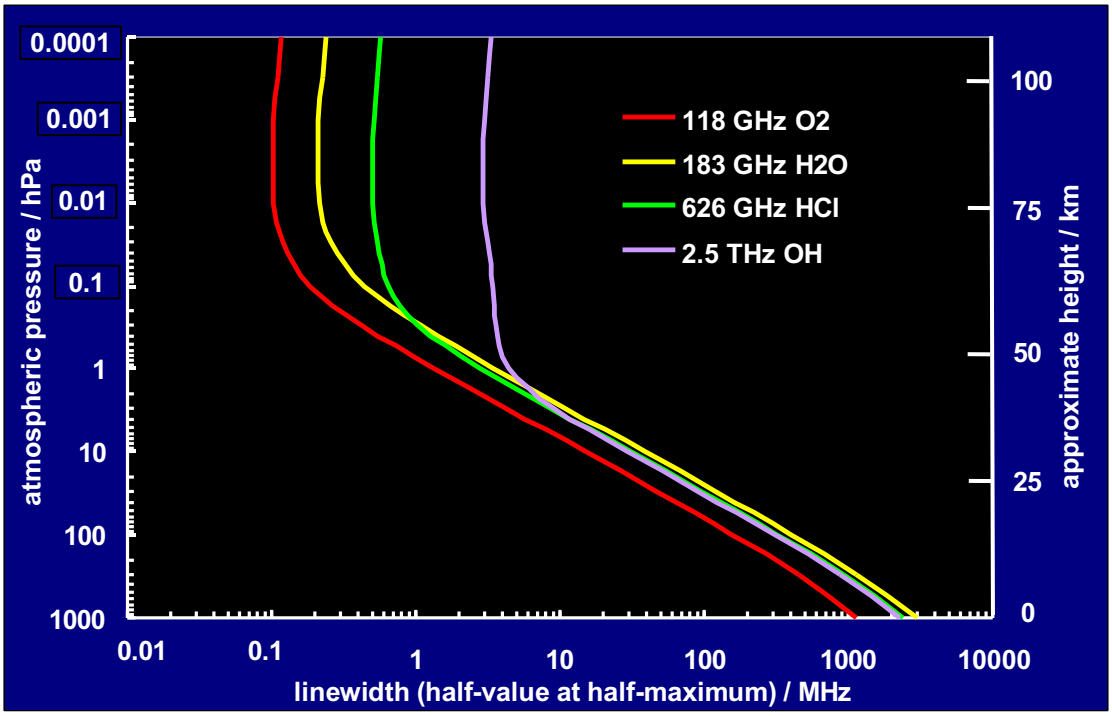

Figure 3-2. Linewidth versus height for some spectral lines measured by EOS MLS.

Figure 3-3 below shows an example of spectra measured by UARS MLS, and illustrates the ability of the technique to spectrally resolve individual emission lines. Having several spectral channels covering a single emission line (and resolving this line at all altitudes of interest) provides robust measurements, since geophysical quantities can be obtained from the channel-to-channel spectrally-varying component of the measured thermal emission. Extraneous effects, such as stray radiation, generally have spectrally-flat emission over the spectral range used for measurements, and their uncertainties do not usually have first-order effects on the retrievals of geophysical parameters.

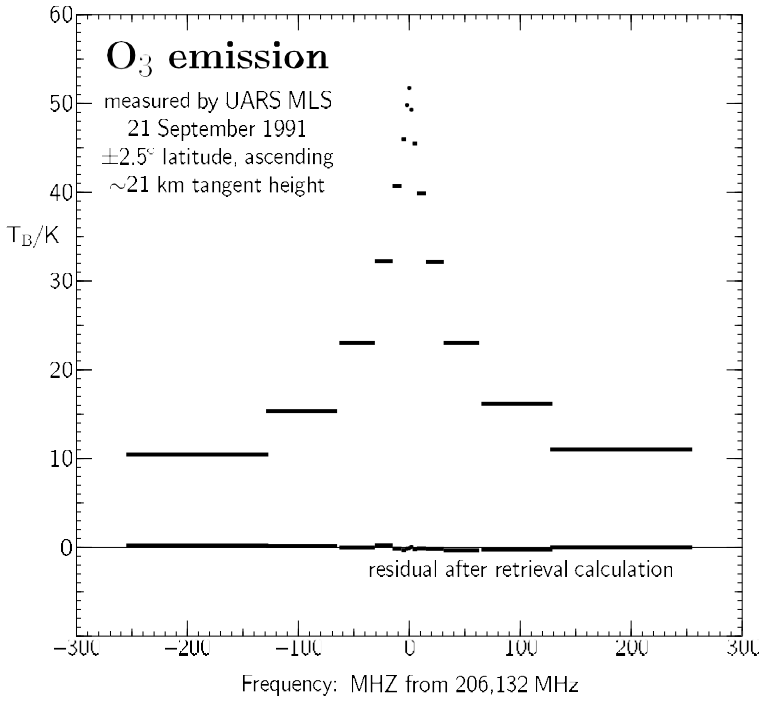

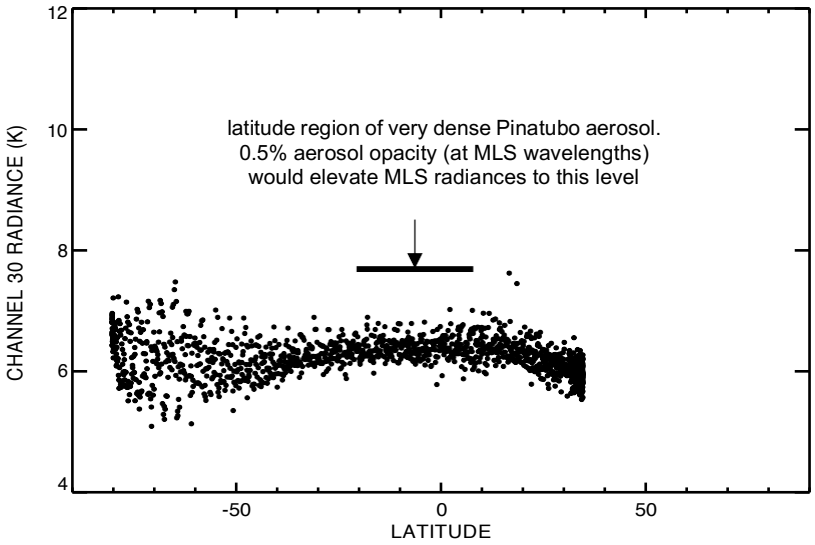

Figure 3-4. MLS 205 GHz radiances (wing channel of ClO band) from the lower stratosphere (50 hPa tangent pressure) versus latitude for all measurements from all orbits on 21 September 1991. The tropical lower stratosphere had very heavy loading of aerosol from the Pinatubo volcano at this time. As anticipated on theoretical grounds, the MLS radiances are not noticeably affected by this aerosol layer, with an observational upper limit of ~0.1% opacity through the limb path.

Figure 3-4 illustrates the insensitivity of measurements to volcanic aerosol by showing 205 GHz radiances from the lower stratosphere measured by UARS MLS when the tropics contained very heavy loading of aerosol from the Mt. Pinatubo volcano. No effect of the aerosol on the MLS radiances is seen, as expected from theoretical considerations, with an upper limit of ~0.1%. The ozone spectral line shown in Figure 3-3 was measured in the presence of this aerosol.

Figure 3-5 below shows data illustrating the excellent long-term stability of the UARS MLS antenna system reflectivity. 'Space radiances,' the radiances measured through the antenna system when it is pointed well above the atmosphere, are plotted. The typical in-orbit temperature of the antenna is ~250 K, and the slope of the best fit line, including its uncertainty, shown in Figure 3-5 thus corresponds to an upper limit of $\sim 3\times10^{-5}$ (= 0.007 K / 250 K) change per year in the overall antenna system reflectivity, or an upper limit of $\sim 2\times10^{-4}$ change over the ~5-year period analyzed. Scatter in the points is due to limitations of the simple model used to remove cyclical, mainly 'UARS-monthly', temperature-dependent effects. Degradation in reflectivity of the antenna reflector surfaces is thought to dominate any degradation in instrument radiometric calibration because these are the only surfaces in the signal path that are exposed to solar ultraviolet radiation and atomic oxygen. Changes in antenna reflectivity affect overall radiometric calibration proportionally, and these data therefore imply an upper limit of $\sim 3\times10^{-5}$ per year (0.003% per year) degradation in UARS MLS radiometric calibration due to this effect. Similar performance is expected from EOS MLS.

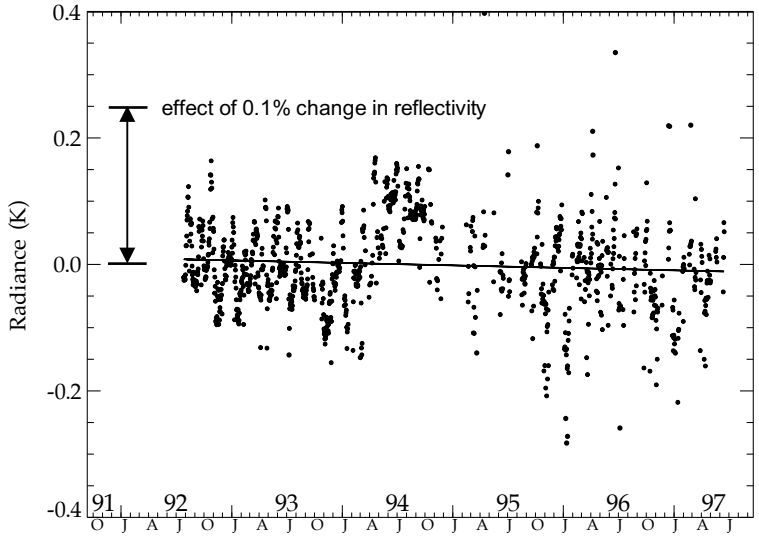

Figure 3-5. Time-series of UARS MLS space radiances after applying a simple model to account for variation in temperature of the antenna. The marker on the left shows the effect that 0.1% change in reflectivity, with concomitant emissivity change, would have had. The nearly horizontal line is a best fit to the radiance trend over the ~5 year period analyzed; and has slope of -0.004 K/year with ±0.003 K/year 2σ uncertainty The data shown here are spectral averages for UARS MLS band 4 (206 GHz ozone spectral line).

4. EOS MLS Scientific Objectives

As stated earlier, the overall scientific objectives of EOS MLS can be grouped into the following categories:

(1) stratospheric ozone,

(2) tropospheric ozone and pollution,

(3) climate variability.

Following subsections summarize objectives in each of these categories. Key questions, as identified by NASA Earth Science Enterprise [2000], provide an overall focus for the objectives and are given (in italic font) at the beginning of the subsection for each of these categories.

4.1. Stratospheric Ozone

How is stratospheric ozone changing, as the abundance of ozone-destroying chemicals decreases and new substitutes increase?

How do stratospheric trace constituents respond to changes in climate and atmospheric composition?

How well can future atmospheric chemical impacts on ozone and climate be predicted?

4.1.1. Global Stratospheric Ozone and Chemistry

An overarching question is whether global stratospheric ozone will recover as expected in the next few decades, following the international regulations on ozone depleting substances. Stratospheric total chlorine will be near its peak during the Aura mission, and stratospheric total bromine is expected to still be increasing, although more slowly than previously [WMO, 2002]. We thus expect some abatement of ozone depletion during Aura's lifetime and an eventual global recovery, which may not be definitively detectable until later [Reinsel et al., 2002; WMO, 2002]. Climate change could possibly delay ozone recovery – both through stratospheric cooling that can exacerbate some ozone destruction processes, and possibly through changes in transport across the tropical tropopause that could affect the amount of H_2O (and perhaps other substances) in the stratosphere. Projected increases in stratospheric H_2O may delay ozone recovery by 10-30 years [Dvortsov and Solomon, 2001; Shindell, 2001].

- **What are the global ozone changes during the Aura mission?** The MLS ozone data will be combined with data from other Aura instruments (and other sources) to collectively produce an accurate record of global ozone changes as part of the longer-term ozone trends record. With significant improvements in precision over UARS, Aura measurements are expected to be especially valuable for quantifying changes in the lower stratosphere.
- **Do we understand global changes in lower stratospheric ozone?** MLS data on N_2O, H_2O, HO_x, BrO, ClO, HCl, HOCl, and temperature (with other Aura measurements of NO_x) will be used to further constrain and test models of ozone change in this region.
- **Do we understand global changes in upper stratospheric ozone?** Stratospheric ozone declines may reverse first in the upper stratosphere, partly because of the smaller relative effects of dynamics there; climate change also may hasten recovery in this region. MLS profiles of O_3 and ClO will be used as part of the critical data to evaluate this issue.
- **Do we understand variations in source gases that can affect stratospheric ozone?** Large and unexpected changes in stratospheric H_2O and CH_4 occurred in the 1990s [WMO, 1999]. MLS (and other Aura) measurements of H_2O, MLS and HIRDLS measurements of N_2O, and HIRDLS and TES profiles of CH_4, will be used to compare to model expectations and for constraining model predictions of stratospheric ozone change.

4.1.2. Chlorine chemistry

- **Do we understand total stratospheric chlorine variations and trends?** A thorough understanding of changes in the stratospheric chlorine burden is fundamental to determining if ozone is recovering 'as expected'. It is possible that our understanding of stratospheric chlorine loading is incomplete: Waugh et al. [2001] found an inconsistency in the timing and magnitude of the peak in total chlorine abundance at 55 km deduced from UARS HALOE HCl observations and the amount inferred from surface observations. Upper stratospheric HCl from MLS will be compared to other HCl measurements made during the Aura mission, and to ground-based data for total chlorine.
- **Do we understand stratospheric reactive chlorine variations and trends?** ClO from MLS provides a measure of the rate at which chlorine destroys ozone. As a major improvement over UARS MLS, EOS MLS will measure both ClO and HCl. Changes in the ClO/HCl ratio, measured very accurately by MLS, provide a stringent test of our understanding of stratospheric chlorine chemistry. Variations in total global reactive chlorine can be dominated by factors other than total chlorine (e.g., by unusual changes in CH_4 [Siskind et al., 1998; Froidevaux et al., 2000]). HIRDLS CH_4 data will be essential for understanding observed variations in upper stratospheric ClO.
- **Do we understand middle and upper stratospheric chlorine partitioning?** Aura will provide a suite of global measurements that will be used for a more stringent/extensive test of upper stratospheric chlorine partitioning than previously possible. Relevant measurements include MLS profiles of ClO, HCl, OH and HO_2; HIRDLS profiles of $ClONO_2$ and CH_4; and HIRDLS and MLS profiles of temperature, O_3, N_2O, and H_2O.
- **Do we understand lower stratospheric chlorine partitioning?** Continued global testing of lower stratospheric chlorine partitioning will be performed using MLS measurements of ClO and HCl (and first global measurements of HOCl), along with $ClONO_2$ from HIRDLS, and NO_x from HIRDLS and TES; such testing will be enhanced by observed tracer (N_2O, CH_4) distributions and model comparisons.

4.1.3. Hydrogen chemistry

MLS will provide the first global measurements of OH and HO_2, the key radicals in hydrogen chemistry. This chemistry dominates ozone destruction at ~20-25 km, and above ~45 km, and its understanding is essential for assessing how stratospheric ozone might change in response to climate and composition changes. Our current understanding of hydrogen chemistry in the upper stratosphere is in question due to MAHRSI OH observations that do not appear to be consistent with current theory [Conway et al., 2000].

- **Can we understand upper stratospheric and mesospheric hydrogen chemistry?** Simultaneous MLS observations of OH and HO_2 in the upper stratosphere and mesosphere, along with H_2O and O_3, will provide much stronger tests than previously possible of HO_x chemistry and ozone destruction in these regions. This should resolve (or, at least, substantially help resolve) the HO_x dilemma detected in MAHRSI data which show less OH above 50 km than predicted, and more OH below 50 km than predicted.
- **Do we understand hydrogen chemistry couplings in the lower stratosphere?** OH and HO_2 abundances affect the lower stratospheric partitioning among species in the nitrogen, chlorine, and bromine families. The simultaneous MLS observations of OH and HNO_3 and HIRDLS observations of NO_2 (and HNO_3), for example, will allow tests of the expected relationship between these species globally over a wide height range. HO_x also affects reactive chlorine

partitioning as well as the partitioning between active bromine and HBr, and thus provides further constraints on photochemical models of the lower stratosphere.

4.1.4. Bromine chemistry

It is estimated that stratospheric bromine contributes significantly (roughly 30-50%) to the current ozone depletion rate [WMO, 1999]. Bromine abundances in the stratosphere are still increasing, but more slowly than a few years ago [WMO, 2002]. Bromine abundances in the troposphere have most likely reached a peak [Montzka, et al., 2003] which should be reflected in the stratosphere.

- **Can we understand the global and seasonal variations of stratospheric BrO?** MLS monthly zonal means for BrO will be used to produce a global climatology of stratospheric BrO profiles and their variations on seasonal and annual time scales. More localized studies will include polar winter phenomena, comparing the Arctic and Antarctic winter vortices. These observations will be compared and contrasted to similar phenomena observed in ClO. The observed BrO global distribution, seasonal variations - and diurnal variations near the orbit extremes - will be compared with predictions from photochemical models.
- **Can we determine and understand total bromine in the upper atmosphere?** The MLS BrO observations can be used in conjunction with models to constrain the budgets of atmospheric bromine. Including the MLS simultaneous observations of HO_2, currently thought to be the major loss mechanism of BrO in the upper statosphere and lower mesosphere through the reaction $BrO + HO_2 \rightarrow HOBr + O_2$, will allow estimates to be made of the total abundance of inorganic bromine. This will increase our understanding of the global budget of atmospheric bromine, and perhaps its trends, which is an issue of significant current interest.

4.1.5. Polar Winter Processes

Ozone recovery may be delayed with a colder more humid stratosphere possibly arising from climate change. The Arctic, in particular, may be at a threshold for more severe O_3 loss in the future. MLS measurements of many species involved in polar processes, as well as O_3 and temperature, will improve understanding of how climate change may affect polar ozone recovery.

4.1.5.1. Polar winter vortex development and evolution

Development of the vortex in fall and early winter strongly affects conditions later when polar processing occurs. Transport in/through the upper stratosphere is particularly important since air in this region descends to the lower stratosphere in spring [e.g., Plumb et al., 2002].

- **What are the effects of fall vortex development on processing later in winter?** MLS and HIRDLS will provide data on temperature evolution and uncertainties. Global daily fields and tracer correlations from MLS/HIRDLS will be used to study the evolution and origins of air in the polar vortex, and interannual variability in descent and mixing.
- **Where does air in the lower stratospheric vortex originate?** MLS/HIRDLS geopotential height and temperature will be used to calculate winds and descent at higher altitudes than has previously been possible to do routinely with confidence, and H_2O, CH_4, and CO will provide more direct information on descent into the stratospheric vortex, helping to determine origins of air involved in polar processing.

4.1.5.2. Polar stratospheric clouds

PSCs are known to play pivotal roles in controlling the amount of polar ozone loss, but key aspects of their formation, composition, and sensitivity to climate change are still uncertain.

- **What are the phase and composition of PSC particles, and what are the dominant mechanisms governing their formation?** Many deficiencies in previous studies using satellite data will be ameliorated with simultaneous, colocated HNO_3, H_2O and temperature from MLS/HIRDLS and aerosol from HIRDLS/OMI. Better precision and resolution will reduce ambiguity in data/model comparisons, and better coverage will allow complete PSC lifecycles and intraseasonal cloud changes to be tracked. Correlating PSC detections based on MLS HNO_3 and HIRDLS aerosol extinction with temperature, tropopause pressure, and column ozone will improve our knowledge of the relative importance of synoptic-scale uplift versus mesoscale temperature fluctuations in promoting PSC formation.
- **Will the spatial extent, duration, or frequency of PSCs increase in the future?** Aura data will help determine whether changes/trends in lower stratospheric temperature and/or H_2O induce significant changes in the prevalence or character of PSCs, especially in the Arctic, where the lower stratosphere now is often only marginally cold enough for PSCs.

4.1.5.3. Denitrification and dehydration

Ozone loss is influenced by denitrification and dehydration in the polar winter, but these processes and their sensitivity to climate change are still inadequately understood.

- **What are the mechanisms for denitrification, what is its relationship to dehydration, and how sensitive are these processes to changes in temperature or H_2O?** UARS data indicate that denitrification precedes dehydration in the Antarctic [Tabazadeh et al., 2000]. Observation of large HNO_3-containing particles during an unusually cold Arctic winter [Fahey et al., 2001] appears to confirm that these processes are independent, but it remains uncertain whether such large particles form during typical Arctic winters or in the Antarctic. The coverage/quality of temperature, HNO_3, H_2O, and aerosol extinction from MLS and HIRDLS will improve understanding of these processes and their sensitivities.
- **Is widespread severe denitrification necessary for massive ozone loss?** Ongoing processing on sulfate aerosol may be more important than denitrification in maintaining enhanced ClO in spring [e.g., Portmann et al., 1996]. MLS/HIRDLS temperature, aerosol, HNO_3, ClO, HCl, $ClONO_2$, and O_3 data will allow us to clarify the relative importance of denitrification versus chlorine activation on PSCs/sulfate aerosol in facilitating ozone loss.

4.1.5.4. Chlorine activation, deactivation and the chlorine budget

Understanding chlorine activation, deactivation, and the chlorine budget with its seasonal evolution is crucial for understanding polar ozone loss.

- **Is our understanding of chlorine activation, the relative abundances of the main reservoir species, and deactivation in the winter polar lower stratosphere quantitatively correct?** Simultaneous ClO, HCl, and $ClONO_2$ measurements from MLS and HIRDLS will allow chlorine partitioning to be studied in detail. High priority will be given to understanding any discrepancies between the largest values of observed and modeled ClO.
- **Does the chlorine budget balance?** Observations from the 1999/2000 Arctic winter initially indicated a discrepancy in the chlorine budget [WMO, 2002]; reanalysis of the data reduced the discrepancy but did not eliminate the possibility of 'missing' chlorine species. MLS/HIRDLS ClO, HCl, $ClONO_2$, and CFC11 and CFC12 will help resolve this issue.

- **Are there unknown photolytic processes that enhance chlorine destruction of O_3?** Models substantially underestimate O_3 loss during cold Arctic winters, and recent analyses [Rex et al., 2003] implicate an unknown process involving photolysis at high solar zenith angles. Comparing MLS ClO and O_3 with model results will help identify the mechanism.

4.1.5.5. Chemical ozone loss in polar winter

Different methods and datasets give qualitatively similar results in current Arctic ozone loss studies, but detailed quantitative agreement is lacking and hampered by limited data and large uncertainties in loss estimates. Outstanding issues in the Antarctic include predicting the onset of ozone loss, quantifying midwinter loss, and understanding loss in the subvortex.

- **How well can we quantify ozone loss throughout the winter, in both the Arctic and Antarctic?** Four general methods [e.g., Harris et al., 2002] have been used to estimate ozone loss from direct observations of ozone: 'match' techniques, calculations of vortex-average descent and O_3 changes, comparisons of observed O_3 with passive O_3 in transport models, and evolution of O_3/tracer correlations. Using these methods with MLS data should greatly improve estimates of O_3 loss and quantification of their uncertainties. Aura tracer data will be used to assess applicability and limitations of the tracer correlation method applied to satellite measurements. The MLS ClO, and related, data will also allow direct calculation of the amount of ozone loss expected from chlorine chemistry [e.g., Mackenzie et al., 1996].
- **What are the relative contributions of polar dynamical and chemical processes to long-term ozone changes?** Improved column ozone loss estimates from Aura data will be used with dynamical models to improve our understanding of the relative importance of dynamical and chemical processes in Arctic ozone variability.

4.1.6. Dynamics and Transport

Understanding stratospheric dynamics and transport is essential for understanding stratospheric O_3 and its variations. Unique MLS contributions in this area include routine measurements every 1.5° along the orbit track, and measurements in the presence of ice clouds and aerosol that can degrade infrared, visible and ultraviolet measurements.

4.1.6.1. Dynamical effects on ozone trends [4]

Downward trends in midlatitude ozone [e.g., Staehelin et al., 2002] arise from a combination of chemical and dynamical processes. Both day-to-day [e.g., Hood et al., 2001] and interannual [e.g., Appenzeller et al., 2000] O_3 variability are strongly related to dynamical processes. Variability and trends in wave propagation, wave-breaking, and tropopause characteristics have direct effects on column ozone. Summertime ozone variability has been related to Rossby-wave propagation and to the dynamics of the vortex breakup. Dynamical and transport processes are intimately involved in extra-tropical stratosphere-troposphere exchange.

What are the roles of dynamical and transport processes in day-to-day, seasonal and interannual ozone variability? Daily 3D O_3 fields from MLS/HIRDLS will be used to quantify the roles of dynamical processes in O_3 variability. Relationships between lower stratospheric temperatures, tropopause heights, column O_3, 3D O_3 structure and wave fluxes (all of which can be derived from MLS and/or HIRDLS data) will be studied. MLS/HIRDLS O_3 and H_2O in the upper troposphere and lower stratosphere (UT/LS) will be used to relate trends/variability in extratropical stratosphere-troposphere exchange to dynamical processes.

What are the processes governing relationships between changes in stratospheric ozone, tropopause height, and UT/LS dynamical variations? Tropopause height, temperature and other dynamical properties derived from MLS and HIRDLS temperature and geopotential height will be correlated with observed column O_3 to elucidate relationships between changes in the two, and analyzed with ozone profiles to understand the mechanisms behind these relationships.

4.1.6.2. Effects of polar processes on midlatitude ozone

Polar vortex processes can affect midlatitude ozone through export of PSC-activated air with subsequent in-situ midlatitude ozone loss and through export of ozone-depleted air. However, observations to date have been inadequate for quantifying these two effects. Aura data will allow a more detailed quantitative study of them.

- **How well can we quantify the export of vortex-processed air to midlatitudes?** The evolution of 3D trace gas fields will be examined to identify and quantify export of vortex-processed air. Vortex and extravortex tracer correlations differ strongly in late winter and spring, due to effects of descent/mixing and chemical/microphysical processes; such correlations will be used to identify and study air transported out of the vortex. Air parcel history calculations will identify the origins of air escaping from the vortex. The 1.5° along-track spacing of MLS measurements is particularly useful for identifying vortex filaments, and the 1 km vertical resolution of HIRDLS is particularly suited to detecting laminae that arise from such filaments.
- **How well can we model the effects of vortex-exported air on midlatitude ozone?** 3D trace gas fields from Aura will be used to initialize chemical transport models (CTMs) for detailed modeling studies of transport of air from the polar vortex and for comparison with model results. MLS and HIRDLS observations will be used to identify the composition of air exported from the vortex for modeling in situ loss in midlatitudes.

4.1.6.3. Tropical transport and its effect on stratospheric ozone [1]

Understanding the tropical tropopause region is crucial to predicting trends in stratospheric H_2O and hence the recovery of ozone, yet our current understanding is so poor that we cannot even explain the sign of the observed H_2O trend. Seasonality and interannual variability in the tropical tropopause temperature is consistent with control by the stratospheric residual circulation, which is driven by extratropical wave activity. The relative roles of stratospheric residual circulation and convectively-driven disturbances are now a topic of scientific debate. Model results [Potter and Holton, 1995] have also suggested that convectively generated buoyancy waves may play an important role in dehydrating the tropical lower stratosphere.

- **Can we obtain better estimates of vertical velocity and related parameters, and thus a better understanding of the stratospheric "tape recorder"?** Rising tropical air remains remarkably little changed by other stratospheric air or by vertical mixing – the seasonal cycle of stratospheric H_2O is preserved for ~1.5 years as the air rises. Several attempts have been made to quantify horizontal dilution and vertical diffusion rates. The multi-year datasets of H_2O and CH_4 from Aura will permit us to better address this issue, and look for interdecadal variability resulting from anthropogenic changes in atmospheric composition.
- **What are the effects of the seasonal cycle and quasi-biennial oscillation (QBO) on stratospheric ozone?** The QBO influences the distribution of stratospheric ozone in several ways. The secondary residual circulation induced by it results in temperature fluctuations, which affect temperature-dependent photochemistry of O_3 and the entry value of H_2O that can

[1] Material in this section was contributed by Dr. Philip Mote.

affect O_3 chemistry. The QBO influences wave propagation into the tropics that shapes the distribution of trace constituents. Analyses of Aura O_3 and H_2O measurements over several annual and QBO cycles will extend our understanding of how the QBO and annual cycle interact to influence stratospheric ozone and tracer distributions.

4.1.6.4. Gravity waves and effect on stratospheric circulation and ozone

Gravity waves (GWs) play important roles in determining atmospheric circulation and thermal structure. Comprehensive atmospheric models used in ozone loss studies rely on GW parameterizations to produce realistic stratospheric polar vortex and temperature distributions, but current parameterizations are crude and quite arbitrary with many *ad hoc* settings.

- **What is the global distribution of gravity waves, and their propagation and source properties?** GWs are generated from flow over mountains, deep convection, etc., but their sources and distributions are highly uncertain. MLS will measure GWs with >~5 km vertical and > ~100 km horizontal wavelengths, and HIRDLS with >~1 km vertical and >~300 km horizontal wavelengths; these will provide important constraints to GW theories and model parameters. Comparative studies of observations (Aura, GPS, ground-based) and mechanistic model simulations should offer unprecedented insight into GW processes.
- **To what extent do gravity waves contribute to PSC formation?** The uncertainty of GWs' role in PSC formation hinders the reliable prediction of future ozone loss in the polar region. GW-related PSC formation will be investigated in conjunction with HIRDLS, TES and OMI PSC measurements, as MLS GW observations can be made simultaneously at these PSC locations but are not contaminated by the clouds.

4.1.7. Dehydration of the Stratosphere [2]

How and why stratospheric humidity has been increasing for the last few decades [e.g., Rosenlof et al., 2001] has important implications for stratospheric O_3 [e.g., Dvortsov and Solomon, 2001] and radiative forcing of climate [e.g., Smith et al., 2001]. Knowledge of the mechanisms regulating stratospheric humidity is required to adequately understand processes, including potentially important feedbacks, affecting both O_3 and climate. Dehydration mechanisms in the Tropical Tropopause Layer (TTL) clearly remove most of the tropospheric H_2O, and two theories for this mechanism have emerged. "Convective dehydration" [e.g., Sherwood and Dessler, 2001] posits that air emerges from convection fully dehydrated (on average) to stratospheric values. "Gradual dehydration" [e.g., Holton and Gettelman, 2001] posits that air is dehydrated after detrainment from convection by repeated exposures to episodic cold events as it slowly ascends into the stratosphere.

- **Does convection hydrate or dehydrate the TTL?** MLS measurements of the 3D structures of H_2O and other trace gases around the tropical tropopause will help determine the extent to which convection hydrates or dehydrates the TTL. Because low O_3 (high CO) indicates air that has been recently transported from the planetary boundary layer, coincidence between regions of low H_2O and low O_3 (high CO) indicates convective dehydration. Lack of such a coincidence indicates gradual dehydration.
- **What role does the Asian monsoon play in regulating stratospheric humidity?** The Asian monsoon has come under increasing scrutiny as a major player in the water budget near the tropopause. Moistening of the TTL and midlatitude lowermost stratosphere appears clearly in observations [e.g., Randel et al., 2000], but it is unclear how the monsoon affects air entering the

[2] Drs. Andrew Dessler and Rong Fu contributed material in this section.

stratosphere at potential temperatures above 380 K. MLS (and HIRDLS) fields of H_2O, O_3, and other tracers, in combination with transport model studies, will be used to trace the motion of H_2O for determining the Asian monsoon's role.

- **What is the role of thin cirrus in the TTL?** The role of thin cirrus in the H_2O budget of the TTL is uncertain. The combination of MLS (and HIRDLS) H_2O and temperature measurements and HIRDLS and Aqua MODIS measurements of thin cirrus, will provide insight into the role of these clouds. We will examine from a broad viewpoint whether thin cirrus formation is slaved to local temperature or if other factors (e.g., air mass history) are important. The humidity field evolution will be correlated with cirrus occurrence and environmental conditions to yield critical constraints on the dehydration role of cirrus.
- **What is the role of diabatic cross-tropopause transport over the extra tropics?** As summarized by Holton et al. [1995], the role of diabatic cross-tropopause H_2O transport in the extratropics is perhaps the least understood component in of the H_2O budget in the extratropical lower stratosphere. Preliminary analyses of UARS MLS data for the North Atlantic region also suggest that the diabatic cross-tropopause transport frequently transports equal or even greater amounts of water vapor per event than the isentropic cross-tropopause transport during summer in the extratropics [Fu et al., manuscript in preparation]. Data from Aura MLS, along that from HIRDLS and operational meterological analyses will enable us to more accurately examine this issue, and hence more clearly determine the role of extratropical diabatic cross-tropopause H_2O transport.

4.1.8. Volcanic Effects on Stratospheric Ozone

Stratospheric aerosol variability over the past 25 years has been dominated by the effects of episodic volcanic eruptions [WMO, 2002], and 30% of the last 150 years have been characterized by volcanic clouds as optically thick as Arctic PSCs [Tabazadeh et al., 2002]. An explosive, sulfur-rich volcanic eruption within the next few decades – when stratospheric chlorine loading is still high – could have profound consequences. If a major volcano erupts during the Aura mission, MLS objectives will include addressing the following key questions.

- **How does volcanically-enhanced sulfate aerosol perturb stratospheric nitrogen and chlorine concentrations?** Following volcanic eruptions, the SO_2 injected into the stratosphere is rapidly converted into sulfate aerosol, greatly extending the latitudinal, altitudinal, and temporal ranges over which heterogeneous processes alter nitrogen and chlorine partitioning [e.g., Solomon, 1999]. These perturbations will be investigated with Aura measurements of HNO_3, N_2O_5, NO_2, ClO, HCl, $ClONO_2$, and column OClO.
- **How does volcanically-enhanced sulfate aerosol affect PSC formation/denitrification?** Models indicate that under volcanic conditions the sulfate-rich composition of ternary solutions hampers formation of solid PSCs [Tabazadeh et al., 2002], limiting the effectiveness of PSC particles in causing denitrification. Aura measurements of temperature, H_2O, HNO_3, and aerosol extinction will be used to assess differences in PSC character and denitrification between volcanically perturbed and quiescent periods.
- **How do volcanoes affect stratospheric ozone?** Dynamical effects associated with volcanic aerosol can reduce column O_3 in the tropics, while perturbations to nitrogen and chlorine partitioning can cause increased chemical O_3 depletion at mid/high latitudes [e.g., Solomon, 1999]. Possible cooling of the stratosphere, and increases in H_2O, may exacerbate ozone depletion even under background aerosol conditions and will likely have a still greater effect under enhanced aerosol conditions following a major volcanic eruption. The MLS, and other Aura, measurements provide a suite of measurements for quantifying these effects.

4.2. Tropospheric Ozone and Pollution

What are the effects of regional pollution on the global atmosphere, and the effects of global chemical and climate changes on regional air quality?

Tropospheric ozone, an important pollutant and contributor to urban smog, has increased since pre-industrial times. In addition to its more direct effects on air quality, tropospheric ozone is a source for OH which regulates air's ability to cleanse itself of many polluting and greenhouse gases. Aura is a major step forward in tropospheric observations, with TES global measurements of many species. MLS complements TES in the upper troposphere, with some science objectives itemized below, and MLS measurements can be made in the presence of (and through) cirrus that degrade TES data. MLS single profile measurement precision will generally be sufficient for H_2O, temperature and O_3 in the upper troposphere. Biweekly or monthly maps will generally be needed for CO, CH_3CN and HCN – but single profiles will be useful when abundances are substantially enhanced (e.g., by biomass burning). Correlative aircraft measurements, valuable for many MLS (and Aura) science objectives, are especially important for several aspects of the MLS tropospheric studies (e.g., validation, better precision and spatial resolution, complementary data, and extending the analysis range into the lower troposphere).

- **What is the quantitative connection between global upper tropospheric pollution and biomass burning/surface pollution?** Biomass burning is known to be a significant contributor to tropospheric column O_3 enhancements over the South Atlantic [e.g., Fishman et al., 1990] and to CO enhancements in the Pacific upper troposphere [Matsueda et al., 1999]. Direct linkage between biomass burning and upper tropospheric pollutant enhancement events has been established [Andreae et al., 2001]. A localized enhancement in lower stratospheric CH_3CN detected and tracked by UARS MLS has been traced to an intense thunderstorm's injection of forest fire pollution into the stratosphere [Livesey et al., 2003]. An EOS MLS objective is to better quantify such events and their global effect. Correlations of MLS O_3, CO, CH_3CN and HCN will provide data on the sources of O_3 and CO enhancements. Such studies will be optimized through the use of several Aura products (e.g., NO_2 column and aerosol from OMI; O_3, CO and CH_4 from TES).
- **Can we determine and understand global tropospheric column ozone variations?** Stratospheric column ozone from MLS (and HIRDLS) will be used in combination with OMI total ozone column to produce daily maps of tropospheric ozone residual (TOR) column. Tropospheric column ozone quality, improved over that previously available, is expected from the OMI-MLS (and OMI-HIRDLS) TOR products; these will supplement tropospheric ozone columns measured directly by TES (which typically will have a 50% duty cycle). These data will be compared to 3D models (as constraints for improving tropospheric models).
- **What is the global upper tropospheric ozone distribution/budget?** Upper tropospheric ozone measurements from MLS, TES and HIRDLS will be used to produce a more detailed global description of the upper tropospheric ozone field, and its budget/variations, than has previously been possible. Aura global tropospheric data should dramatically increase constraints on tropospheric models. Stratosphere-troposphere exchange is a significant source for ozone in the upper troposphere [Lelieveld and Dentener, 2000], and improvements in estimates of ozone flux from the stratosphere (and model parameterizations of it) should be possible with Aura data. MLS measurements in the presence of cirrus and HIRDLS high-resolution measurements are especially important in this regard.

- **Can we determine and understand interannual and longer-term upper troposphere changes?** While seasonal variations of upper tropospheric O_3 seem to be fairly well captured by models [e.g., Law et al., 2000], better characterization and understanding of longer-term changes are needed. Pollution transport is episodic [e.g., Yienger et al., 2000] and requires understanding on a global, interannual, and long-term basis. This includes issues such as variability related to El Niño and expected increases in pollution from Asia. Constraints from Aura data should improve our ability to determine tropospheric changes.

4.2. Climate Variability

What trends in atmospheric constituents and solar radiation are driving global climate?

How well can transient climate variations be understood and predicted?

How well can long-term climate trends be assessed or predicted?

How well can future atmospheric chemical impacts on ozone and climate be predicted?

4.2.1. Climate Processes Involving Upper Tropospheric H_2O [3]

A key uncertainty in predicting future climate changes is the response of tropospheric H_2O to changes in other greenhouse gas concentrations. The small amounts of H_2O in the upper troposphere (UT) have a particularly strong infrared radiative effect, due to the low temperatures there, and exert enormous leverage on Earth's radiative balance. Increases in upper tropospheric H_2O within global climate models result in much greater radiative effects at the surface than are caused solely by the build-up of CO_2 and other greenhouse gases [e.g., Shine and Sinha, 1991]. Of particular importance is the moisture in the dry subtropical regions, which has a large cooling effect on the whole tropics [Spencer and Braswell, 1997]. There is large uncertainty on the actual abundance of H_2O in this region, due to lack of data.

Understanding the mechanisms that control humidity of the tropical troposphere is key to determining the nature of its feedback on climate, and is thus essential for improving climate change predictions. The subtropics are not as dry as the simple picture of outflow and subsidence from equatorial convective regions would imply – hence there must be additional moisture sources that hydrate the regions of the tropics characterized by descent. There are three hypotheses for the sources of this moisture: (1) evaporation of precipitation, (2) evaporation of detrained cloud particles, and (3) lateral transport. The relative contribution of these sources to subtropical moisture has major implications on how subtropical humidity will change in response to climate change and, hence, major implications for the water vapor feedback on climate [e.g., Pierrehumbert, 2000]. Improving our understanding of these sources is crucial for climate models to accurately simulate tropospheric water vapor and its feedbacks.

- **What is the distribution of upper tropospheric water vapor, and how does it vary on seasonal and interannual time scales?** EOS MLS will provide accurate H_2O measurements in the tropical and subtropical upper troposphere, even in the presence of cirrus where observations by other techniques can be flawed. These measurements will enable the distribution and temporal variation of upper tropospheric humidity (UTH) to be accurately determined. The better accuracy and precision, and spatial and temporal coverage, of EOS

[3] Dr. Darryn Waugh contributed material in this section.

MLS compared to UARS MLS – and its extension of the UARS data set over a longer time period – will further improve our knowledge of UTH.

- **What are the processes controlling upper tropospheric humidity?** Joint analysis of the MLS UTH measurements and the location and strength of deep convection and the circulation (e.g., from outgoing longwave radiation measurements) will improve understanding of how deep convection affects upper tropospheric humidity. Aura measurements of tracers will provide information on the origin of the air mass, and may place further constraints on the hydration paths for upper tropospheric water. MLS measurements of cloud ice content will provide important data on the supply of water to the upper troposphere – helping, for example, determine what fraction of water in a convective air parcel remains in condensed form that can rapidly fall out. Variation in the observed UTH over seasonal through interannual time scales will provide insight into how different forcings, such as El Nino, may affect climate variability. Observed UTH will help determine how well models can reproduce the observed distribution, and thus will test our understanding of processes controlling upper tropospheric H_2O (e.g., comparisons with models that determine the humidity by tracing air parcels to the temperature of last saturation will test the "lateral transport" hypothesis).

4.2.2. Radiational Effects of Stratospheric O_3 and H_2O on Climate

- **How might changes in stratospheric O_3 and H_2O affect stratospheric climate?** In addition to effects on stratospheric temperature, O_3 and H_2O changes are expected to affect stratospheric circulation in ways difficult to predict. As well as direct effects (e.g., influence of the change in heating/cooling on the vertical static stability and meridional temperature gradients), there is a feedback via geostrophic balance on the magnitude of zonal mean winds. This impinges on the propagation of tropospheric planetary waves into the stratosphere and the rate at which they are damped and dissipated, affecting strength of the diabatic circulation. Understanding the interaction of these processes entails calculation of 3D heating and cooling fields, which requires accurate H_2O and O_3 throughout the stratosphere. There is wide disparity in the calculated effects of changes in O_3 and H_2O on stratospheric temperature. A major source of the disparity is uncertainty in the vertical distribution of stratospheric H_2O trends [Shine and Sinha, 1991]. MLS and HIRDLS will accurately measure O_3 and H_2O in the region of most uncertainty, allowing effects of future changes to be more accurately predicted.
- **How might changes in stratospheric O_3 and H_2O affect forcing of surface temperature?** Greenhouse forcing of surface temperature is significantly influenced by radiative effects of O_3 and H_2O in the lower stratosphere and around the tropopause [IPCC, 2001]. A given *fractional* change in O_3 has the largest effect on surface forcing when it occurs in the upper troposphere and lower stratosphere [Forster and Shine, 1997], but O_3 changes in these regions are poorly characterized. As a consequence, understanding of greenhouse forcing by stratospheric O_3 changes is now classified as only 'medium' [IPCC 2001]. Radiative forcing by stratospheric H_2O trends is expected to be comparable (and opposite in sign) to that due to O_3 depletion [Forster and Shine, 2002]. The important contribution to surface forcing by H_2O in the near-tropopause region, where its distribution and variation are poorly characterized, has been highlighted in a number of studies. Aura measurements of O_3 and H_2O will reduce uncertainties in their contributions to future changes.

4.2.3. Climatic Effects of Volcanic SO_2

- **How does volcanic SO_2 injected into the stratosphere affect climate?** Volcanoes can inject large amounts of SO_2 into the stratosphere. This is converted by reaction with OH into sulfuric acid, which condenses into aerosols whose scattering of shortwave solar radiation leads to surface cooling, and whose absorption of upwelling longwave radiation leads to lower stratospheric

heating. If there are volcanic injections of SO_2 into the stratosphere during the MLS operational lifetime, the MLS measurements of SO_2 and OH vertical profiles will allow more stringent tests than previously possible for models of stratospheric aerosol formation from volcanic SO_2. Its measurements of temperature, tracers, and geopotential height – all of which can be made in the presence of dense aerosol – will provide unique information on the short term response of stratospheric temperature and circulation to aerosol increases.

4.3. Summary of EOS MLS measurement objectives

Figure 4-1 summarizes the EOS MLS scientific measurement objectives. Accuracy and precision for the measurements are summarized in section 8. Information on precision and resolution for all measurements are given in Filipiak et al. [2004].

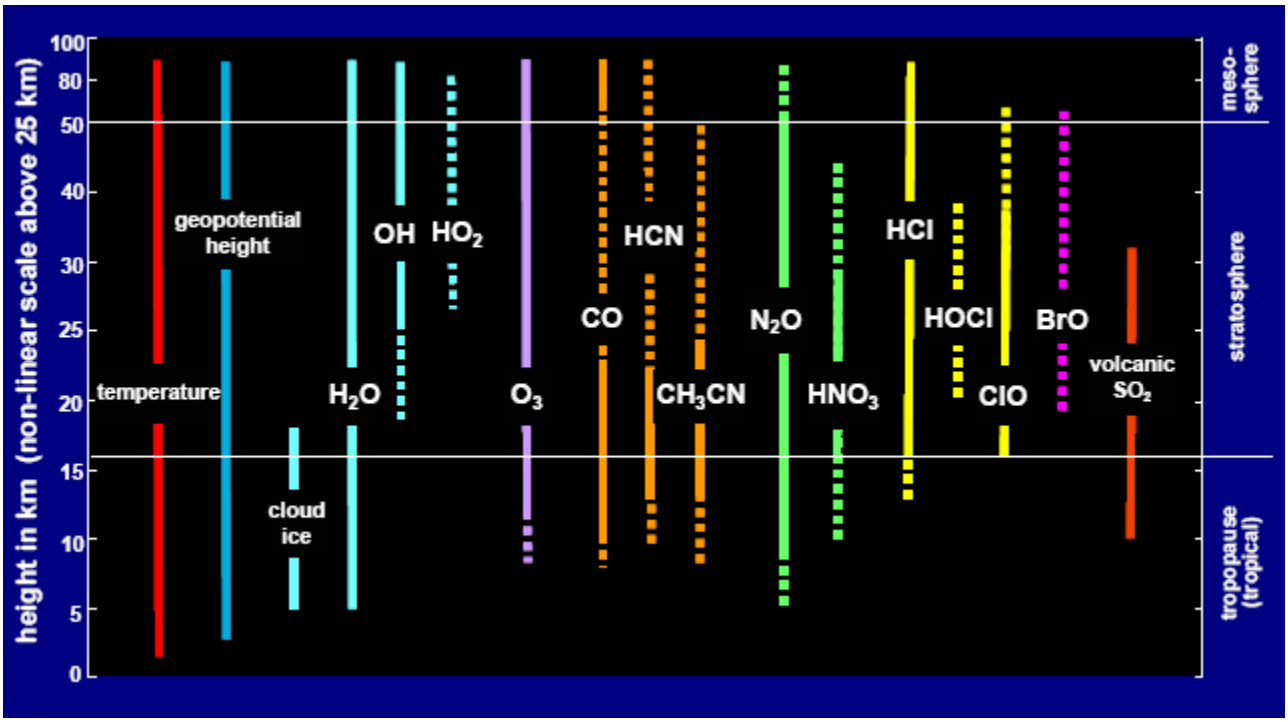

Figure 4-1. EOS MLS scientific measurement objectives. Solid lines indicate useful individual profiles and/or daily maps. Dotted lines indicate that zonal (or other) averages will likely be needed to obtain useful precision. It should be noted that 'useful profiles' indicated by the solid lines here do not necessarily apply at all times of day and night due to diurnal variation in some species, particularly OH, HO_2, ClO and BrO. Also, they do not necessarily apply at all latitudes due to latitudinal variation in abundances. For example, although useful individual profiles of lower stratospheric HNO_3 will be obtained at mid and high latitudes, they are not expected in the tropics because of the smaller HNO_3 abundances at low latitudes.

5. The EOS MLS Instrument

5.1. Complement of radiometers

The EOS MLS instrument has radiometers in five spectral regions, chosen to produce the standard geophysical data products from MLS stated in the May 1995 EOS Execution Phase Project Plan [NASA Goddard Space Flight Center, 1995] and given below in Table 5-1. The 118 GHz radiometer, covering the strong 118 GHz O_2 line, was chosen to optimize trade-offs between precision and vertical resolution for temperature and tangent pressure. The 190 GHz radiometer was chosen to measure the 183 GHz H_2O line, as done by UARS MLS, and to measure a strong band of HNO_3 lines. The 240 GHz radiometer was chosen to cover very strong O_3 lines in a spectral region where upper tropospheric absorption (mainly by water vapor continuum) is sufficiently small to allow measurements of upper tropospheric O_3. The 640 GHz radiometer was chosen to measure the lowest-frequency line of HCl, the strongest rotational line of ClO (more than 10× stronger than the 204 GHz line measured by UARS MLS), and a strong N_2O line. The 2.5 THz radiometer is chosen for OH because of the relatively clean spectral region around the pair of strong OH lines at 2.510 and 2.514 THz, and because of the availability of a methanol gas laser to use as local oscillator for this radiometer.

These radiometers provide additional measurements, indicated in Table 5-1, which are now standard data products for MLS as stated in the EOS Aura Project Plan [NASA Goddard Space Flight Center, 1999]. Additional contributions from the radiometers are also stated in the table.

Planar-technology mixers [Siegel et al., 1993] are used in all the radiometers, with a monolithic millimeter-wavelength integrated-circuit (MMIC) amplifier [Weinreb et al., 1997] preceding the mixer in the 118 GHz radiometer. Subharmonically-pumped mixers are used at 118, 190, 240 and 640 GHz, and a fundamental mixer at 2.5 THz. Local oscillators are solid state, except at 2.5 THz, where a CO_2-pumped methanol (CH_3OH) gas laser is used. All radiometers operate at ambient temperature.

Table 5-1. MLS geophysical data products and radiometers.

MLS Standard Data Products from May 1995 EOS Project Plan, GSFC 170-01-01, Rev A	**Radiometers for the Standard Data Products in left column**	**Additional measurements by the radiometers, set as Standard Data Products for MLS in the April 1999 CHEM Project Plan**	**Additional contributions by the radiometers**
temperature, geopotential height	118 GHz (R1)	contributes to cloud ice product	tangent pressure measurement needed for other measurements, improves quality of upper trop H_2O
H_2O HNO_3	190 GHz (R2)	HCN, contributes to cloud ice product	ClO (lower quality than from 640 GHz), N_2O (lower quality than from 640 GHz), O_3 (but not in upper trop), CH_3CN, SO_2
O_3	240 GHz (R3)	CO, contributes to cloud ice product	temperature and tangent pressure, HNO_3, improves quality of upper trop H_2O
HCl, ClO, N_2O	640 GHz (R4)	BrO, HOCl, HO_2, volcanic SO_2, contributes to cloud ice product	stratospheric O_3 with better vertical resolution than 240 GHz (but does not measure O_3 in upper trop), CH_3CN, improves quality of upper trop H_2O
OH	2.5 THz (R5)	contributes to cirrus ice product	pressure over limited vertical range (needed for OH measurement)

5.2. Signal flow

Figure 5-1 shows a signal flow block diagram for the instrument. Atmospheric signals for the 118, 190, 240 and 640 GHz radiometers are collected by a three-reflector antenna system which vertically scans the limb. As needed, the antenna is scanned to higher altitudes for a view of 'cold space' through the complete antenna system. The antenna design is very similar to that of UARS MLS, with a primary reflector dimension of 1.6 m projected in the vertical direction at the limb tangent point. A switching mirror following the GHz antenna system provides radiometric calibration by switching to views of calibration targets or to space. An optical multiplexer, consisting of an arrangement of dichroic plates and polarization grids as shown in Figure 5-2, spatially separates the signal from the switching mirror into different paths for the different radiometers. A second 118 GHz radiometer ('R1B', at the orthogonal polarization) provides redundancy for temperature and pressure, but – under nominal operation – is not turned on.

The atmospheric and calibration signals for the 2.5 THz radiometer are obtained via a dedicated telescope and scanning mirror whose operation is synchronized with that of the GHz antenna and the GHz switching mirror. The 2.5 THz primary mirror dimension in the 'limb vertical' direction is ~25 cm. The 2.5 THz measurements are performed simultaneously at both polarizations to increase the signal to noise ratio for the important OH measurement.

The radiometers have intermediate frequency (IF) outputs in several bands as described later in section 5.3. These IF outputs are fed, via a switch network, to spectrometers. The switch network provides some redundancy, and can be used to improve efficiency in the unexpected event that time-sharing of measurements is required because of power limitations (see section 5.8). Digitized data from the spectrometers are passed to the command and data handling system for transmission to the ground. The instrument individual measurement integration time is nominally 1/6 second, termed an MLS Minor Frame (MIF). The MLS Major Frame (MAF) is the time over which a complete limb scan is taken; a MAF normally consists of 148 MIFs (24.7s), but occasionally has 149 MIFs for synchronization of the MLS limb scan with the Aura orbit.

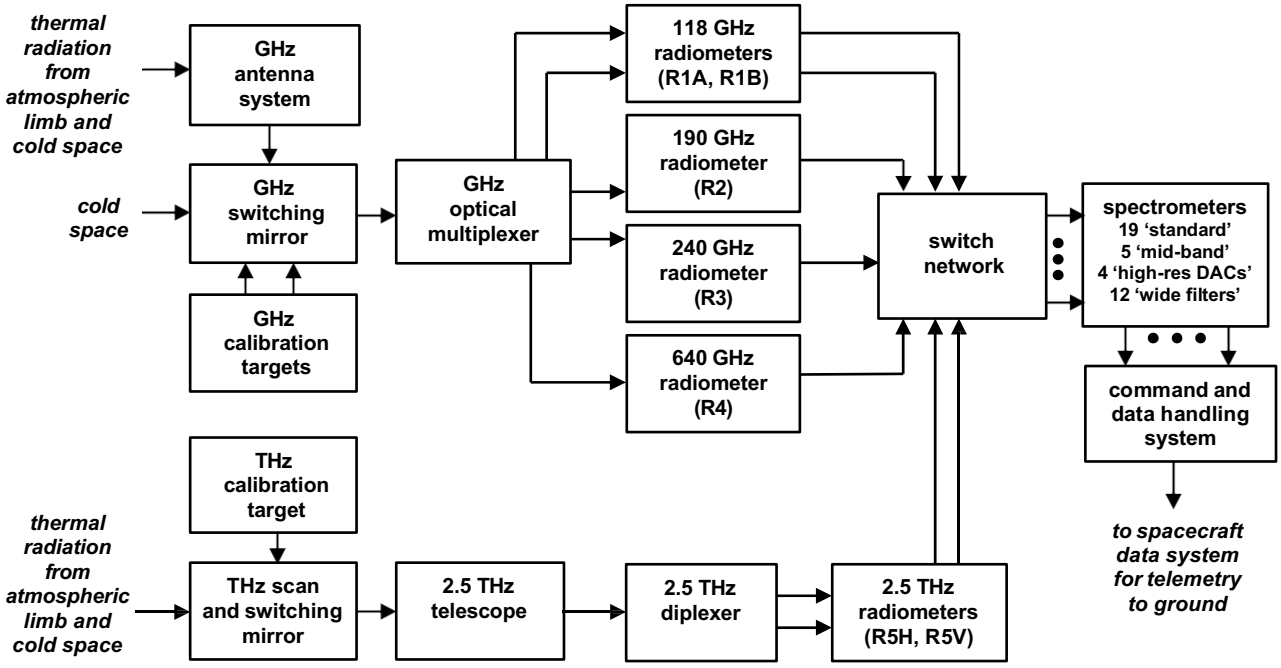

Figure 5-1. EOS MLS signal flow block diagram.

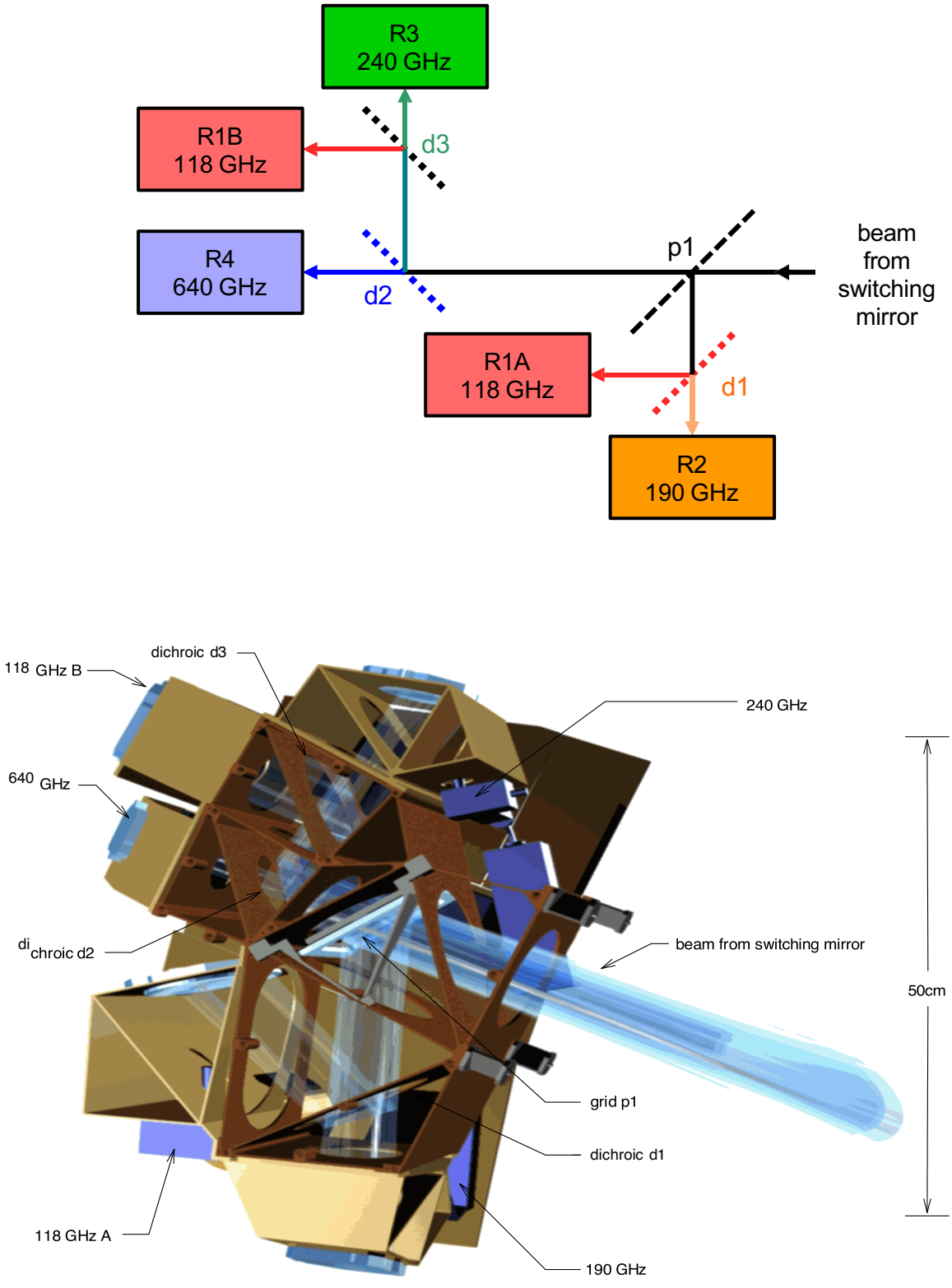

Figure 5-2. Schematic (top) and design (bottom) of the optical multiplexer for the EOS MLS GHz radiometers. "pn" denotes a polarization grid and "dn" denotes a dichroic plate; these components separate different polarizations or frequency bands.

5.3. Spectral regions

The spectral regions used for measurement by EOS MLS, shown in Figure 5-3, resulted from an investigation to minimize the number of radiometers and spectrometers needed to accomplish the scientific objectives of the experiment, while reliably producing its data products with the required accuracy and resolution.

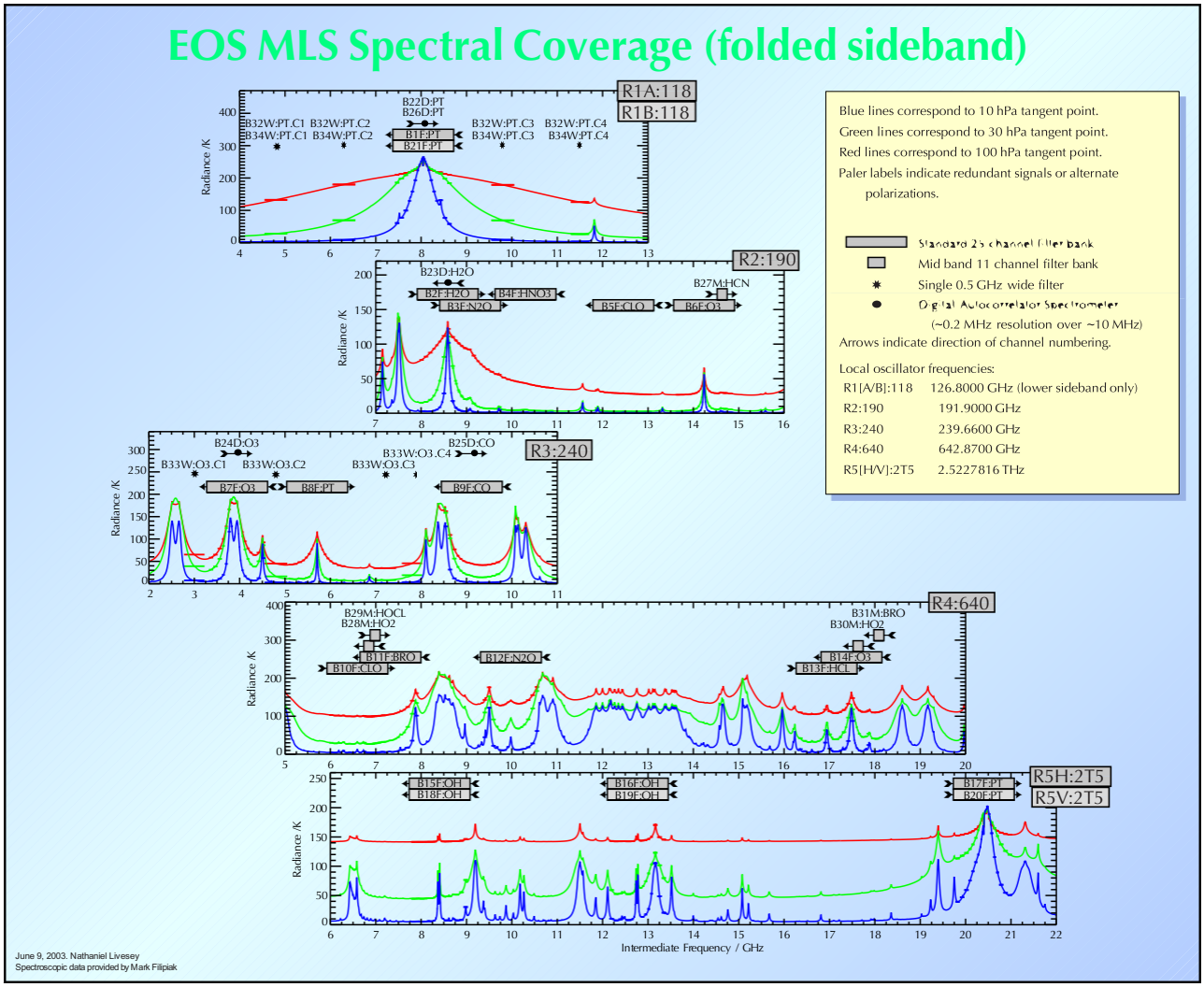

Figure 5-3 (from Livesey and Snyder [2004]). Atmospheric spectral regions measured by EOS MLS. They grey boxes and other symbols denote the position of various bands covered by different radiometers, with indications of the targeted measurement for each (PT indicates pressure/temperature). There is a separate panel for each radiometer, and the horizontal axis of each is the intermediate frequency at the output of the mixer (see top portion of Figure 5-2) output. The red, green and blue curves are the calculated atmospheric limb spectra at 100, 30 and 10 hPa tangent pressure. More information is given in the yellow inset in the figure. See Appendix E of Livesey and Snyder [2004] for details on the notation used to designate the various EOS MLS radiometers, bands, and channels.

Figure 5-4 shows chemical species measured by individual EOS MLS radiometers.

Table 5-2 (on the following page) gives some specifics for the MLS spectral regions, including frequencies of the targeted spectral lines and the maximum expected radiometer noise in each region. There are separate estimates for the noise in the spectrally-varying component of the calibrated radiance and in the spectrally-averaged component of the radiance, as defined in notes 6 and 7 of Table 5-2. The primary molecule to be observed in each region, its expected typical abundance, the targeted spectral line, and the expected signal intensity are also given.

Most MLS data products are obtained from the spectrally-varying component of the radiance, and different scientific uses for the same data product require different precisions, which depend upon the amount of averaging and spectral resolution used in the analyses. The spectrally-averaged component of the radiance is used at the lowest ends of the measurement height range to provide information on temperature, H_2O, and cloud ice.

Any radiometer responses in extraneous spectral regions, which might be converted into signals at the IF frequencies of spectral regions targeted for measurements, are at least 30 dB lower than for the targeted regions. Any responses of the 240 GHz radiometer within 3 GHz of the 118 GHz O_2 line are at least 40 dB lower than in its targeted regions. This ensures that any unwanted atmospheric signal will contribute less than 0.3 K brightness to the received signal, and limits contamination of the 240 GHz upper tropospheric O_3 measurements to less than 0.03 K by the strong 118 GHz O_2 line.

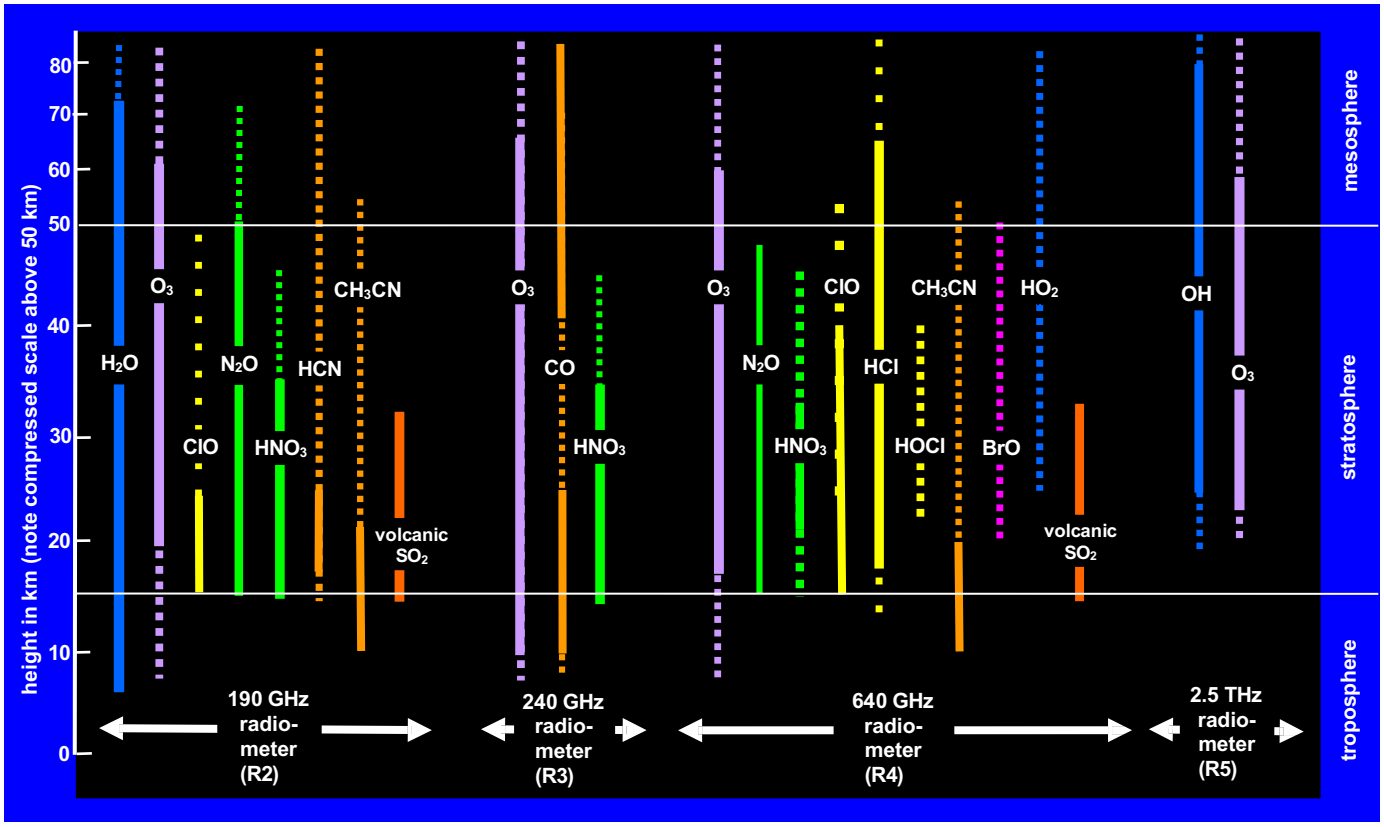

Figure 5-4. Chemical species measured by individual EOS MLS radiometers. (All radiometers contribute to measurement of temperature, geopotential height and cloud ice.) Solid lines indicate useful individual profiles and/or daily maps. Dotted lines indicate that zonal (or other) averages are generally needed to obtain useful precision. Solid lines for CH_3CN and 190 GHz ClO are for enhanced abundances (biomass burning injections of CH_3CN, and polar winter vortex ClO).

Table 5-2. Some specifics for the spectral regions measured by EOS MLS.

radiometer and LO frequency (see note 1) (GHz)	primary targeted molecule	abundance expected (see note 2) (vmr)	spectral line frequency (see note 3) (GHz)	expected signal intensity (see note 2) (K, SSB)	measured spectral region: Doppler-shifted 'sky' freq (see note 4) (GHz)	measured spectral region: IF freq (see note 4) (GHz)	MLS spectral band(s) (see note 5)	T_{sys} (K,SSB)	instrument noise (see notes 6 and 7) spectrally-varying component (K, SSB): ΔI for 1/6 s: 6 MHz	ΔI for 1/6 s: 96 MHz	ΔI for 1/6 s: 500 MHz	ΔI_{min}
R1 (A&B) 118 GHz 126.800 (÷2 = 63.400)	O_2 wing	2.1E-01		1-300	115.3	-11.5	B32W.C1	1200			0.1	0.1
	O_2 wing	2.1E-01		1-300	117.0	-9.8	B32W.C2	1100			0.1	0.1
	O_2	2.1E-01	*118.7503	1-300	118.7530	-8.0470	B1F & B22D	1300	1.3	0.3		0.1
	O_2 wing	2.1E-01		1-300	120.5	-6.3	B32W.C3	1200			0.1	0.1
	O_2 wing	2.1E-01		1-300	122.0	-4.8	B32W.C4	1700			0.2	0.1
R2 190 GHz 191.900 (÷2 = 95.950)	H_2O	5E-06	183.3101	1-300	183.3142	-8.5858	B2F & B23D	2200	2.3	0.6		0.1
	N_2O	1E-07	200.9753	15	200.9798	9.0798	B3F	2300	2.3	0.6		0.1
	HNO_3	1E-09	181.5946	5	181.5987	-10.3013	B4F	2000	2.0	0.5		0.1
	ClO	5E-10	*204.352	0.4	204.3566	12.4566	B5F	2000	2.0	0.5		0.03
	O_3	1E-05	206.1320	1-100	206.1367	14.2367	B6F	1800	1.8	0.6		0.1
	HCN	1E-10	177.2612	0.5	177.2652	-14.6348	B27M	1800	1.8	0.6		0.1
R3 240 GHz 239.660 (÷2 = 119.830)	O_3 wing	5.0E-08		0.2		+/- 3.0	B33W.C1	2400			0.3	0.1
	O_3	5.0E-08	235.7098	2	235.7151	-3.9449	B7F & B24D	2800	2.8	0.7		0.1
	O_3 wing	5.0E-08		0.2		+/- 4.8	B33W.C2	3600			0.4	0.1
	^{18}OO	8.0E-04	233.9462	1-100	233.9515	-5.7085	B8F	3200	3.2	0.8		0.1
	O_3 wing	5.0E-08		0.2		+/- 7.2	B33W.C3	2700			0.3	0.1
	O_3 wing	5.0E-08		0.2		+/- 7.8	B33W.C4	2700			0.3	0.1
	CO	1.0E-07	230.5380	1.5	230.5432	-9.1168	B9F & B25D	2400	2.4	0.6		0.1
R4 640 GHz 642.870 (÷2 and ÷3 = 107.145)	ClO	5.0E-10	*649.4512	8	649.4659	6.5959	B10F	10,000	10	3		0.1
	HO_2	5.0E-10	649.7015	1	649.7162	6.8462	B28M	10,000	10			0.1
	HOCl	2.0E-10	635.8700	0.7	635.8844	-6.9856	B29M	10,000	10			0.1
	^{81}BrO	5.0E-12	*650.179	0.1	650.1937	7.3237	B11F	10,000	10	3		0.1
	N_2O	1.0E-07	652.8338	80	652.8485	9.9785	B12F	10,000	10	3		0.1
	HCl	2.0E-09	*625.9188	50	625.9327	-16.9373	B13F	10,000	10	3		0.1
	O_3	1.0E-05	625.3715	1-200	625.3856	-17.4844	B14F	10,000	10	3		0.1
	HO_2	5.0E-10	660.4857	1	660.5006	17.6306	B30M	10,000	10			0.1
	^{81}BrO	5.0E-12	*624.768	0.1	624.7821	-18.0879	B31M	10,000	10			0.1
R5 (V&H) 2.5 THz 2522.7816 (see note 8)	OH (H)		*2514.3167	0.2-100	2514.3735	-8.4081	B15F	20,000	20	5		0.2
	OH (V)	5.0E-13 to	*2514.3167	0.2-100	2514.3735	-8.4081	B18F	15,000	15	4		
	OH (H)	1.0E-09	*2509.9490	0.2-100	2510.0057	-12.7759	B16F	20,000	20	5		0.2
	OH (V)		*2509.9490	0.2-100	2510.0057	-12.7759	B19F	15,000	15	4		
	O_2 (H)	2.1E-01	*2502.3239	1-300	2502.3804	-20.4012	B17F	60,000	60	15		0.1

Note 1: The R1 and R5 local oscillator (LO) frequencies were selected from engineering considerations; others were chosen to provide atmospheric measurements from both the lower and upper sidebands. R1 is single sideband and all others are double sideband, and there are two (A&B) R1 radiometers; R1B is a redundant radiometer that is normally turned off. The '(÷ 2 = *f*)' below the LO frequency gives the frequency *f* of the fundamental oscillator used to generate the LO. There is an additional ÷ 3 for the 640 GHz radiometer because a frequency-tripler is also used there, as well as its mixer being subharmonically pumped like the 118, 190 and 240 GHz radiometers.

Note 2: Values here are typical of what is expected over certain vertical ranges to be covered by MLS; 'vmr' is volume mixing ratio.

Note 3: Spectral lines having fine structure are marked by *.

Note 4: Doppler-shifted values are for MLS looking forward in 700 km orbit. A negative number in the 'IF freq' column indicates the spectral line is in the radiometer lower sideband; ± indicates signals from the targeted molecule are in both upper and lower sidebands.

Note 5: Bn indicates MLS spectral band n. BnF indicates a 'standard' 25-channel filter bank is used for this band, BnM indicates an 11-channel 'mid-band' filter bank is used, BnD indicates a high-resolution digital autocorrelator 'DAC' is used, and BnW.cm indicates a wide filter (channel m of band n) is used. These are described in section 5.4 of this document. More information on the MLS band nomenclature is in Appendix E of Livesey and Snyder [2004].

Note 6: The expected 1σ noise in the spectrally-varying component of the radiance (single sideband, after calibration, difference in measurments from one channel or filter to another throughout a given radiometer) is the greater of $\Delta I_{min}/3$ or $T_{sys}/\mathrm{sqrt}(B\tau)$, where ΔI_{min} and T_{sys} are given in the table above, B is the noise bandwidth, and τ is integration time for which the measurement is accumulated. ΔI_{min} is the minimum signal to be measured. The value of τ can range from 0.17 s (a single instrument integration time) to ~1 hour (the approximate integration time for producing monthly zonal means with ~3 km vertical and ~5° latitude resolution) or more. Values of the expected noise for the individual 1/6 s instrument integration time are given in the columns labeled 'ΔI for 0.17 s' (at 6 and 96 MHz bandwidths for regions measured by standard and midband spectrometers, and at 500 MHz bandwidth for regions measured by the wide filters). All values are in single-sideband units, and are approximate average values for each band from measurements made on the completed MLS flight instrument.

Note 7. The expected 1σ noise in the spectrally-averaged component of the radiance from each radiometer (single sideband, after calibration, average value of measurements over all channels of the radiometer) measured in an individual 0.17 s integration period is $4\times10^{-4} \times T_{sys}$ or less for R1, R2, R3 and R4 - and $2\times10^{-3} \times T_{sys}$ or less for R5.

Note 8: Measurements are made in both polarizations (H & V) and are averaged to reduce the noise during retrievals of OH.

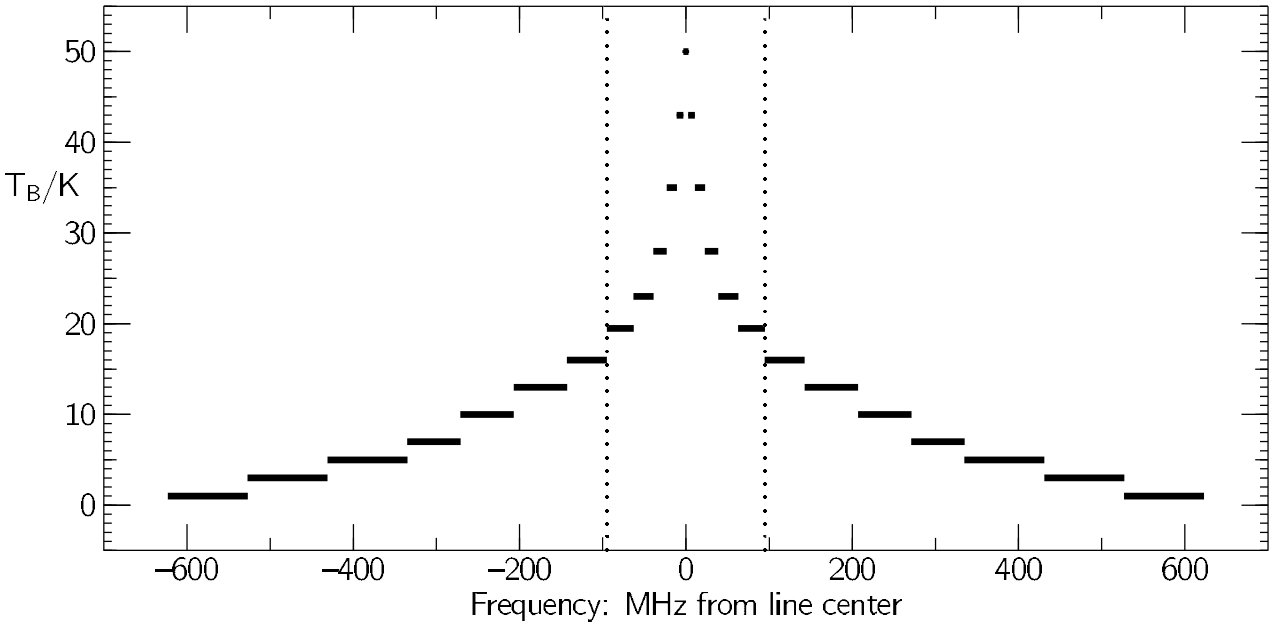

Figure 5-5. Coverage of the EOS MLS 'standard' 25-channel spectrometer. Each filter in the spectrometer is shown as a horizontal bar whose width gives the filter resolution. The 11 filters located between the dotted vertical lines also occur in the EOS MLS 'mid-band' spectrometers. The signal illustrated here is the 206 GHz O_3 line shown earlier in Figure 3-3 measured by UARS MLS, and extended outward to the broader spectral coverage of EOS MLS.

5.4. Spectrometers

Four types of spectrometers are used in EOS MLS, having different spectral resolutions and bandwidth. They broadly cover the different altitude ranges over which measurements are needed. Measurements at lower altitudes require more spectral coverage, but less resolution, than do measurements at higher altitudes.

'Standard' 25-channel spectrometers are the primary source of information for measurements throughout the stratosphere (atmospheric pressure range from ~100 to ~1 hPa), which require spectral coverage of ~1300 MHz at the lower altitudes and resolution of ~6 MHz at the higher altitudes, as can be seen from Figure 3-3. These spectrometers are indicated by 'BnF' in the 'MLS spectral band(s)' column of Table 5-2. Individual channel positions (frequency relative to the down-converted frequency of the measured spectral line) and widths (full width between the half-power points of the channel response) are given in Table 5-3, and illustrated in Figure 5-5. Filters for individual channels have a response typical for a 5-6 pole Tchebychev filter.

Table 5-3. Positions (relative to spectral line center) and widths (full widths between half power points) of channels in the 'standard' 25-channel spectrometers. Values for channels 8 to 18 also apply to the 'midband' spectrometers.

channel number	position (MHz)	width (MHz)	channel number	position (MHz)	width (MHz)	channel number	position (MHz)	width (MHz)
1	-575	96	8	-79	32	19	119	48
2	-479	96	9	-51	24	20	175	64
3	-383	96	10	-31	16	21	239	64
4	-303	64	11	-17	12	22	303	64
5	-239	64	12	-7	8	23	383	96
6	-175	64	13	0	6	24	479	96
7	-119	48	14	7	8	25	575	96
			15	17	12			
			16	31	16			
			17	51	24			
			18	79	32			

'Midband' spectrometers, consisting of the center 11 channels (numbered 8 to 18) in Table 5-3, are used for additional measurements in the middle and upper stratosphere (atmospheric pressures from ~10 to ~1 hPa). These spectrometers are indicated by 'BnM' in the 'MLS spectral band(s)' column of Table 5-2. Locations of individual filters in these spectrometers are also shown in Figure 5-5.

'Digital autocorrelator' (DAC) spectrometers provide the resolution needed for mesospheric measurements of temperature, H_2O, O_3 and CO. These have 129 channels covering 10 MHz spectral width, with each channel having resolution of ~0.15 MHz to measures narrow spectral lines at atmospheric pressures below ~1 hPa (see Figure 3-2), and are indicated by 'BnD' in the 'MLS spectral band(s)' column of Table 5-2. The 'standard' spectrometers provide adequate spectral resolution for the mesospheric OH signals that have a Doppler-broadened halfwidth of ~3 MHz (see Figure 3-2), which is well matched to the 6 MHz resolution of the center channels of the standard spectrometers.

'Wide' filters, having 0.5 GHz width, extend the spectral range of the 25-channel spectrometers for measurements extending down into the troposphere. These filters are at spectral locations indicated by 'BnW' in the 'MLS spectral band(s)' column of Table 5-2, and are illustrated in Figures 5-3 occurring earlier in this document.

The instrument contains a total of 19 'standard' spectrometers, 5 'mid-band' spectrometers, and 4 DAC spectrometers. There are 12 'wide' filters organized into 3 'bands' of 4 channels (one band each in R1A, R1B and R3).

The position and width of each GHz channel are known to within 1% of the full width between half power points. This ensures that the channel position and resolution are within an acceptable range for gathering the needed information. The fraction of spectrally-flat input power received within each channel's width is 0.85 or greater. This ensures that signals received by each filter arise mainly from the targeted region.

The frequency stability of channel responses (at frequencies of the maximum response and the –10 dB points on the edges), including cumulative effects of all down-conversions except that of the first local oscillator for the 2.5 THz radiometer, is better than 0.01 MHz over time periods up to 1 minute. This ensures that frequency shifts of the channel response over an individual limb scan are less than 1% of the spectral line Doppler width for the GHz channels, and less than the Doppler width for the 2.5 THz channels. The requirement on the GHz channels is tighter because the Doppler shift of atmospheric spectral lines may be determined during analyses of data from certain of these channels. The 2.5 THz local oscillator frequency can slowly drift over a range of approximately ± 2 MHz, and is determined during ground data processing.

Over time periods from 1 minute up to the life of the instrument, either the frequency stability, or knowledge of drifts in frequency of the channel responses, is better than 0.5% of the channel width for the GHz bands, including cumulative effects of all down-conversions. This ensures that long-term drifts will not significantly degrade the quality of geophysical measurements retrieved from the data. The same specification applies to the THz bands but without including the effects of frequency down-conversion from the first local oscillator since those effects will be accounted for during data processing.

5.5. Field-of-view (FOV)

The beamwidths, beam efficiencies, and placement and coincidences of boresights are key parameters for the EOS MLS instrument field-of-view performance.

'FOV beamwidth' is defined as the angle between the half-power points of the antenna response. 'Beam efficiency' is defined as that fraction of power from an isotropic source which is collected within a specified angular range centered at the antenna boresight. The MLS FOV beamwidths and beam efficiency are set by the vertical resolution needed for the measurements. The values chosen are an acceptable compromise between the scientific desire for better vertical resolution, and the engineering/accommodation difficulties associated with the increase in antenna size required for better resolution. They correspond to an antenna for the GHz channels that is the same size as for the UARS MLS, but the shorter-wavelength EOS MLS measurements provide better vertical resolution than those from UARS MLS.

The EOS MLS FOV beamwidths are given in Table 5-4. The beam efficiency within an angular range of 2.5 times the beamwidth is 0.95 or greater.

Table 5-4. EOS MLS field-of-view beamwidths (full width between half-power points)

Radiometer	FOV beamwidth in vertical plane at the limb tangent point	FOV beamwidth in horizontal plane at the limb tangent point
118 GHz (R1)	6.5 km	13 km
190 GHz (R2)	4.5 km	9 km
240 GHz (R3)	3.5 km	7 km
640 GHz (R4)	1.5 km	3 km
2.5 THz (R5)	2.5 km	2.5 km

The angular pattern of the EOS MLS FOV response is similar to that for UARS MLS. Measurements of the EOS MLS FOV response at 234 GHz (frequency used for obtaining pointing information) is shown in Figure 5-6. The noise floor on the measurements shown in Figure 5-6 is ~60 dB (10^{-6}) below the peak boresight value of the response.

'FOV boresight' is defined as the direction given by the peak value of the Gaussian function that best fits the antenna response down to the -10 dB power points. FOV boresights of the 190, 240 and 640 GHz radiometers coincide with the 118 GHz FOV boresight to within one-fifth of the 118 GHz beamwidth. Direction of the 2.5 THz FOV boresight relative to the direction of the 118 GHz FOV boresight will be known to within one-fifth of the 118 GHz beamwidth. The scan plane of the 2.5 THz boresight is within 10 km of that of the 118 GHz boresight at the atmospheric limb tangent point, over the tangent height range of 10 to 60 km, and the THz and GHz scans are synchronized to within one individual instrument integration period (1/6 second).

To ensure efficient coverage of the vertical region of interest, the accuracy in placement of the tangent height of the FOV boresights, after in-orbit adjustments, will be ±0.5 km at the start of each limb scan (which can degrade to ±1 km at the end of the limb scan). The tangent heights are with respect to a geoid model of the Earth and the scan accounts for Earth's oblateness.

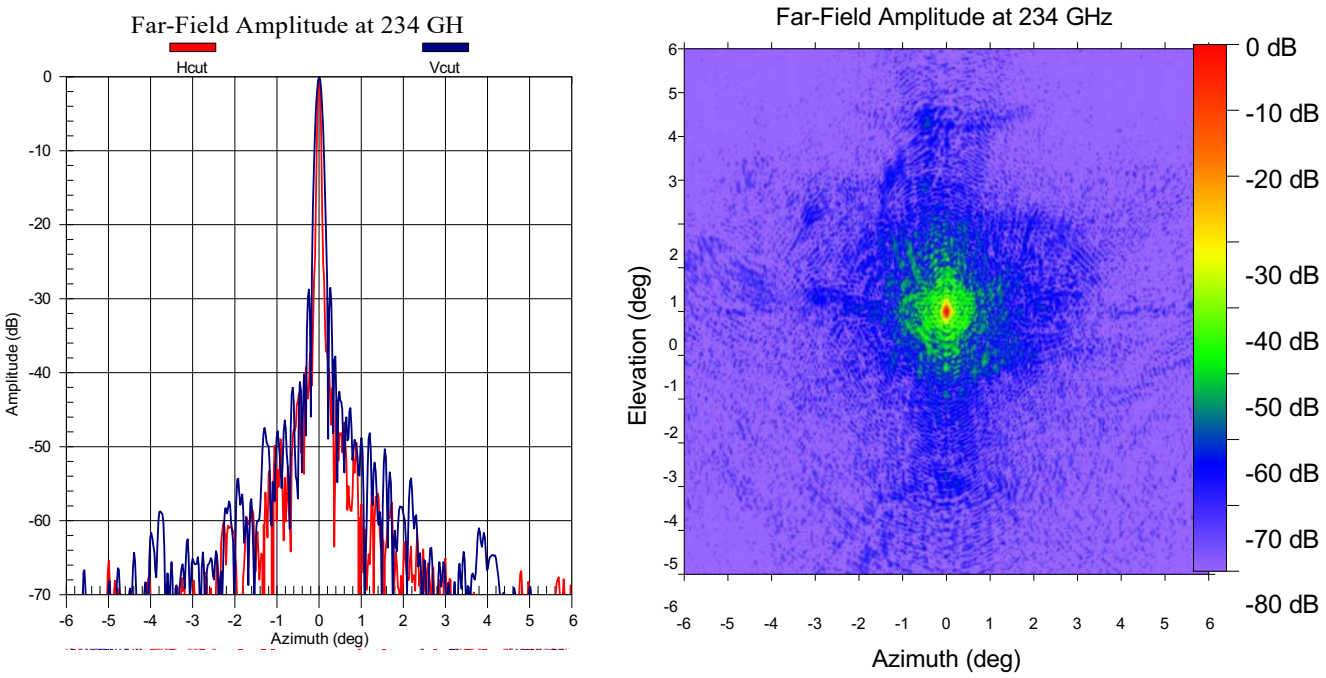

Figure 5-6. Measured EOS MLS field-of-view response at 234 GHz. The left panel shows measurements made along two orthogonal directions. The right panel shows a contour plot of the response over all angular directions within 6° of boresight. These measurements were made by Dr. Paul Stek, using a near-field range that was developed for this purpose.

To ensure that tangent height uncertainties due to boresight elevation uncertainties are comparable to, or less than, the equivalent height uncertainties in MLS measurements of tangent pressure, the change in elevation of the FOV boresights with respect to nadir during each limb scan will be known to an accuracy of 2 arcsecond (3σ), and the rate of change will be known to an accuracy of 1 arcsecond per second (3σ), at time scales between 0.17 and 25 seconds. (Note: 1 arcsecond corresponds to 15 m vertical distance at the limb tangent point.) MLS instrument data on the FOV boresight elevation is recorded twice per individual radiometric integration period, and spacecraft data relevant to the MLS FOV boresight elevation is recorded at least twice per individual radiometric integration period. Jitter in the FOV boresights at time scales shorter than 0.17 second will not exceed 2 arcsecond (3σ).

The absolute pointing knowledge required for EOS MLS geopotential height measurements will be obtained from the Aura satellite star tracker and Inertial Reference Unit (IRU) data. Drifts in these data will be 'calibrated out' by analyses of overlapping observations from successive orbits in the polar regions (see Figure 6-1, later in this document), and in the tropics where MLS temperature data indicate stable atmospheric conditions. Preliminary analyses indicate that pointing knowledge of 2 arcseconds (3σ) accuracy throughout the orbit can be maintained by this process. Biases in pointing will also be checked and corrected by occasional comparison of geopotential height retrieved from MLS with geopotential height fields from operational meteorological data. Comparisons will also be made with overlapping HIRDLS geopotential height retrievals to remove biases. HIRDLS can remove drifts in satellite pointing errors much more effectively than MLS because the HIRDLS azimuth scanning capability allows comparison *throughout the orbit* of measurements from adjacent orbits.

5.6. Overall instrument

The EOS MLS instrument has three major modules:

1. the 'GHz module', which contains the GHz antenna system, calibration targets, switching mirror, optical multiplexer and radiometers for the 118, 190, 240 and 640 GHz measurements,
2. the 'THz module', which contains the THz scan and switching mirror, calibration target, telescope and radiometers at both polarizations for the 2.5 THz measurements,
3. the 'Spectrometer Module', which contains the spectrometers, command and data handling, and power distribution systems.

Figure 5-7a is a line drawing of the instrument, with the three modules labeled. Figure 5-7b shows a photograph of the flight instrument, and Figure 5-7c shows a photograph of the instrument on the Aura spacecraft.

Table 5-5 gives the overall instrument mass, full-up power (average power over two orbits) and data rate. Section 5.8 gives a scenario for time-sharing measurements if needed to reduce power consumption.

Table 5-5. Mass, full-up average power, and data rate for the MLS instrument.

mass	453 kg
power	544 Watts
data rate	100 kilobits /second

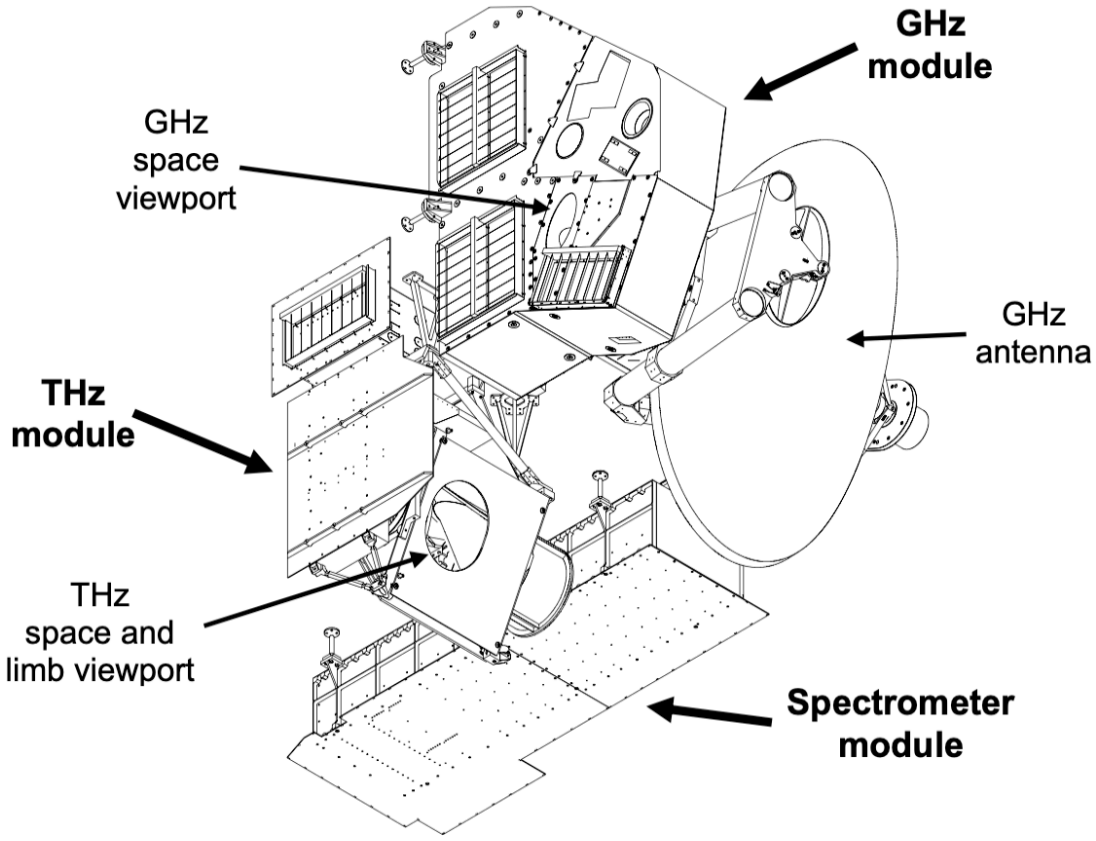

Figure 5-7a. Line drawing of the EOS MLS instrument.

Figure 5-7b. The EOS MLS flight instrument at JPL before delivery to the Aura spacecraft

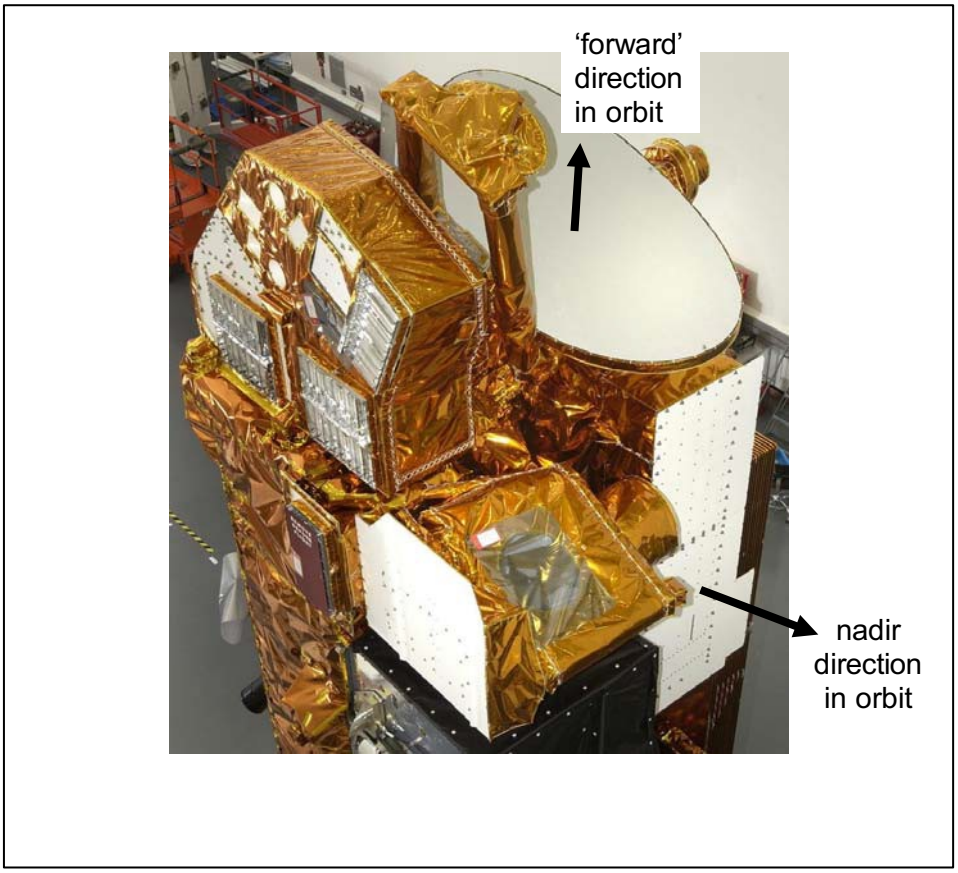

Figure 5-7c. The EOS MLS instrument on the Aura satellite just before delivery to the launch site. The satellite is in a 'vertical' orientation in this photograph.

5.7. Calibration

There are four categories of calibration for the EOS MLS instrument.

1. 'Radiometric calibration' gives the absolute power incident upon the antenna that is received in each spectral channel. As is typical in microwave radiometry, this power is calibrated in terms of a 'temperature' that is proportional to the power received, and converges - in the long-wavelength (Rayleigh-Jeans) limit - to the absolute temperature of a blackbody emitting that amount of power. The calibrated outputs are referred to as 'radiances'.
2. 'Field-of view (FOV) calibration' gives the response of the instrument to the input signal as a function of the angle at which the signal is incident upon the antenna.
3. 'Spectral calibration' gives the relative response of the instrument to the input signal as a function of the frequency of the signal.
4. 'Engineering calibration' gives the output of engineering sensors in appropriate units (e.g., volts, amperes).

Instrument calibration is performed in each of these categories. Examples of pre-launch calibration are: (1) measurement of the emissivities of the on-board targets and the loss in the antenna for radiometric calibration, (2) end-to-end measurement of the antenna response as a function of angle, or of the position of a probe in the antenna aperture near-field, for FOV calibration, (3) end-to-end measurement of the frequency response of each channel (including responses in radiometer sidebands) for spectral calibration, and (4) calibration of engineering sensors against accepted standards. In-orbit calibration includes: (1) observations of the on-board targets and 'cold space' between each limb scan for radiometric calibration, (2) occasional scans of the moon for FOV calibration, and (3) occasional frequency-sweeps with an on-board signal source for frequency calibration. Consistency of the measured spectral line shapes (as a function of tangent point pressure) with those calculated from a radiance 'forward model' also provides an in-orbit test of spectral and field-of-view calibration.

Radiometric calibration parameters are used primarily in MLS Level 1 data processing. Spectral and field-of-view calibration parameters are used primarily in Level 2 data processing. (See section 7 of this document, and references given there, for a description of MLS data processing.)

Approximate accuracies of the radiometric, spectral and field-of-view calibrations are as follows.

1. Radiometric. The systematic uncertainty in the atmospheric/Earth radiances measured through each spectral channel is less than (at the 90% confidence level):
   (a) 3K for the absolute value of the radiances, and
   (b) 1% or $\Delta I_{min}/3$ for the spectrally-varying component of the radiances measured from one channel or filter to another throughout a given radiometer (where ΔI_{min} for each spectral region is given in Table 5-2, and represents the smallest signal to be measured).
2. Spectral and field-of-view. The spectral and FOV responses are characterized sufficiently that their separate uncertainties do not introduce uncertainties in the MLS 'forward model' calculations of the atmospheric/Earth radiances of more than (at the 90% confidence level):
   (a) 3 K in the absolute value of radiances measured through each spectral channel, and
   (b) 1% or $\Delta I_{min}/3$ for the spectrally-varying component of the radiances measured from one channel or filter to another throughout a given radiometer (where ΔI_{min} for each spectral region is given in Table 5-2, and represents the smallest signal to be measured).

All MLS calibration is traceable to fundamental standards.

Methods for calibrating EOS MLS are similar to those used for UARS MLS [Jarnot et al. 1996]. The major difference was in field-of-view calibration where a compact range and near-field techniques were used for EOS MLS. The calibration report [Jarnot et al., 2004b] gives details and results of the EOS MLS calibration.

5.8 Measurement time sharing (if needed)

Although the MLS power requirements (544 Watts) for full-up operation are within the MLS power allocation (550 Watts) for the mission lifetime, a method for time sharing measurements has been devised for implementation in the unexpected case that less power becomes available. The instrument has flexibility to accommodate various time-sharing scenarios.

The following logic was used to select two radiometers whose operation could be time-shared to reduce the overall average power consumption. Approximately 1 day is needed for settling of switching thermal transients in order achieve stability required for all measurements, but some measurements will be possible in a much shorter time after switching.

1. The 118 GHz radiometer should not be time-shared because of the 'universal' need for its temperature and pressure measurements. (Note: we now expect to obtain better temperature and pressure from the 240 GHz radiometer; when this is demonstrated in orbit, we will change this time sharing requirement to the 240 GHz radiometer.)
2. The 190 GHz radiometer should not be time-shared because of the importance of its water vapor (both tropospheric and stratospheric) measurement.
3. This leaves the 240, 640 and 2.5 THz available for time-sharing.
4. The 640 GHz and 2.5 THz radiometers should be on together, at least some of the time, because HO_2, ClO, HCl and HOCl from 640 GHz are chemically related to (and should be measured simultaneously with) OH from 2.5 THz.
5. This leaves time-sharing of 240 GHz with either 640 GHz or 2.5 THz
6. It is better to have the 640 GHz on continuously than the 2.5 THz because (a) the 640 GHz provides a large number of measurements and has the best vertical resolution of any EOS MLS radiometer, and (b) every-other-month measurements of stratospheric OH are, at the current time, thought to be adequate.
7. This leaves time-sharing of the 240 GHz and 2.5 THz radiometers, and the two operational modes given in Table 5-6.

Table 5-6. Two operational modes for time-sharing to reduce MLS power consumption.

mode	operational status of radiometers	measurements lost in this mode
1	2.5 THz radiometer off, all other radiometers on	stratospheric OH
2	240 GHz radiometer off, all other radiometers on	upper tropospheric ozone, CO, best HNO_3 (note: stratospheric ozone is measured). [Note: after in orbit demonstration of T/P from the 240 GHz radiometer, this will change to '118 GHz radiometer off', with no measurements lost]

6. Measurement Coverage

The Aura orbit is sun-synchronous at 705 km altitude with 98° inclination and 1:45 p.m. ascending equator-crossing time. MLS performs observations with the instrument fields-of-view scanning the limb *in the orbit plane* to provide 82° N to 82° S latitude coverage on each orbit. MLS observes in the *forward* direction (direction of orbital motion), and the limb is scanned in an *upward* direction to give an observation path tangent point locus that is nearly vertical. The tangent points at greater heights are closer to the satellite, but in the Earth frame of reference this is compensated by the satellite's forward motion.

The MLS limb scans for nominal operation are synchronized to the orbit (using node-crossing ancillary data from the spacecraft), with the number of scans per orbit an integer multiple of 4, and phased such that limb scan locations occur over the equator. This gives the same latitude sampling in the northern and southern hemispheres, and on the ascending and descending portions of the orbit. MLS nominal operations have 240 limb scans per orbit to give 1.5° (~165 km, ~24.7 s) along-track separation between adjacent limb scans; this separation is well-matched to the along-track resolution expected for upper tropospheric water vapor measurements. Figure 6-1 shows the locations of measurements with this scan pattern for one 24-hour period.

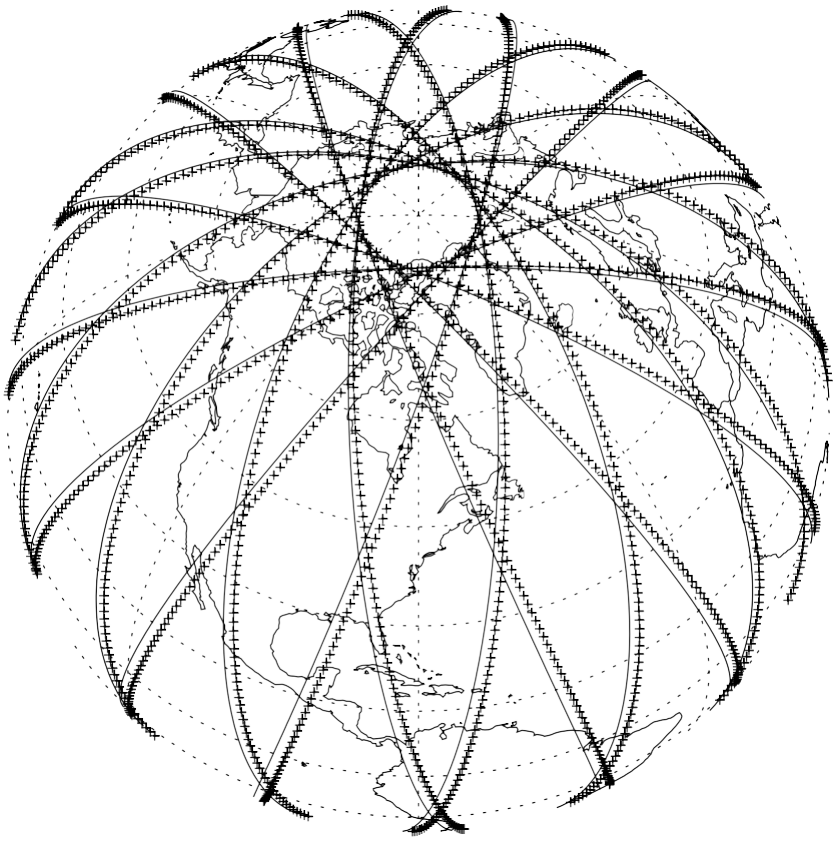

Figure 6-1. EOS MLS measurement locations for a 24 hour period. Each cross gives the location of the tangent points for individual limb scans. The continuous line is the suborbital track, which is slightly displaced from the tangent points because of Earth's rotation during the time in which the satellite moves forward to the tangent point latitude. The ascending portions of the orbit are those with the southeast-northwest tilt. Daily coverage at high latitudes in the Southern Hemisphere is analogous to that of the Northern Hemisphere shown here. R.R. Lay prepared this figure.

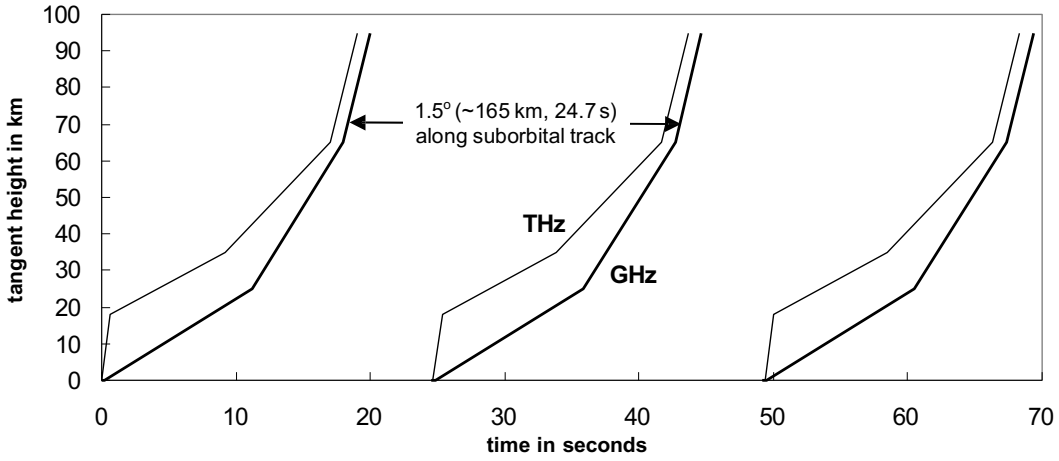

Figure 6-2. EOS MLS nominal operational scan. The curves give the height, at the tangent point, of the FOV boresight as a function of time. Radiometric calibration (observation of blackbody target and of cold space) and retrace are performed during the gap that appears between limb scans. The ~1 s difference between the end times of the THz and GHz scans is to reduce peak power transients when mirrors are moved more quickly during retrace.

The nominal operational limb scan profiles are shown in Figure 6-2, with details in Table 6-1. The scan is performed continuously (non-stepped), and the 1/6 s instrument integration time provides radiance measurements every 0.3-0.4 km in the vertical in the upper troposphere and lower stratosphere. The observation geometry in the orbit plane is shown in Figure 6-3.

Table 6-1. Details of the nominal GHz and THz scans.

GHz scan				**THz scan**			
tangent height range / km	MIF range	rate deg/s	rate km/MIF	tangent height range / km	MIF range	rate deg/s	rate km/MIF
0-25	1-67	0.0422	0.37	0-18	1-4	0.510	4.50
25-65	68-108	0.110	0.98	18-35	5-55	0.0375	0.33
				35-65	56-102	0.072	0.64
65-95	109-120	0.270	2.5	65-95	103-114	0.270	2.50
switching mirror to space view; antenna retrace	121-135	NA	NA	120-154 (23.3° space view)	115-128	NA	NA
switching mirror to target; antenna retrace	136-144	NA	NA	target view	129-138	NA	NA
return to 0 km limb view	145-147	NA	NA	return to 0 km limb view	139-147	NA	NA

Notes: (1) The MAF length is usually 148 MIFs (24.667 s), but occasionally is 149 MIFs (24.833 s) for synchronizing the MLS scan to the orbit. MIF numbering starts at 0; MIF 0 (as well as 149 when present) will dwell at 0 km tangent height.

(2) The THz mechanism spends MIFs 142-147 searching for zero encoder index while moving the FOV at ~1deg/s near (below) 0 km tangent height; this period may be useful for cloud studies.

(3) Mechanisms take 3 MIFs at the beginning of each step for motion; this means that the total calibration time is 18 MIFs, or 3 seconds.

(4) The GHz retrace takes exactly 4.5 s for displacements up to 2.1 degrees (111 km in tangent height); any retrace of larger size will take longer.

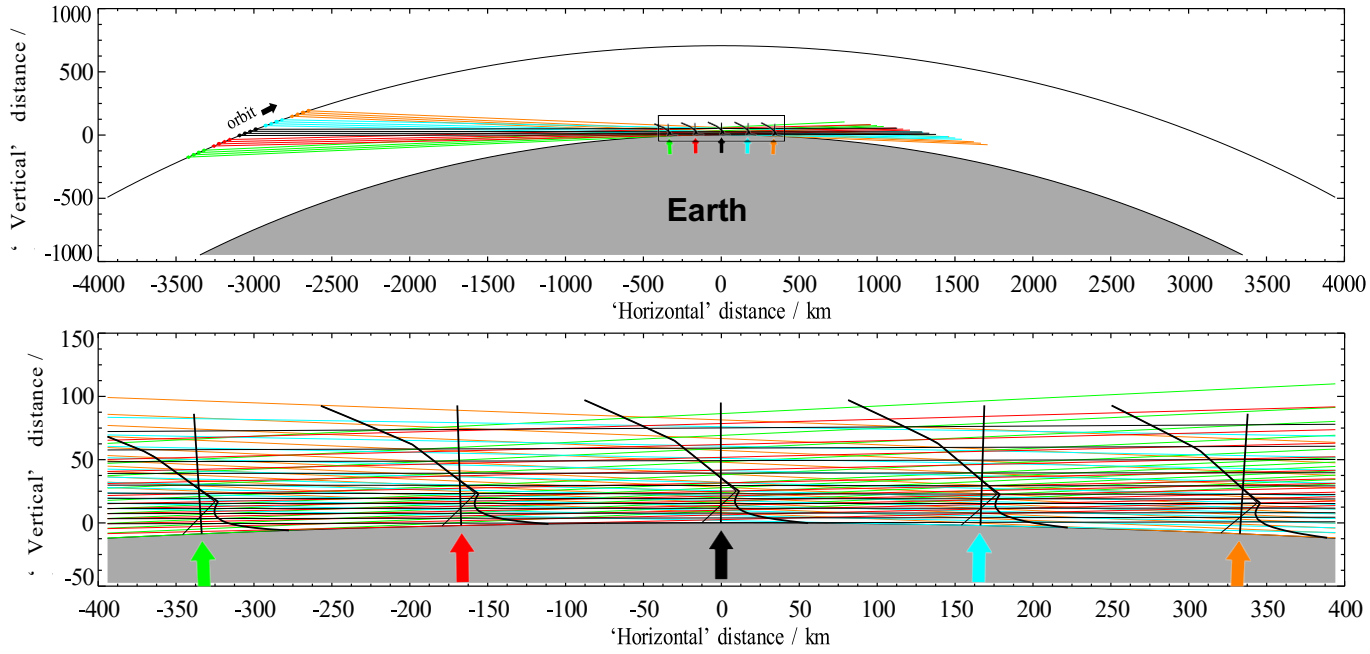

Figure 6-3. MLS observation geometry, as seen in the plane of one orbit. Line-of-sight paths are the colored lines going mostly horizontal across the figure; 12 of the 120 limb ray paths for 5 limb scans are shown. Earth’s surface is the gray shaded area. The vertical pointing arrows are the locations of retrieved profiles. The bent lines are the loci of the GHz FOV tangent point for the limb scans, with the two lines below ~20 km in the vertical showing the effect of refraction: the refracted (true) path is the thicker curve to the right. The THz tangent point is displaced forward of the GHz by ~50 km at ~20 km tangent height, decreasing to ~10 km at 90 km. From Livesey and Snyder [2004].

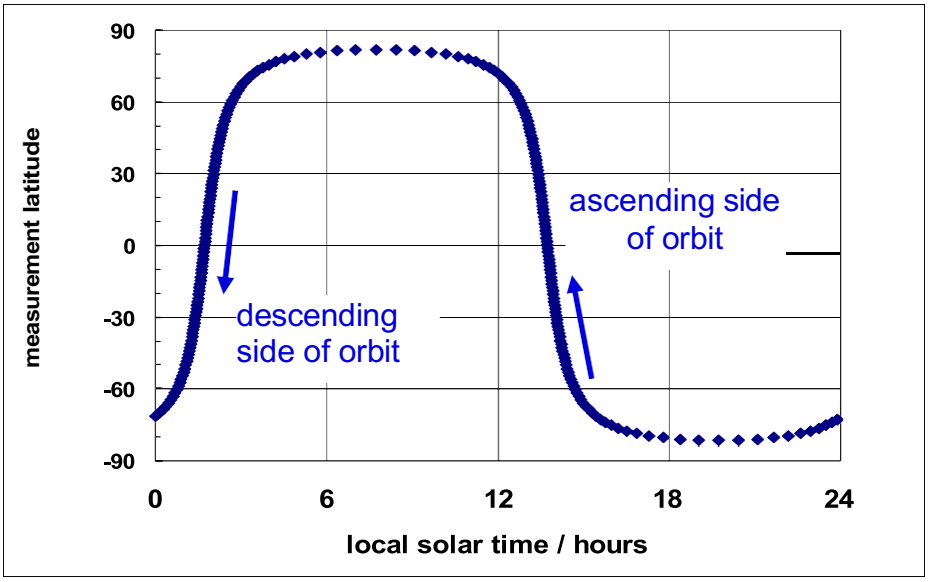

As the Aura orbit is sun-synchronous, MLS observations at a given latitude on either the ascending (north-going) or descending (south-going) portions of the orbit have approximately (to within several minutes) the same local solar time throughout the mission, as indicated in Figure 6-4. The boundaries between the day and night portions of the orbit vary through an annual cycle as shown in Figure 6-5.

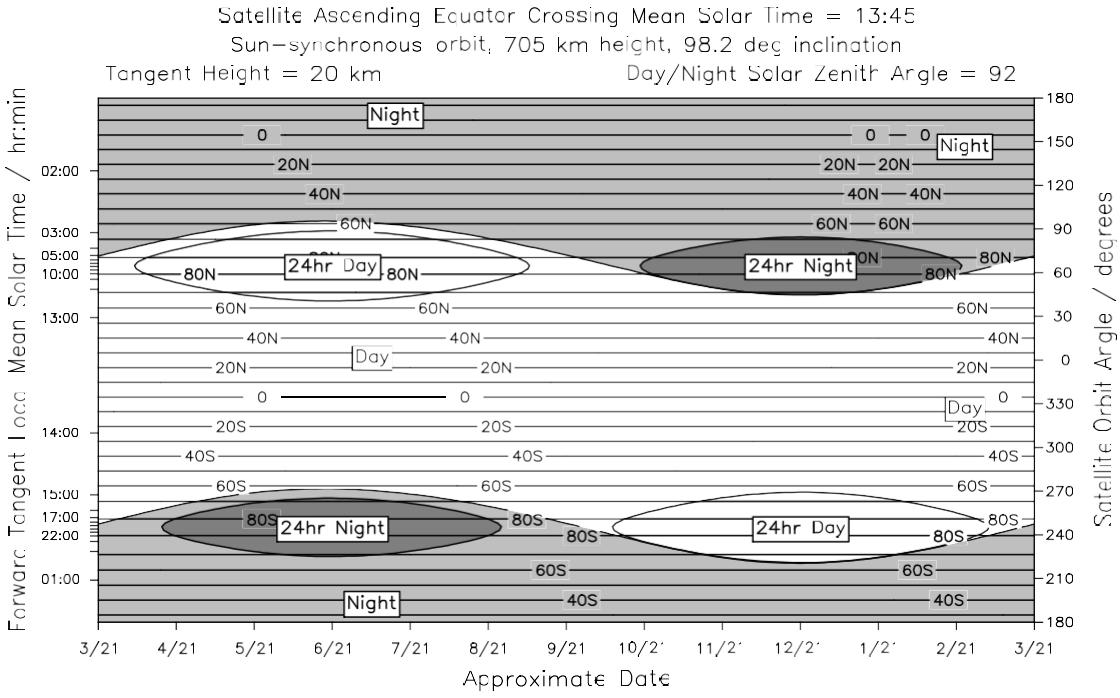

Figure 6-5. Variation, over an annual cycle, of the latitude range where MLS measurements are in day and in night. The horizontal axis gives the approximate date. The right hand vertical axis gives the orbit angle (defined as zero when the satellite is over the equator); the left hand vertical axis gives the corresponding local mean solar time at the (forward) tangent point of MLS observations. Horizontal lines give the latitude of the MLS tangent point, and the day-night boundary is defined as 92° local solar zenith angle.

7. Data Processing

7.1 EOS MLS data processing overview

Figure 7-1 shows the overall EOS MLS data processing flow.

Level 1 processing creates Level 1data files: calibrated MLS radiances and instrument engineering data. Inputs to this step are (a) the MLS Level 0 data, which are unprocessed instrument data, (b) the satellite ephemeris and engineering data, which are used, for example, to obtain satellite location and attitude, and (c) solar, lunar and planetary ephemerides, which are used to 'flag' situations when bright objects might be in the MLS fields-of-view.

Level 2 processing creates Level 2 data files of retrieved geophysical parameters. Inputs to this step are MLS Level 1 data and operational meteorological data (GMAO – GSFC Meteorological data Assimilation Office, and/or NCEP – National Center for Environmental Prediction).

Level 3 processing creates Level 3 files containing gridded daily and monthly maps, and daily and monthly zonal means. Inputs to this step are the MLS Level 2 data files. Zonal means of 'noisy products' such as BrO, HO_2, and lower stratospheric OH, will be produced using a Level 2 auxiliary file that provides information needed by Level 3 algorithms optimized for these products.

Summary descriptions of these processing steps are given separately in following subsections. The EOS MLS data products are described in section 8. Cuddy et al. [2004] give more details on the overall EOS MLS Data Processing system.

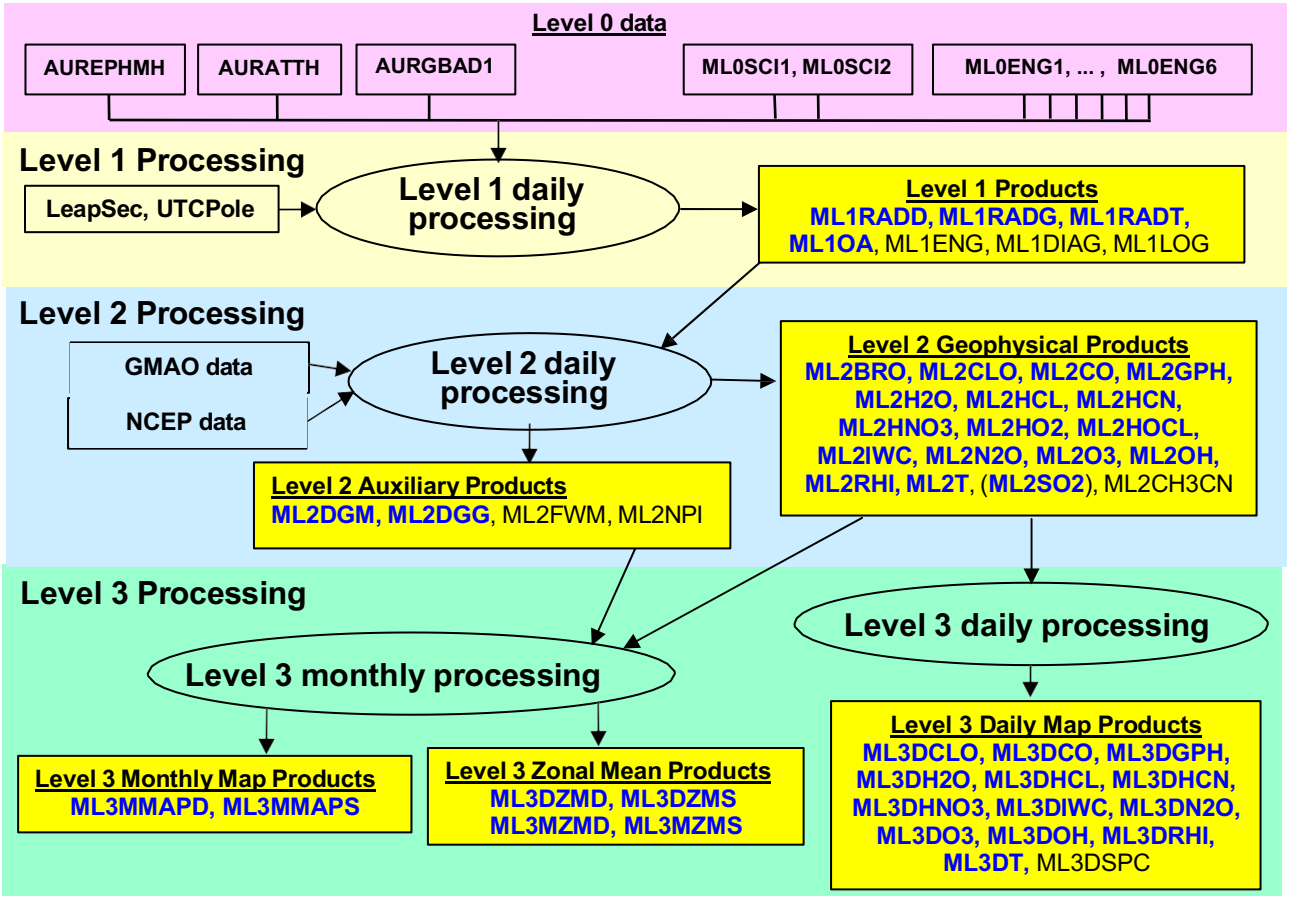

Figure 7-1. EOS MLS Data Processing Flow. Various data files are indicated in boxes. Yellow boxes are products from the MLS processing, where bold blue font indicates the Earth Science Data Type (ESDT) 'short name' for products delivered to the GES DAAC (ML2SO2, containing volcanic SO_2, is produced only after major volcanic eruption. This figure is based on a similar one prepared by D.T. Cuddy.

7.2 Level 1 data processing

The primary tasks of EOS MLS Level 1 data processing are to:

1. Qualify each datum using instrument configuration and checksum data, as well as transmission quality flags and statistical tests for 'reasonableness'.
2. Calibrate the instrument engineering data (e.g., voltages and temperatures).
3. Interpolate space and target radiometric measurements to the time of the limb measurements.
4. Calculate radiometric gain at the time of the limb measurements.
5. Determine the spectrally-varying component of the limb signal arising from antenna emission and scattering effects.
6. Estimate the spectrally-averaged component of the limb signal arising from antenna emission and scattering effects.
7. Calibrate the limb radiances and provide estimates of their uncertainties (for both the spectrally-varying and spectrally-averaged values).
8. Determine the field-of-view boresight pointing angles for each radiometer.
9. Generate ancillary data (e.g., tangent point location, local solar time and zenith angles; flags for 'bright objects' in the field-of-view) that are needed for quality checks in Level 2 processing.
10. Produce daily files of the data and a log summarizing instrument performance and outputs.

The theoretical basis and algorithms for this processing are given by Jarnot et al. [2004a], and have heritage from UARS MLS.

The calibrated limb radiances produced by EOS MLS Level 1 processing are the values, for each spectral channel and instrument integration period, of the radiance received within approximately 6° of the field-of-view boresight direction for that channel. (This is the angular range Ω_a over which the shape of the field-of-view is measured, an example of which has been shown previously in Figure 5-7, and used in Level 2 processing. The small amount of radiance received outside Ω_a is estimated and removed during Level 1 processing.) The radiance is calibrated as average radiant power per unit spectral interval received by that channel; this measure of the received power is expressed in units of temperature, which is convenient since the MLS signals originate thermally.

Briefly, the radiometric gain (counts per Kelvin) for channel α at the time of a limb (L) observation is estimated from target and 'cold space' counts (measured during the FOV 'retrace' following each limb scan) according to

$$g_\alpha(L) = \frac{C_\alpha^T(L) - C_\alpha^S(L)}{aP^T - bP^S - c}$$

where $C_\alpha^T(L)$ and $C_\alpha^S(L)$ are the target and 'cold space' count value interpolated onto the time of the limb measurement; P^T is the target radiance (determined from its monitored temperature and measured emissivity) and P^S is the 'cold space' radiance (that of a 2.7 K blackbody) for each channel. Small effects due to baffles in the GHz target and space views are accounted for by the near-unity factors a and b, and - due to differences in 'baffle emission' between the two views - by the small term c. The preceding equation is equivalent to that of equation (4.17) of Jarnot et al. [2004a] which contains expressions for a, b and c in terms of quantities produced during instrument calibration. For the THz (R5) radiometer, which views target and space through its *complete* optical system (not possible for the GHz bands because of the GHz antenna size), a and b are unity and c is zero.

The calibrated limb radiance power received by the antenna within angular range Ω_a for channel α is then produced according to

$$P_\alpha^A(L) = \beta \left[\frac{C_\alpha^L(L) - C_\alpha^S(L)}{g_\alpha(L)} + \gamma P^S - \delta \right]$$

where $C_\alpha^L(L)$ is the measured count for the limb observation L. Small multiplicative effects (due, e.g., to antenna loss and scattering) are accounted for by the near-unity terms β and γ, and small additive effects (due, e.g., to emission from the limb port baffle) are accounted for by the term δ. The preceding equation is equivalent to that of equations (4.14) and (4.18) of Jarnot et al. [2004a] which contains expressions for β, γ, and δ in terms of quantities produced during instrument calibration; δ is zero for the THz channels.

Calibration of limb radiances for the 'narrowband' digital autocorrelator spectrometer channels involves an additional Fourier transform step necessary to convert the measured autocorrelation function to spectral power density as described in Appendix H of Jarnot et al. [2004a].

7.3 Level 2 data processing

The primary tasks of EOS MLS Level 2 data processing software are to:

1. Retrieve geophysical parameters such as temperature, constituent abundances, from the EOS MLS Level 1B data, and provide estimates of uncertainties on the retrieved quantities.
2. Produce additional diagnostic information (such as radiances calculated from the retrieved parameters, and chi-square statistics) on the quality of the retrieved geophysical parameters, and 'flags' to detect bad retrievals.
3. Produce ancillary data, such as tropopause pressure, which may be derived from MLS data and/or ancillary meteorological data available at the time of data processing.
4. Produce daily files of the output data, and a log summarizing appropriate information on the processing statistics for that day.

Livesey and Snyder[2004] gives the theoretical basis and algorithms for the MLS Level 2 data processing, with extension to cloud products given by Wu and Jiang [2004]. The algorithms have heritage from UARS MLS.

Retrieval theory, the basis of algorithms used to obtain geophysical parameters from remote measurements, is a well-established field as described for atmospheric science by Rodgers [1976, 1990]. A 'state vector' **x** describes the atmospheric parameters being retrieved (as well as other quantities affecting the retrieval process), and a 'forward model' calculates estimates of the radiances (and other observables) from **x**. The process is initialized by an assumed value of **x**, and the retrieval algorithms, using the forward model, then adjust the elements of **x** to provide an optimal fit to the observed radiances. In addition to the radiance measurements, the retrieval algorithm uses 'virtual measurements' to improve the stability of the retrieval calculation, and the precision of the results. These virtual measurements are based on *a priori* knowledge of **x**, often taken from climatological data sources. This *a priori* knowledge is also typically used to construct the starting value of **x**.

The EOS MLS gas-phase forward model is described by Read et al. [2004], and its extension to polarized emission from mesospheric O_2 by Schwartz et al. [2004]. Briefly, the forward model $f_\alpha(\mathbf{x})$ for the limb radiance power P_α^A received by the antenna within angular range Ω_a for channel α during an individual integration period is given by the integral radiative transfer equation integrated over the instrument response and FOV movement during the integration period Δt:

$$\begin{aligned} P_\alpha^A &= \int_{\Delta t}\left[\int_{\Omega_a}\int_{\nu} A_\alpha[\nu,\Omega,\Omega_0(t)]\left\{I_\infty(\nu,\Omega)\,\tau(\nu,\infty)+\int_{s=\infty}^{s=0}\tau(\nu,s)\,\frac{dB\,]\nu,T(s)]}{ds}ds\right\}d\nu\,d\Omega\right]dt \\ &\equiv f_\alpha(\mathbf{x}) \end{aligned}$$

where ν is frequency of the radiation, Ω is angular direction with $\Omega_o(t)$ being the FOV boresight direction at time t and Ω_a the solid angle over which the FOV is measured during instrument calibration. $A_\alpha[\nu, \Omega, \Omega_o(t)]$ describes the instrument's spectral and FOV response for channel α, and $I_\infty(\nu, \Omega)$ is the 2.7 K cosmic background emission. Distance along the ray path is s (where the instrument is at $s = 0$), $T(s)$ is temperature and $B[\nu, T(s)]$ is the Planck blackbody function at s. The quantity $\tau(\nu, s)$ is the atmospheric transmission from s to the instrument given by

$$\tau(\nu,s)=\exp\left[-\int_{s'=s}^{s'=0}k\,]\nu,T(s'),f(s'),\rho(s')]\,ds'\right],$$

where k is the absorption coefficient as a function of frequency, temperature, mixing ratios f of atmospheric species affecting the radiance, and atmospheric density ρ. The forward model equation, as written above, neglects scattering and assumes thermal equilibrium and that ray paths do not intersect the surface of the Earth. Wu and Jiang [2004] describe the forward model used for the effects of clouds.

The task of the retrieval algorithms is to produce a best estimate of the state of the atmosphere represented by the vector **x**. Here the term 'best' means that state which minimizes the differences between the observed MLS radiances, represented by the vector **y,** and the results of a 'forward model' calculation **f**(**x**) describing the radiances that would be observed by MLS were the atmosphere in the state represented by **x**. These differences are summarized in the quantity χ^2, defined by

$$\chi^2 = [\mathbf{y}-\mathbf{f}(\mathbf{x})]^T\,\mathbf{S}_\mathbf{y}^{-1}\,[\mathbf{y}-\mathbf{f}(\mathbf{x})]$$

where $\mathbf{S}_\mathbf{y}$ is the error covariance matrix for the radiance vector **y**. In practice the minimum can often not be found without additional information. In the MLS case, as is typical, this information is supplied as *a priori* estimates on the state of the atmosphere, which we represent by the vector **a**, with error covariance $\mathbf{S}_\mathbf{a}$. The expression for χ^2 becomes

$$\chi^2 = [\mathbf{y}-\mathbf{f}(\mathbf{x})]^T\,\mathbf{S}_\mathbf{y}^{-1}\,[\mathbf{y}-\mathbf{f}(\mathbf{x})] + [\mathbf{a}-\mathbf{x}]^T\,\mathbf{S}_\mathbf{a}^{-1}\,[\mathbf{a}-\mathbf{x}]$$

The Gauss-Newton approach to the minimization of χ^2 gives the following iterative expression for finding the value of **x** that minimizes χ^2

$$\mathbf{x}_{p+1} = \mathbf{x}_p + \left[\mathbf{K}^T\mathbf{S}_\mathbf{y}^{-1}\mathbf{K} + \mathbf{S}_\mathbf{a}^{-1}\right]^{-1}\left[\mathbf{K}^T\mathbf{S}_\mathbf{y}^{-1}(\mathbf{y}-\mathbf{f}(\mathbf{x}_p)) + \mathbf{S}_\mathbf{a}^{-1}(\mathbf{a}-\mathbf{x}_p)\right]$$

where the *p* subscript indicates the iteration number, and the matrix **K** describes the *weighting functions*, defined by

$$\mathbf{K} = \frac{\partial \mathbf{f(x)}}{\partial \mathbf{x}}$$

The derivation of this expression, and the addition of constraints on the smoothness of the solution, and terms to aid convergence are given Livesey and Snyder [2004].

Livesey and Read [1999] and Livesey and Snyder [2004] describe extensions of the above expressions to direct retrieval of line-of-sight atmospheric structure as done by the EOS MLS algorithms.

The retrieval algorithms are implemented in phases as shown in Figure 7-2. The 'Core' phase, which itself consists of several initial phases, produces good estimates of temperature, geopotential height and tangent pressure. 'Core + Rn' phases then produce data products for which radiometer Rn gives information. Additional phases produce cloud data products, and high resolution data for certain selected products.

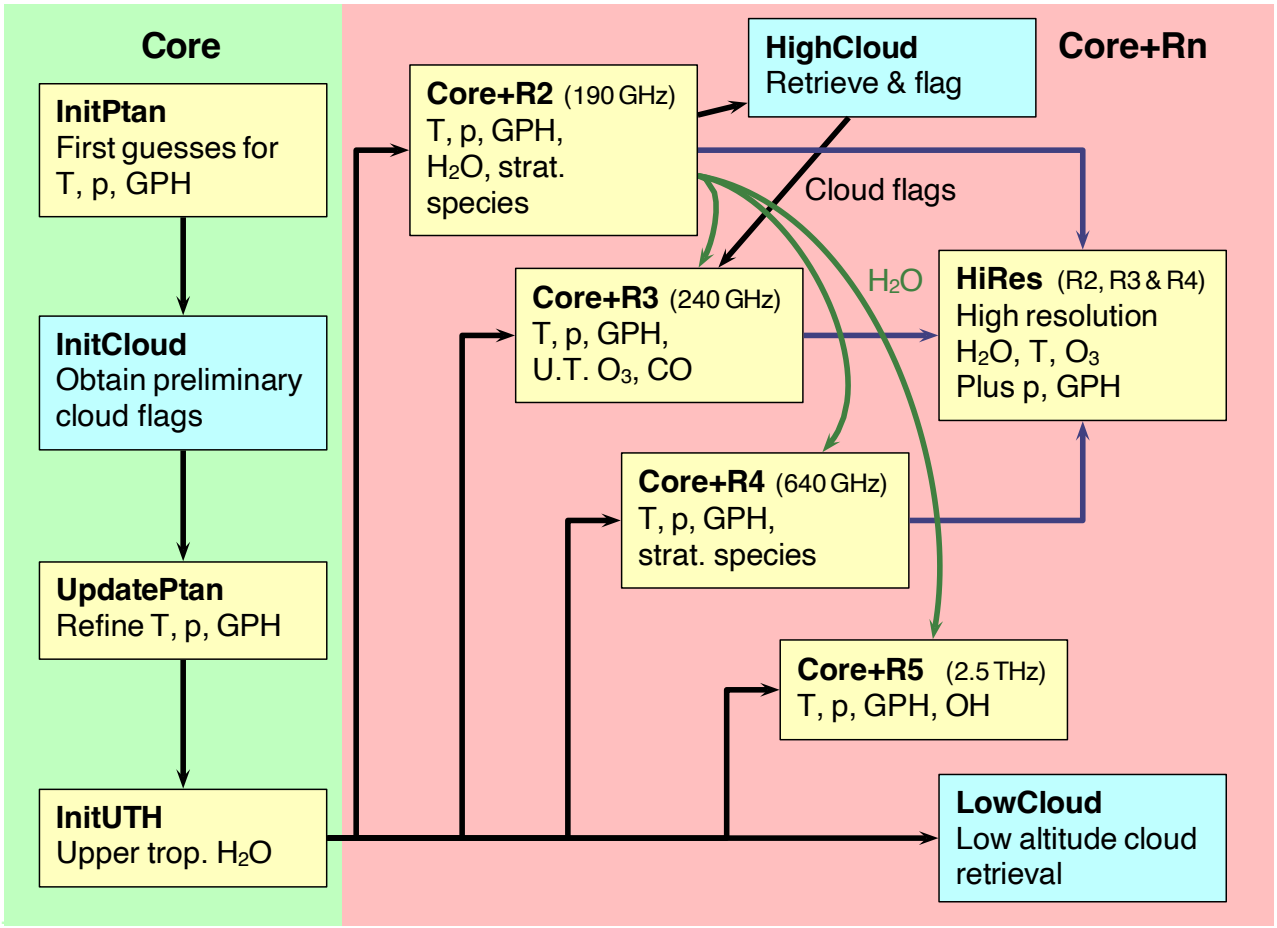

Figure 7-2. Phases implemented in the launch-ready MLS Level 2 software [from Livesey and Snyder, 2004].

7.4 Level 3 data processing

The tasks of EOS MLS Level 3 data processing are to produce:

1. daily gridded maps of measurements that have adequate signal-to-noise for making such maps,
2. daily and monthly zonal means,
3. monthly gridded maps.

Fourier 'asynoptic mapping' techniques, as initially developed by Salby [1982], are used for producing the daily gridded maps. Jiang [2004a] gives the theoretical basis for these techniques. They allow construction of a synoptic map (or quasi-synoptic map for species with a marked diurnal variation) from the MLS asynoptic measurements, and were applied to UARS MLS by Elson and Froidevaux [1993].

Optimum algorithms will eventually be used for producing daily and monthly zonal means of 'noisy products', as described by Livesey and Snyder [2004], but not yet implemented at time of writing. Zonal means of products with adequate signal-to-noise for the daily gridded maps can be taken from the 'wavenumber zero' Fourier component generated during production of the daily maps.

Monthly gridded maps can be generated from the daily gridded maps by averaging the daily gridded data over a monthly period. Monthly gridded maps for 'noisy products' will eventually be produced using special algorithms optimized for these products as described by Livesey and Snyder [2004], but not yet implemented at time of writing.

8. Data Products

8.1 Types of EOS MLS data products and examples of expected precisions

The following types of EOS MLS data products will be produced routinely.

Level 0 data

- 'Raw count' data from the instrument

Level 1 data

- Calibrated radiances with their estimated precisions for each MLS integration period and spectral channel, along with calibrated engineering data and ancillary data.

Level 2 data

- Geophysical products and their estimated precisions, along with ancillary data such as time, location, local solar time, etc.,
- Diagnostics, such as geophysical parameters measured in more than one spectral band, tangent point pressure, chi-square statistics, etc.

Level 3 data

- Daily gridded maps of all geophysical data products that have sufficient precision for making such maps, along with their estimated precisions,
- Daily and monthly zonal means of geophysical data products and their estimated precisions,
- Monthly global maps of geophysical data products and their estimated precisions.

All MLS Levels 1, 2 and 3 data are stored in HDF-5, or HDF-EOS5. Following subsections of this document give summary information on the products.

Table 8-1. The daily volume for EOS MLS routine data products. Values are in Megabytes.

	Level 1	**Level 2**	**Level 3**	**total**
delivered to DAAC	~4400	~1300	~100	~6000
total produced	~4500	~2500	~120	~7000

Table 8-2 gives examples and expected precisions of some MLS geophysical data products. The precisions are from Filipiak et al. [2004] and are based on the measured MLS flight instrument noise (given in Table 5-2) and the operational limb scan profiles (given in Figure 6-2). See Filipiak et al. [2004] for plots of precision and resolution versus height for all of the MLS geophysical data products.

Absolute accuracy of most products, based on experience from UARS MLS, is expected to be typically ~5% for composition measurements and ~1-2 K for temperature.

Table 8-2. Examples of estimated precision (1σ) and vertical resolution for MLS 'single profile' and 'monthly zonal mean' data products [Filipiak et al., 2004; Livesey et al., 2005; ice water content precision estimates by Dong Wu]. Values shown here are for the Version 1.5 software to be used for initial post-launch processing of MLS data. Note: (1) precision and vertical resolution are the same for geopotential height, and (2) SO_2 is produced only after major volcanic eruptions. Much work is needed with the real data to realize some of the predicted levels of precisions, especially for the monthly zonal mean products. Later versions of the software are expected to extend the lower height limit of some measurements, and produce some products with better vertical resolution.

.

Data product	**~ height range of usefulness / km**	**single profile precision (corresponding vertical resolution in parentheses) @ selected height range**	**monthly 5° zonal mean precision (corresponding vertical resolution) @ selected height range**
BrO	20 – 50	not expected to be useful	~8 pptv (~5 km) @ 20-40 km (longer/wider averages of BrO will be needed for useful precision)
CH_3CN	10–50	useful for > ~1 ppbv enhancement events	~5 pptv (~7 km) @ 50 km ~1 pptv (~5 km) @ 15-20 km
ClO	15–50	~0.4 ppbv (~4 km) @ 50 km 0.1-0.2 ppbv (3-4 km) @ 18-40 km	~15 pptv (4 km) @ 50 km ~10 pptv (3-4 km) @ 18-40 km
CO	10–90	~3 ppmv (~6 km) @ 80 km ~20 ppbv (4-5 km) @ 12–25 km	~0.1 ppmv @ 80 km ~1 ppbv @ 12-25 km
geopotential height	5–80	~50 m @ 80 km, ~30m @ 40 km ~20 m @ ~15 km, ~30m @ 10 km	not applicable
H_2O	8–80	~0.3 ppmv (~5 km) @ 50 km ~0.1 ppmv (~3 km) @ 20 km <10% (~ 3 km) @ 8 km to tropopause	~1% (3-5 km) @ 8-70 km
HCl	15–80	~0.4 ppbv (~5 km) @ 50 km ~0.1 ppbv (~3 km) @ 20 km	~5 pptv (~3-5 km) @ 15-50 km
HCN	10–50	~0.1 ppbv (~5 km) @ 20-40 km	~3 pptv (~5 km) @ 20-40 km
HNO_3	15–40	~2 ppbv (~4 km) @ 40 km ~1 ppbv (~3 km) @ 15-25 km	~40 pptv (~4 km) @ 40 km ~20 pptv (~3 km) @ 15-30 km
HOCl	15–40	not expected to be useful	20-40 pptv (~3 km) @ 20-40 km
HO_2	25–80	not expected to be useful	~70 pptv (~3 km) @ 50 km ~ 5 pptv (~5 km) @ 25 km
ice water content	10–20	~1 mg/m^3 (~2 km) @ 16 km ~2 mg/m^3 (~3 km) @ 14 km ~20 mg/m^3 (~3 km) @ 12 km	~0.1 mg/m^3 (~2 km) @ 16 km ~0.2 mg/m^3 (~3 km) @ 14 km ~1 mg/m^3 (~3 km) @ 12 km
N_2O	15–50	~20 ppbv (~5 km) @ 15-40 km	~1 ppbv (~5 km) @ 15-40 km
OH (upper stratosphere, mesosphere)	30–90	~30% (~5km) @ 75 km ~25% (~3km) @ 35-65 km	~1% (5km) @ 75 km ~1% (3 km) @ 30-60 km ~3% (~3 km) @ 30 km
OH (low strat.)	20-30	not expected to be useful	~ 1 pptv (3 km) @ 22-30 km *
O_3	10–90	~10% (3km) @ 50 km 2-5% (3km) @ 20-40 km 20-40 ppbv (3 km) @ 10-15 km	~ 1% (3km) @ 20-65 km ~1 ppbv (3km) @ 10-20 km
volcanic SO_2	15-40	~1 ppbv (4-6 km) @ 15-40 km	not applicable
temperature	8-90	~1 K (~10km) @ 80 km ~1K (~6 km) @ 50 km ~ 1 K (~4 km) @ 15-40 km	~0.0.3 K (~10 km) @ 80 km ~0.02 K (~6 km) @ 50 km ~ 0.01 K (~4 km) @ 15-40 km

8.2 Level 0 data products

Table 8-3 lists the Level 0 data products used in MLS production data processing.

Table 8-3. Level 0 data used in MLS processing.

description	ESDT	daily volume / Megabytes
MLS Level 0 science data	ML0SCI1, MLSC12	~1100
MLS Level 0 engineering data	ML0ENG - MLSENG6	~7
Aura satellite attitude data	AURATTH	~6
Aura satellite ephemeris data	AUREPHMH	~5
Aura satellite ground based attitude-determination data (contains 8 Hz Aura gyro data)	AURGBAD1	~20
	total	~1150

8.2 Level 1 data products

MLS Level 1 data products are calibrated instrument science and engineering data, performance diagnostics, and ancillary data such as georeferencing information. These are classified as Level 1B data in EOS terminology (p. 40 of MTPE EOS Reference Handbook 1995).

Table 8-4 lists the general contents and daily volume of MLS Level 1 data. There is one data file per day, each file corresponding to 00-24 hours Greenwich Mean Time (GMT). See Perun [2004] for a description of the contents of the MLS Level 1 data files.

Table 8-4. MLS Level 1B data products. Bold font indicates ESDT 'short names' for products that are delivered to the GES DAAC. The products not delivered to the DAAC are used by the MLS team for diagnostic and quality control purposes.

description	product	daily volume / Megabytes
Aura orbit/attitude and engineering data relevant for MLS 'footprints', etc.	**ML1OA**	~300
MLS radiances, GHz filter channels	**ML1RADG**	~1500
MLS radiances, GHz digital autocorrelator channels	**ML1RADD**	~2000
MLS radiances, THz channels	**ML1RADT**	~500
MLS Level 1 engineering data	ML1ENG	~100
MLS Level 1 diagnostics data	ML1DIAG	~25
MLS Level 1 log file	ML1LOG	<1
	total Level 1	~4500

8.3 Level 2 data products

There is one data file per day for each of the Level 2 data products. Each file corresponds to 00-24 hours GMT.

Level 2 geophysical parameters are produced on a 'standard' vertical grid having 6 points per decade change in pressure and on a horizontal grid having points every 1.5° great circle along the measurement track (near the nominal tangent point locations of each limb scan), as shown earlier in Figure 6-2. Some products that have adequate signal-to-noise and are useful with better vertical resolution at the expense of sensitivity, such as upper tropospheric water vapor, will also be produced, eventually, on a 'high-resolution' 12 points per decade pressure vertical grid.
Figure 8-1 shows vertical spacing between adjacent pressure surfaces for 3, 6 and 12 points per decade pressure, and the vertical extent of the EOS MLS fields-of-view (FOV). The vertical extent of the 63 GHz UARS MLS FOV is also shown for comparison. Good temperature profiles were obtained from the UARS MLS 63 GHz measurements at a resolution of 3 points per decade pressure (about half the field-of-view width), which demonstrated the capability to obtain vertical resolution better than that indicated solely by the MLS FOV width. Vertical smoothing is done by the retrieval algorithms as needed to give a stable product and an appropriate choice of the trade-off between precision and resolution. Filipiak et al. [2004], as well as showing the estimated precision for each Level 2 data product, also gives plots of 'averaging kernels' that describe both the vertical and horizontal resolution of the product.

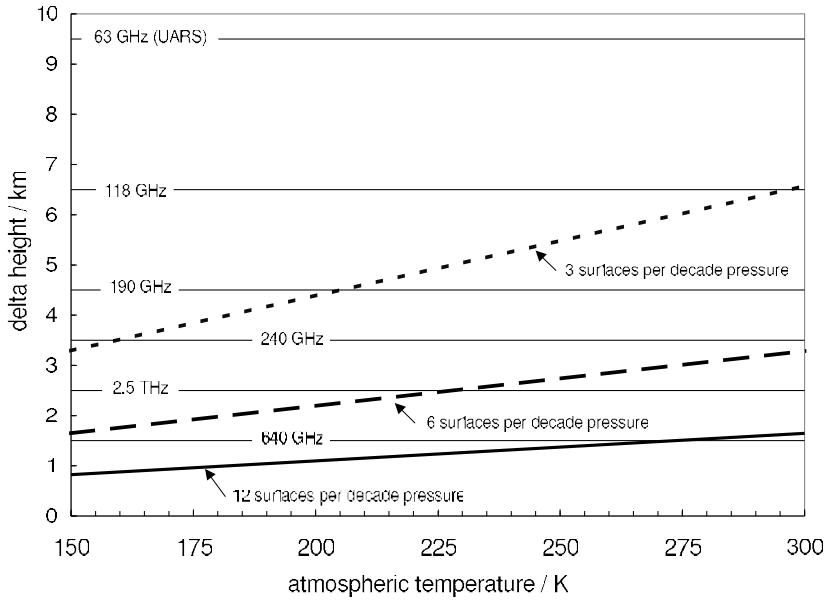

Figure 8-1. Vertical separation of atmospheric pressure surfaces (sloping lines) for different numbers of surfaces per decade pressure, and vertical extent of the fields-of-view (horizontal lines) at the limb tangent point for the various EOS MLS radiometers. The vertical extent of the field-of-view for the UARS MLS 63 GHz radiometer is also shown.

Table 8-5 shows ancillary data that are included with each MLS Level 2 retrieved profile. The 'data quality flag' is based on chi-square (χ^2) statistics indicating the quality of fit to the measured radiances and other diagnostics such as the number of radiances that were used in the retrieval of that profile. The 'data status flag' gives information on the 'status' of data for that profile, such as whether the profile might have been affected by clouds in the field of view or anomalies in the MLS operation that might have affected the profile.

Table 8-5. Ancillary data included with each MLS Level 2 vertical profile.

time, seconds from 1 January 1993 (in TAI units)
latitude, degrees N
longitude, degrees E
local solar time, hh:mm
local solar zenith angle, degrees
tangent point 'horizontal' line-of-sight angle *wrt* local north, degrees MLS geodetic angle (angle along orbit of retrieved profile)
data quality flag (identifies overall 'quality' of data for each profile)
data status flag (identifies overall 'status' of data for each profile)

Table 8-6 lists the EOS MLS Level 2 geophysical data files, and Tables 8-7 and 8-8 give information on 'auxiliary data files' created by Level 2 processing. See Wagner [2004] for a description of the contents of the Level 2 data files.

Table 8-6. EOS MLS Level 2 geophysical data files. Each file contains the value and estimated precision of each vertical profile point, the ancillary data in Table 8-5, and the column above the tropopause (as defined by the tropopause pressure included in the temperature file and inferred from the MLS temperature profile according to the WMO definition of 'tropopause'). 'High-resolution' data for H_2O and temperature are in the files for these products. Bold font in the 'product' column indicates ESTD 'short names' for products delivered to the DAAC; normal font in this column are filenames used on the MLS SCF. (The file for SO_2 is nominally produced only after a large volcanic eruption, when routing 'offline' retrievals detect the presence of measurable amounts of SO_2.)

measurement (alphabetical order)	product	initial vertical range of retrieval (not, necessarily, vertical range over which initial data will be useful)				daily volume / Megabytes
		pressure / hPa		~ height / km		
		max	min	min	max	
BrO	**ML2BRO**	147	0.001	13	95	~3
ClO	**ML2CLO**	147	0.001	13	95	~3
CO	**ML2CO**	316	0.001	8	95	~3
CH_3CN	ML2CH3CN	316	0.001	8	95	~3
geopotential height	**ML2GPH**	316	0.001	8	95	~3
H_2O	**ML2H2O**	316	0.001	8	95	~6
HCl	**ML2HCL**	147	0.001	13	95	~3
HCN	**ML2HCN**	100	0.001	15	95	~3
HNO_3	**ML2HNO3**	316	0.001	8	95	~3
HO_2	**ML2HO2**	147	0.001	13	95	~3
HOCl	**ML2HOCL**	147	0.001	13	95	~3
ice water content of clouds	**ML2IWC**	316	46	8	20	~3
N_2O	**ML2N2O**	215	0.001	11	95	~3
O_3	**ML2O3**	316	0.001	8	95	~3
OH	**ML2OH**	68	0.001	18	95	~3
relative humidity w.r.t. ice	**ML2RHI**	316	0.001	8	95	~3
SO_2	**(ML2SO2)**	215	0.1	11	65	~3
temperature	**ML2T**	316	0.001	8	95	~6
total Level 2 geophysical product daily volume						~60

Table 8-7. Level 2 Auxiliary Data Products. Bold font in the 'product' column indicates ESTD 'short names' for products delivered to the DAAC; normal font in this column are filenames used on the MLS SCF.

product	summary description	daily volume /Megabytes
ML2DGG L2GP-DGG	'geophysical diagnostic quantities': various diagnostics pertaining directly to the MLS geophysical data products, and generally on a grid similar (or idential) to that of the geophysical data products. See Table 8-7 for a summary description of the contents.	~300
ML2DGM L2AUX-DGM	'minor frame diagnostic quantities': various diagnostics that are on a minor frame grid. These include such items as tangent pressure, 'chi-square' describing various fits to the measured radiances, number of radiances used in various retrieval phases, etc.	~800
ML2DGM L2AUX-cloud	Values for 'cloud-induced radiances' inferred for selected spectral channels. These are differences from the estimated clear-sky radiances.	~100
ML2FWM	'Forward Model' calculated radiances, and related quantities	~2000
ML2NPI	'Noisy product information' needed by Level 3 algorithms optimized to produce averages of 'noisy' measurement. (At time of writing this feature has not yet been implemented.)	TBD

Table 8-8. MLS Level 2 'geophysical' diagnostic quantities. These are stored in the daily ML2DGG files, each daily file having a volume of ~300 Megabytes.

item	brief description
spectral baselines	retrieved values for various instrumental 'spectral baselines'
CH_3CN-190	CH3CN from the 'Core+R2' retrieval phase
CH_3CN-640	CH3CN from the 'Core+R4' retrieval phase
ClO-190	ClO from the 'Core+R2' retrieval phase
ClO-640	ClO from the 'Core+R4' retrieval phase
H_2O-190	H_2O from the 'Core+R2' retrieval phase
H_2O-Core	H_2O from the 'Core' retrieval phase
H_2O-InitUTH	H_2O from the 'Init UTH' portion of the 'Core' retrieval phase
HNO_3-190	HNO_3 from the 'Core+R2' retrieval phase
HNO_3-240	HNO_3 from the 'Core+R3' retrieval phase
HNO_3-640	HNO_3 from the 'Core+R4' retrieval phase
IWC-190	ice water content from the 'Core+R2' retrieval phase
IWC-240	ice water content from the 'Core+R3' retrieval phase
IWC-640	ice water content from the 'Core+R4' retrieval phase
LowCloudExtinction	retrieved values for extinction from low-altitude clouds
N_2O-190	N_2O from the 'Core+R2' retrieval phase
N_2O-640	N_2O from the 'Core+R4' retrieval phase
O_3-190	O_3 from the 'Core+R2' retrieval phase
O_3-240	O_3 from the 'Core+R3' retrieval phase
O_3-640	O_3 from the 'Core+R4' retrieval phase
O_3-UpdatePtan	O_3 from the 'UpdatePtan' portion of the 'Core' retrieval phase
refGPH-<various>	reference geopotential height from various phases of the retrievals
RHI-190	relative humidity from 'Core+R2' retrieval phase
RHI-Core	relative humidity from 'Core' retrieval phase
RHI-InitUTH	relative humidity from the 'InitUTH' portion of 'Core'
Temperature-<various>	temperature from various phases of the retrievals
tpPressure-wmo	tropopause pressure, based on WMO definition of tropopause
various numeric diagnostics	diagnostics on/from the 'numerical problem solvers' used by L2

8.4 Level 3 data products

Table 8-9 summarizes the MLS Level 3 data files. See Jiang [2004b] for details of their contents.

Table 8-9. Level 3 Products. Bold font in the 'product' column indicates ESTD 'short names' for products delivered to the DAAC; normal font in this column are filenames used on the MLS SCF.

product	summary description	time interval for each file	volume /Megabytes
ML3DMAP	Gridded daily maps. Each data product has a separate file; See table 8-9.	1 day	varies from 3.5 to 14, average = ~7
ML3DSPC	Wave spectra for each map. Contain amplitude and phase, for each latitude and pressure level, of the Fourier components that were fitted to the Level 2 data.	10 days (centered on ~30 days of measurements)	~500 total, average ~35 for each product
ML3MMAPS	Gridded monthly map 'standard' file; contains monthly maps for all MLS products	1 month	~40
ML3MMAPD	Monthly map 'diagnostic' file; contains monthly map diagnostics for all MLS products	1 month	~50
ML3DZMS	Daily zonal mean 'standard' file; contains daily zonal means for all MLS products	1 day	~3
ML3DZMD	Daily zonal mean 'diagnostic' file; contains daily zonal mean diagnostics for all MLS products	1 day	~5
ML3MZMS	Monthly zonal mean 'standard' file; contains monthly zonal means for all MLS products	1 month	~3
ML3MZMD	Monthly zonal mean 'diagnostic' file; contains monthly zonal mean diagnostics for all MLS products	1 month	~5

Daily gridded map products are made for MLS measurements which have adequate signal-to-noise. The output grid is 4° longitude by 2° latitude (between 82° N and 82° S). Table 8-10 gives the currently-planned daily map products. Separate maps for data from the ascending (mostly day) and descending (mostly night) portions of the orbit are made for the diurnally-varying species ClO, OH, and high-altitude O_3.

Table 8-10. Level 3 Daily Map Products. This table gives currently planned Level 3 Daily Map products, but this may change with experience in processing incoming data. (An MLS Level 3 product can be made from any MLS Level 2 product.) Bold font in the 'product' column indicates ESTD 'short names' for products delivered to the DAAC.

measurement	ESDT 'short name'	initial vertical range (not, necessarily, vertical range over which initial data will be useful)			
		pressure/ hPa		~ height / km	
		max	min	min	max
ClO	**ML3DCLO**	100	1	15	50
geopotential height	**ML3DGPH**	100	0.01	8	80
H_2O	**ML3DH2O**	100	0.01	8	80
HCl	**ML3DHCL**	100	0.1	15	65
HNO_3	**ML3DHNO3**	100	1	15	50
N_2O	**ML3DN2O**	100	1	10	50
O_3	**ML3DO3**	100	0.32	8	80
OH	**ML3DOH**	10	0.1	15	65
temperature	**ML3DT**	316	0.01	8	80

Level 3 monthly map products are produced for all MLS Level 2 products. These maps represent average conditions for the month and are currently planned to be produced at the 2^o latitude by 4^o longitude grid used for the Level 3 daily maps. Separate maps for the ascending and descending sides of the orbit will be produced for diurnally-varying species. The 'month' for these maps is defined to be the same as calendar months.

Daily zonal means are produced for all the MLS Level 2 data products. Separate zonal means are produced for the ascending and descending portions of the orbit, and the full latitudinal resolution of the corresponding Level 2 product is maintained (i.e., a zonal mean is produced for each of the Level 2 latitudes), which gives better latitude resolution at high latitudes. Ancillary data included with the geophysical parameters are latitude, local solar time and local solar zenith angle.

Level 3 monthly zonal means are also produced for all the MLS Level 2 products. Separate zonal means are produced for the ascending (mostly day) and descending (mostly night) portions of the orbit, and the full latitudinal resolution of the corresponding Level 2 product is maintained (i.e., a zonal mean is produced for each of the Level 2 latitudes). Ancillary data included with the geophysical parameters are latitude, and maximum and minimum values of the local solar time and local solar zenith angle for the measurement over the course of the month.

9. Data Validation

Validation of the EOS MLS data products will follow the same procedures used successfully for UARS MLS data, and documented in the UARS MLS data validation publications (see references cited in section 2 of this document). These include the following:

1. Simulation and sensitivity studies to determine the expected precision and absolute accuracy of each data product.
2. Inspection of all incoming data, and certain diagnostics, for 'reasonableness' and unexpected 'spikes' through examination of a manageable number of routine analyses products.
3. Examination of radiance residuals as a function of observation tangent pressure and signal frequency to determine, and hopefully eliminate, artifacts.
4. Comparison of the same geophysical parameter measured in more than one spectral region.
5. Comparison of MLS measurements with measurements of the same geophysical parameters by other instruments on the EOS Aura mission.
6. Comparison with other 'correlative measurements' from aircraft, balloon, and ground-based instruments.

A scientist on the MLS team who is knowledgeable in its scientific use is responsible for the validation of each geophysical data product. Tables 10-1 and 10-2, later in this document, give current responsibilities.

Table 9-1 gives correlative measurement priorities for EOS MLS. Development of a 'climatology' of cloud particle concentration and size distribution, especially for particles larger than ~100 μm would also improve interpretation of the MLS cloud ice water content data product.

More information on the overall Aura data validation activities, including details for MLS and the other instruments, is available in the Aura Science Data Validation Needs: Update [2004] (available at http://eos-aura.gsfc.nasa.gov).

Table 9-1. MLS Correlative Measurement Priorities. Measurements are listed in approximate order of decreasing priority within each category.

Priority	Geophysical Parameter	Comments
1	Upper tropospheric O_3, CO, H_2O, T	Aircraft measurements (preferably of vertical profiles) along the MLS track would be especially valuable, particularly in the tropics. Tropical data (e.g. sondes) would also be especially valuable (O_3, H_2O).
	Lower stratospheric O_3, H_2O, OH, BrO, HCl, N_2O, HNO_3 (and SO_2, if large volcano erupts into the stratosphere).	Aircraft measurements along the MLS track, vertical profiles if possible. Balloon/sonde measurements of vertical profiles.
	Upper tropospheric cloud data: number density and particle size distribution (for sizes of ~100 μm up to 1 mm), and total ice density.	Measurements for clouds above ~8 km in the tropics (along the MLS measurement track if possible).
2	Upper tropospheric HCN, CH_3CN	
	Lower stratospheric ClO, HOCl, T Lower stratospheric HO_2, CO	Polar winter data needed for chlorine species. Vertical profiles needed.
	Middle/upper strat. OH, HO_2, BrO, HCl, ClO, H_2O, O_3, HNO_3, N_2O, HOCl, CO, T	Vertical profiles needed.
3	Stratospheric HCN, CH_3CN, SO_2 (if no large volcanic eruption), geopotential height	Vertical profiles needed.

10. Personnel

Tables 10-1 through 10-4 list MLS personnel, and their primary responsibilities and/or scientific areas of interest.

Table 10-1. MLS personnel at the Jet Propulsion Laboratory. (Dr. Manney is currently on assignment at New Mexico Highlands University). * indicates formal MLS investigator recognized by NASA.

name	primary responsibility
Joe Waters *	MLS Principal Investigator
Lucien Froidevaux *	Deputy MLS PI (US) ; stratospheric O_3, HCl, HOCl products; data trends
Rick Cofield *	Optics design, field-of-view calibration, geopotential height
Robert Jarnot *	Instrument Scientist, GHz radiometric and spectral calibration
Nathaniel Livesey *	Retrieval theory/algorithms; N_2O, BrO, CH_3CN products
Gloria Manney *	Analyses of data for dynamical consistency, geopotential height
Herb Pickett *	2.5 THz system and calibration, OH and HO_2 products
Bill Read *	Standard 'forward model', upper tropospheric H_2O product
Michelle Santee *	HNO_3 and ClO products, polar process studies
Peter Siegel *	Radiometer technology (active during development phase of instrument)
Dong Wu *	Cloud ice products, atmospheric gravity wave studies
Dennis Flower	MLS Project Manager
Dave Cuddy	MLS Science Software and Data Processing Manager
Ryan Fuller	Data inspection operations software
Jonathan Jiang	Forward model for cloud effects, atmospheric gravity wave studies
Yibo Jiang	Level 3 map products and aspects of Level 2 analyses
Brian Knosp	Data inspection operations engineer
Richard Lay	Instrument operations, lead
Mario Loo	Instrument operations
Dominick Miller	Instrument operations
Nick Patel	MLS Science Computing Facility (SCF) Manager
Vince Perun	Level 1 data software engineer
Xuan Sabounchi	MLS science, software and operations group secretary
Michael Schwartz	Temperature and tangent pressure products
Van Snyder	Level 2 data software engineer
Paul Stek	Field-of-view calibration, Level 1 data inspection
Bob Thurstans	MLS SCF system software
Paul Wagner	Level 2 data software engineer

Table 10-2. MLS personnel at the University of Edinburgh.
* indicates formal MLS investigator recognized by NASA.

name	primary responsibility
Bob Harwood *	UK MLS Principal Investigator
Mark Filipiak *	CO and upper trop O_3 products, algorithm development
Hugh Pumphrey*	Stratospheric H_2O and HCN products, algorithm development
Cory Davis	Cloud forward model
Liang Feng	Data Assimilation
Carlos Jiminez	Retrieval theory
Archie MacDonald	University of Edingburgh MLS Science Computing Facility Manager
Ian MacKenzie	Atmospheric modeling

Table 10-3. Current members of the 'extended' MLS Science Team. It is anticipated, and encouraged, that this list will grow as MLS enters its operational phase and data become available.

name	organization	scientific area(s) of interest
Doug Allen	Naval Research Labs	stratospheric dynamics
Andy Dessler	U. of Maryland	water vapor, climate change, stratospheric chemistry
Rong Fu	Georgia Tech	upper tropospheric water vapor, climate change
Hope Michelsen	Lawrence Livermore	stratospheric chemistry and dynamics
Phil Mote	U. of Washington	water vapor, atmospheric dynamics transport
Darryn Waugh	Johns Hopkins U.	water vapor, climate change, atmospheric dynamics

Table 10-4. MLS Science Investigator-led Processing System (SIPS) personnel at Raytheon Information Technology and Science Services. Some of these personnel also support the EOS Aura Troposphere Emission Spectrometer (TES) SIPS operations.

name	primary responsibility
Emily Greene	SIPS Program Manager
Mark Echeverri	MLS SIPS System Engineer
Audrey Hanzel	MLS SIPS Operations Manager
Rafael Hernandez	SIPS Software Engineer
Barna Saha	SIPS Operator
David Romo	SIPS Operator
Paul Zimdars	SIPS System Adminstrator
John Burke	SIPS Database Adminsistrator

Acronyms (courier font indicates filenames)

AURATTH	Aura attitude data file
AUREPHMH	Aura ephemeris data file
AURGBAD1	Aura ground basee attitude data file
CTM	Chemical transport model
DAAC	Distributed Active Archive Center
DAC	Digital autocorrelator (MLS spectrometer for high-resolution spectra)
ESDT	Earth Science Data Type
EOS	Earth Observing System
FOV	Field-of-view
GES DAAC	GSFC Earth Science Distributed Active Archive Center
GMAO	GSFC Meteorological data Assimilation Office
GMT	Greenwich Mean Time
GPS	Global Positioning System
GSFC	Goddard Space Flight Center
GWs	Gravity Waves
HDF	Hierarchical Data Format
HDF-5	Hierarchical Data Format-5
HDF-EOS5	Hierarchical Data Format-Earth Observing System 5
HIRDLS	High Resolution Dynamics Limb Sounder
IF	Intermediate frequency
IPCC	Intergovernmental Panel on Climate Change
IRU	Inertial Reference Unit
JPL	Jet Propulsion Laboratory
LO	Local Oscillator
MAF	EOS MLS Major Frame
MAHRSI	Middle Atmosphere High Resolution Spectrograph Investigation
MIF	EOS MLS Minor Frame
ML0ENG1 – MLSENG6	EOS MLS Level 0 engineering data files
ML0SCI1, MLSC12	EOS MLS Level 0 science data files
ML1OA	EOS MLS Level 1 orbit attitude data files
ML1RADG	EOS MLS Level 1 radiance data file for GHz filter channels
ML1RADD	EOS MLS Level 1 radiance data file for GHz digital autocorrelators
ML1RADT	EOS MLS Level 1 radiance data file for THz filter channels
ML1ENG	EOS MLS Level 1 engineering data file
ML1DIAG	EOS MLS Level 1 diagnostics data file
ML1LOG	EOS MLS Level 1 log file
ML2BRO	EOS MLS Level 2 BrO data file
ML2CLO	EOS MLS Level 2 ClO data file
ML2CO	EOS MLS Level 2 CO data file
ML2CH3CN	EOS MLS Level 2 CH_3CN data file
ML2DGG(L2GP-DGG)	EOS MLS Level 2 geophysical diagnostic quantities data file
ML2DGM(L2AUX-DGM)	EOS MLS Level 2 minor frame diagnostic quantities data file
ML2DGM(L2AUX-cloud)	EOS MLS Level 2 cloud-induced radiances data file
ML2FWM	EOS MLS Level 2 Forward Model data file
ML2GPH	EOS MLS Level 2 geopotential height data file
ML2H2O	EOS MLS Level 2 H_2O data file
ML2HCL	EOS MLS Level 2 HCl data file
ML2HCN	EOS MLS Level 2 HCN data file

ML2HNO3	EOS MLS Level 2 HNO_3 data file
ML2HO2	EOS MLS Level 2 HO_2 data file
ML2HOCL	EOS MLS Level 2 HOCl data file
ML2IWC	EOS MLS Level 2 ice water content of clouds
ML2N2O	EOS MLS Level 2 N_2O data file
ML2NPI	EOS MLS Level 2 noisy product information data file
ML2O3	EOS MLS Level 2 O_3 data file
ML2OH	EOS MLS Level 2 OH
ML2RHI	EOS MLS MLS Level 2 relative humidity (with respect to ice) data file
ML2SO2	EOS MLS Level 2 SO_2 data file
ML2T	EOS MLS Level 2 temperature data file
ML3DCLO	EOS MLS Level 3 ClO daily map data file
ML3DGPH	EOS MLS Level 3 geopotential height daily map data file
ML3DH2O	EOS MLS Level 3 H_2O daily map data file
ML3DHCL	EOS MLS Level 3 HCl daily map data file
ML3DHNO3	EOS MLS Level 3 HNO_3 daily map data file
ML3DMAP	EOS MLS Level 3 daily map generic data file
ML3DN2O	EOS MLS Level 3 N_2O daily map data file
ML3DO3	EOS MLS Level 3 O_3 daily map data file
ML3DOH	EOS MLS Level 3 OH daily map data file
ML3DSPC	EOS MLS Level 3 wave spectra date file
ML3DT	EOS MLS Level 3 temperature daily map data file
ML3DZMD	EOS MLS Level 3 daily zonal mean diagnostic data file
ML3DZMS	EOS MLS Level 3 daily zonal mean standard data file
ML3MMAPD	EOS MLS Level 3 monthly map diagnostic data file
ML3MMAPS	EOS MLS Level 3 monthly map standard data file
ML3MZMD	EOS MLS Level 3 monthly zonal mean diagnostic data file
ML3MZMS	EOS MLS Level 3 monthly zonal mean standard data file
MLS	Microwave Limb Sounder
MMIC	Monolithic Millimeter-wavelength Integrated-Circuit
MODIS	Moderate Resolution Imaging Spectroradiometer
MTPE	Mission to Planet Earth
NASA	National Aeronautics and Space Administration
NCEP	National Center for Environmental Prediction
OMI	Ozone Monitoring Instrument
PT	Pressure/Temperature
PSC	Polar Stratospheric Clouds
QBO	Quasi-Biennial Oscillation
RITSS	Raytheon Information Technology and Scientific Services
SAGE	Stratospheric Aerosol and Gas Experiment
SIPS	Science Investigator-led Processing System
TES	Tropospheric Emission Spectrometer
TOMS	Total Ozone Mapping Spectrometer
TOR	Tropospheric Ozone Residual
TTL	Tropical Tropopause Layer
UARS	Upper Atmosphere Research Satellite
UT	Upper Troposphere
UT/LS	Upper Troposphere and Lower Stratosphere
UTH	Upper Tropospheric Humidity
WMO	World Meteorological Organization

References

Andreae, M.O., P. Artaxo, H. Fischer, S.R. Freitas, J.-M. Grégoire, A. Hansel, P. Hoor, R. Kormann, R. Krejci, L. Lange, J. Lelieveld, W. Lindinger, K. Longo, W. Peters, M. de Reus, B. Scheeren, M.A.F. Silva Dias, J. Ström, P.F.J. van Velthoven, J. Williams, "Transport of biomass burning smoke to the upper troposphere by deep convection in the equatorial region," *Geophys. Res. Lett. 28*, 951-954, 2001.

Appenzeller, C., A.K. Weiss, J. Staehelin, "North Atlantic oscillation modulates total ozone winter trends," *Geophys. Res. Lett. 27*, 1131-1134, 2000.

Aura Science Data Validation Plan, Version 1.0 (available at http://eos-aura.gsfc.nasa.gov), 2001.

Aura Science Data Validation Needs: Update, Version 1.0, available at http://eos-aura.gsfc.nasa.gov, 2004.

Barath, F.T., et al., "The Upper Atmosphere Research Satellite Microwave Limb Sounder Instrument," *J. Geophys. Res. 98*, 10,751, 1993.

Borrman, S., S. Solomon, J.E. Dye, and B. Luo, "The potential of cirrus clouds for heterogeneous chlorine activation," *Geophys. Res. Lett. 23*, 1996.

Burrows, J.P., et al., "The Global Ozone Monitoring Experiment (GOME): Mission Concept and First Scientific Results," *J. Atmos. Sci. 56*, 151, 1999.

Conway, R.R., M.E. Summers, M.H. Stevens, "Satellite Observations of Upper Stratospheric and Mesospheric OH: The HO_x Dilemma," *Geophys. Res. Lett. 27*, 2613-2616, 2000.

Craig, C., K. Stone, D. Cuddy, S. Lewicki, P. Veefking, P. Leonard, P. Wagner, "HDF-EOS Aura File Format Guidelines," Version 1.3, 2003.

Cunnold, D., H.Wang, W.P. Chu, and L. Froidevaux, "Comparisons between Stratospheric Aerosol and Gas Experiment II and microwave limb sounder ozone measurements and aliasing of SAGE II ozone trends in the lower stratosphere," *J. Geophys. Res. 101*, 10,061, 1996a.

Cunnold, D., L. Froidevaux, J.M. Russell, B. Connor, and A. Roche, : Jet Propulsion Laboratory Document D-16159**,** Version 2.0, 2004. "Overview of UARS ozone validation based primarily on intercomparisons among UARS and Stratospheric Aerosol and Gas Experiment II measurements," *J. Geophys. Res. 101*, 10335, 1996b.

Cuddy, D.T., et al., "The EOS MLS Data Processing System," manuscript in preparation for *IEEE Transactions on Geoscience and Remote Sensing* special issue on the EOS Aura mission.

Dessler, A.E., H. Kim, "Determination of the amount of water vapor entering the stratosphere based on HALOE data," *J. Geophys. Res. 104*, 30,605-30,607, 1999.

DeLucia, F.D., A. Meshkov,' paper presented at International Workshop on Critical Evaluation of millimeter and sub-millimeter wave Spectroscopic Data for Atmospheric Obserevations, Mito, Japan, 29-30 January 2004.

Drouin, B.J., "Temperature Dependent Pressure Induced Lineshape of the HCl J=1←0 Rotational Transition in Nitrogen and Oxygen," *J. Quant. Spec. Rad. Trans. 83*, Issues 3-4, 321-331, 2004.

Drouin, B.J., J. Fisher, R.R. Gamache, "Temperature dependent pressure induced lineshape of O_3 rotational transitions in air," *J. Quant. Spec. Rad. Trans. 83*, Issue 1, 63-81, 2004.

Dvortsov, V.L., S. Solomon, "Response of the stratospheric temperatures and ozone to past and future increases in stratospheric humidity," *J. Geophys. Res. 106*, 7505-7514, 2001.

Elson, L.S., and L. Froidevaux, "The use of Fourier transforms for asynoptic mapping: Early results from the Upper Atmosphere Research Satellite Microwave Limb Sounder," *J. Geophys. Res. 98*, 23039, 1993.

Fahey, D.W., et al., "The detection of large HNO_3-containing particles in the winter Arctic stratosphere," *Science 291*, 1026-1031, 2001.

Filipiak, M.J., N.J. Livesey, W.G. Read, "EOS MLS Retrieved Geophysical Parameter Precision Estimates," Edinburgh University Meteorology Department Technical Report (also Jet Propulsion Laboratory Document D-16160)**,** Version 1.5, 2005.

Fishbein, E.F., R.E. Cofield, L. Froidevaux, R.F. Jarnot, T.A. Lungu, W.G. Read, Z. Shippony, J.W. Waters, I.S. McDermid, T.J. McGee, U. Singh, M. Gross, A. Hauchecorne, P. Keckhut, M.E. Gelman, and R.M. Nagatani, "Validation of UARS Microwave Limb Sounder temperature and pressure measurements," *J. Geophys. Res. 101*, 9938, 1996.

Fishman, J., C.E. Watson, J.C. Larsen, J.A. Logan, "Distribution of tropospheric ozone determined from satellite data," *J. Geophys. Res. 95*, 3599-3617, 1990.

Forster, P.M. de F., K.P. Shine, "Radiative forcing and temperature trends from stratospheric ozone changes," *J. Geophys. Res. 102*, 10841-10857, 1997

Forster, P.M. de F., and K.P. Shine 2002, "Assessing the climate impact of trends in stratospheric water vapor," *Geophys. Res. Lett. 29*, No. 6, 10.1029/2001GL013909, 2002.

Froidevaux, L., W.G. Read, T.A. Lungu, R.E. Cofield, E.F. Fishbein, D.A. Flower, R.F. Jarnot, B.P. Ridenoure, Z. Shippony, J.W. Waters, J.J. Margitan, I.S. McDermid, R.A. Stachnik, G.E. Peckham, G. Braathen, T. Deshler, J. Fishman, D.J. Hofmann, and S.J. Oltmans, "Validation of UARS Microwave Limb Sounder ozone measurements," *J. Geophys. Res. 101*, 10,017, 1996.

Froidevaux, L., J.W. Waters, W.G. Read, P.S. Connell, D.E. Kinnison, J.M. Russell III, "Variations in the free chlorine content of the stratosphere (1991-1997): Anthropogenic, volcanic, and methane influences," *J. Geophys. Res. 105*, 4471-4481, 2000.

Harris, N.R.P., M. Rex, P. von der Goutail, G.L. Manney, R. Müller, "Comparison of empirically derived ozone loss rates in the Arctic vortex," *J. Geophys. Res. 107*, 10.1029/2001JD001011, 2002.

Hofmann, D.J., "Recovery of antarctic ozone hole," *Nature 384*, 222-223, 1996.

Holton, J.R., A. Gettelman, "Horizontal transport and the dehydration of the stratosphere," *Geophys. Res. Lett. 28*, 2799-2802, 2001.

Holton, J.R., P.H. Haynes, M.E. McIntyre, A.R. Douglass, R.B. Rood, L. Pfister, "Stratospheric-Tropospheric Exchange," *Rev. Geophys. 33*, 403-439, 1995.

Hood, L.L., B.E. Soukharev, M. Fromm, J.P. McCormack, "Origin of extreme ozone minima at middle to high northern latitudes," *J. Geophys. Res. 106*, 20,925-20,940, 2001.

IPCC, *Climate Change 2001: The Scientific Basis*, J.T. Houghton, Y. Ding, D.J. Griggs, M. Noguer, P.J. van der Linden, X. Dai, K. Maskell, C.A. Johnson, eds., Intergovernmental Panel on Climate Change, Cambridge University Press, Cambridge, UK, 2001.

Jarnot, R.F., R.E. Cofield, J.W. Waters, G.E. Peckham, and D.A. Flower, "Calibration of the Microwave Limb Sounder on the Upper Atmosphere Research Satellite," *J. Geophys. Res. 101*, 9957, 1996.

Jarnot, R.F., H.M. Pickett, M.J. Schwartz, "EOS MLS Level 1 Data Processing Algorithm Theoretical Basis," Jet Propulsion Laboratory Document D-15210**,** Version 2.0, 2004a.

Jarnot, R.F., R.E. Cofield, H.M. Pickett, P.C. Stek, "EOS MLS Calibration Report: Volume I," Jet Propulsion Laboratory Document D-26280, 2004b.

Jiang, Y., "EOS MLS Level 3 Algorithms Theoretical Basis," Jet Propulsion Laboratory Document D-18911, Version 1.0, 2004a.

Jiang, Y., "EOS MLS Level 3 File Description and Data Dictionary," Version 1.43, 2004b. (available from the MLS Science Team)

Lahoz, W.A., M.R. Suttie, L. Froidevaux, R.S. Harwood, C.L. Lau, T.A. Lungu, G.E. Peckham, H.C. Pumphrey, W.G. Read, Z. Shippony, R.A. Suttie, J.W. Waters, G.E. Nedoluha, S.J. Oltmans, J. Russell III, and W.A. Traub, "Validation of UARS Microwave Limb Sounder 183 GHz H_2O measurements," *J. Geophys. Res. 101*, 10,129, 1996.

Law, K.S., P.H. Plantevin, V. Thouret, A. Marenco, W.A.H. Asman, M. Lawrence, P.J. Crutzen, J.-F. Müller, D.A. Hauglustaine, M. Kanakidou, "Comparison between global chemistry transport model results and Measurement of Ozone and Water Vapor by Airbus In-Service Aircraft (MOZAIC) data," *J. Geophys. Res. 105*, 1503-1525, 2000.

Lelieveld, J., F.J. Dentener, "What controls tropospheric ozone?," *J. Geophys. Res. 105*, 3531-3551, 2000.

Lindzen, R.S., "Some coolness concerning global warming," *Bull. Am. Meteorol. Soc. 71*, 288-299, 1990.

Livesey, N.J., and W.G. Read, "Direct Retrieval of Line-of-Sight Atmospheric Structure from Limb Sounding Observations," *Geophys. Res. Lett. 27*, 891-894, 2000.

Livesey, N.J., J.W. Waters, R. Khosravi, G.P. Brasseur, G.S. Tyncall, W.G. Read, "Stratospheric CH_3CN from the UARS Microwave Limb Sounder," *Geophys. Res. Lett. 28*, 779-782, 2001.

Livesey, N.J., W.G. Read, L. Froidevaux, J.W. Waters, H.C. Pumphrey, D.L. Wu, M.L. Santee, Z. Shippony, R.F. Jarnot, "The UARS Microwave Limb Sounder version 5 dataset: Theory, characterization and validation," *J. Geophys. Res. 108*, (D13) 4378, doi: 10.1029/2002JD002634, 2003.

Livesey, N.J., and W.V. Snyder, "EOS MLS Retrieval Processes Algorithm Theoretical Basis," Jet Propulsion Laboratory Document D-16159**,** Version 2.0, 2004.

Livesey, N.J., M.D. Fromm, J.W. Waters, G.L. Manney, M.L. Santee, W.G. Read, "Enhancements in lower stratospheric CH_3CN observed by UARS MLS following boreal forest fires," *J. Geophys. Res. 109*, (D06308) 4378, doi: 10.1029/2003JD004055, 2004a.

Livesey, N.J., et al., "Version 1.5 Level 2 data processing algorithms: Implementation and results," document available from the MLS Science Team, 2005.

Mackenzie, I., R.S. Harwood, L. Froidevaux, W.G. Read, and J.W. Waters, "Chemical loss of polar vortex ozone inferred from UARS MLS measurements of ClO during the Arctic and Antarctic springs of 1993", *J. Geophys. Res. 101*, 14505-14518, 1996.

Manney, G.L., L. Froidevaux, J.W. Waters, R.W. Zurek, W.G. Read, L.S. Elson, J.B. Kumer, J.L. Mergenthaler, A.E. Roche, G.E. Peckham, and R. Swinbank, "Chemical depletion of ozone in the Arctic lower stratosphere during winter 1992-93," *Nature 370*, 429-434, 1994.

Matsueda, H., H.Y. Inoue, M. Ishii, Y. Tsutsumi, "Large injection of carbon monoxide into the upper troposphere due to intense tropical biomass burning in 1997," *J. Geophys. Res. 104*, 26,867-26,879, 1999.

McPeters, R.D., S.M. Hollandsworth, L.E. Flynn, J.R. Herman, and C.J. Seftor, "Long-term ozone trends derived from the 16-year combined Nimbus 7/Meteor 3 TOMS Version 7 record," *Geophys. Res. Lett. 23*, 3699, 1996.

Montzka, S.A., J.H. Butler, B.D. Hall, D.J. Mondeel, J.W. Elkins, "A decline in tropospheric organic bromine," *Geophys. Res. Lett. 30*, No. 15, 1826, doi: 10.1029/2003GL017745, 2003.

MTPE EOS Reference Handbook 1995, available from the EOS Project Science Office, code 900, NASA Goddard Space Flight Center, Greenbelt, MD 20771, 1995.

NASA Goddard Space Flight Center, "EOS Execution Phase Project Plan," GSFC document 170-01-01, May 1995.

NASA Goddard Space Flight Center, "EOS Chemistry Project Plan," GSFC Document 424-PG-7120.2.1, 15 April 1999.

NASA Reference Publication 1399, "Present State of Knowledge of the Upper Atmosphere 1996: An Assessment Report," 1997.

NASA Earth Science Enterprise, Strategic Plan, "Exploring Our Home Planet," NASA Headquarters, Washington DC, www.earth.nasa.gov, 2000.

Oh, J.J., and E.A. Cohen, "Pressure broadening of ClO by N_2 and O_2 near 204 and 649 GHz and new frequency measurements between 632 and 725 GHz," *J. Quant. Spectrosc. Radiat. Transfer 54*, 151-156, 1994.

Perun, V.S., "EOS MLS Level 1 File Description and Data Dictionary," Version 1.43, 2004. (available from the MLS Science Team)

Pickering, K.E., A.M. Thompson, Y. Wang, W. Tao, D.P. McNamara, V. W. J. H. Kirchhoff, B.G. Heikes, G.W. Sachse, J.D. Bradshaw, G.L. Gregory, and D.R. Blake, "Convective transport of biomass burning emissions over Brazil during TRACE A," *J. Geophys. Res. 101*, 23,993, 1996.

Pickett, H.M., R.L. Poynter, and E.A. Cohen, "Submillimeter, Millimeter, and Microwave Spectral Line Catalog," *Tech. Rep. 80-23*, Jet Propulsion Laboratory, Pasadena, California, 1992.

Pickett, H.M., "THz spectroscopy of the atmosphere," *SPIE 3617*, 2-6, 1999.

Pierrehumbert, R.T., "Thermostats, radiator fins, and local runaway greenhouse," *J. Atmos. Sci. 52*, 1754-1806, 1995.

Pierrehumbert, R., "Subtropical water vapor as a mediator of rapid global climate change," in *Mechanisms of global change at millennial time scales*, (P.U. Clark, R.S. Webb, L.D. Keigwin, eds.), Geophysical American Geophysical Union Monograph Series, 2000.

Plumb, R.A., W. Heres, J.L. Neu, N.M. Mahowald, J. del Corral, G.C. Toon, E. Ray, F. Moore, A.E. Andrews, "Global tracer modeling during SOLVE: High latitude descent and mixing," *J. Geophys. Res.*, 83090, doi:10.1029/2001JD001023, 2003.

Portmann, R.W., S. Solomon, R.R. Garcia, L.W. Thomason, L.R. Poole, M.P. McCormick, "Role of aerosol variations in anthropogenic ozone depletion in polar regions," *J. Geophys. Res. 101*, 22,991-23,006, 1996.

Potter, B.E., J.R. Holton, "The Role of Monsoon Convection in the Dehydration of the Lower Tropical Stratosphere," *J. Atmos. Sci. 52*, 1034-1050, 1995.

Randel, W.J., F. Wu, D.J. Gaffen, "Interannual variability of the tropical tropopause derived from radiosonde data and NCEP reanalyses," *J. Geophys. Res. 105*, 15,509-15,523, 2000.

Read, W.G., L. Froidevaux, and J.W. Waters, "Microwave Limb Sounder (MLS) measurements of SO_2 from Mt. Pinatubo volcano," *Geophys. Res. Lett. 20*, 1299-1302, 1993.

Read, W.G., J.W. Waters, L. Froidevaux, D.A. Flower, R.F. Jarnot, D.L. Hartmann, R.S. Harwood, and R.B. Rood, "Upper-tropospheric water vapor from UARS MLS," *Bull. Am. Meteorol. Soc. 76*, 2381, 1995.

Read, W.G, J.W. Waters, D.L. Wu, E.M. Stone, Z. Shippony, A.C. Smedley, C.C. Smallcomb, S. Oltmans, D. Kley, H.G.J. Smit, J.L. Mergenthaler, M.K. Karki, "UARS Microwave Limb Sounder Upper Tropospheric Humidity Measurement: Method and Validation," *J. Geophys. Res. 106*, 32,207, 2001.

Read, W.G., Z. Shippony, W.V. Snyder, "EOS MLS Forward Model Algorithm Theoretical Basis," Jet Propulsion Laboratory Document D-18130**,** Version 1.0, 2004a.

Read, W.G., D.L. Wu, J.W. Waters, H.C. Pumphrey, "A New 147-56 hPa Water Vapor Product from the UARS Microwave Limb Sounder," *J. Geophys. Res. 109*, No. D6, D06111, doi:10.1029/2003JD004366, 2004b.

Read, W.G., D.L. Wu, J.W. Waters, H.C. Pumphrey, "Dehydration in the Tropical Tropopause Layer: Implications from UARS MLS," *J. Geophys. Res. 109*, No. D6, D06110, doi:10.1029/2003JD004056, 2004c.

Reber, C.A., C.E. Trevathan, R.J. McNeal, and M.R. Luther, "The Upper Atmosphere Research Satellite (UARS) mission," *J. Geophys. Res. 98*, 10,643, 1993.

Reichardt, J., A. Ansmann, M. Serwazi, C. Weitkamp, and W. Michaelis, "Unexpectedly low ozone concentration in midlatitude tropospheric ice clouds: a case study," *Geophys. Res. Lett. 23*, 1929, 1996.

Reinsel, G.C., E.C. Weatherhead, G.C. Tiao, A.J. Miller, R.M. Nagatani, D.J. Wuebbles, L.E. Flynn, "On detection of turnaround and recovery in trend for ozone," *J. Geophys. Res. 107*, 10.1029/2001JD000500, 2002.

Rex, M., R.J. Salawitch, M.L. Santee, J.W. Waters, K. Hoppel, R. Bevilacqua, "On the unexplained stratospheric ozone losses during cold Arctic Januaries," *Geophys. Res. Lett. 30*, 1008, doi: 10129/2002GL016008, 2003.

Ricaud, P., J. de La Noe, B.J. Connor, L.Froidevaux, J.W. Waters, R.S. Harwood, I.A. MacKenzie, and G.E. Peckham, "Diurnal variability of mesospheric ozone as measured by the UARS microwave limb sounder instrument: Theoretical and ground-based validations," *J. Geophys. Res. 101*, 10,077, 1996.

Rodgers, C.D., "Retrieval of atmospheric temperature and composition from remote measurements of thermal radiation," *Reviews of Geophysics and Space Physics 14*, 609, 1976.

Rodgers, C.D., "Characterization and error analysis of profiles retrieved from remote sounding measurements," *J. Geophys. Res. 95*, 5587, 1990.

Rosenlof, K.H., S.J. Oltmans, D. Kley, J.M. Russell III, E.W. Chiou., D.G. Johnson, K.K. Kelly, H.A. Michelson, G.E. Nedoluha, E.E. Remsberc, G.C. Toon, M.P. McCormick, "Stratospheric water vapor increases over the past half-century," *Geophys. Res. Lett. 28*, 1195-1198, 2001.

Salby, M.L., "Sampling theory for asynoptic satellite observations. Part I: Space-time spectra, resolution and aliasing," *J. Atmos. Sci. 39*, 2577, 1982.

Sandor, B.J., W.G. Read, J.W. Waters, K.H. Rosenlof, "Seasonal behavior of tropical to midlatitude upper tropospheric water vapor from UARS MLS," *J. Geophys. Res. 103*, 25935-25947, 1998.

Santee, M.L., W.G. Read, J.W. Waters, L. Froidevaux, G.L. Manney, D.A. Flower, R.F. Jarnot, R.S. Harwood, and G.E. Peckham, "Interhemispheric differences in polar stratospheric HNO_3, H_2O, ClO and O_3," *Science 267*, 849, 1995.

Santee, M.L., G.L. Manney, N.J. Livesey, W.G. Read, "Three-dimensional structure and evolution of stratospheric HNO_3 based on UARS Microwave Limb Sounder Measurements," *J. Geophys. Res. 109*, D15306,doi:10.10129/2004JD004578, 2004.

Schwartz, M.J., W.V. Snyder, W.G. Read, "EOS MLS Mesospheric-Specific Polarized Forward Model Algorithm Theoretical Basis Document," Jet Propulsion Laboratory Document D-28534**,** Version 1.0, 2004.

Sherwood, S.C., A.E. Dessler, "A model for transport across the tropical tropopause," *J. Atmos. Sci. 58*, 765-779, 2001.

Schoeberl, M.R., R.S. Stolarski, A.R. Douglass, P.A. Newman, L.R. Lait, and J.W. Waters, "MLS ClO observations and arctic polar vortex temperatures," *Geophys. Res. Lett. 20*, 2861-2854, 1993.

Shindell, D.T., D. Rind, P. Lonergan, "Increased polar stratospheric ozone losses and delayed eventual recovery owing to increasing greenhouse gas concentrations," *Nature 392*, 589-592, 1998.

Shindell, D.T., "Climate and ozone response to increased stratospheric water vapor," *Geophys. Res. Lett. 28*, 1551-1554, 2001.

Shine, K.P., A. Sinha, "Sensitivity of the earth's climate to height-dependent changes in the water vapor mixing ratio," *Nature 354*, 382-384, 1991.

Siegel, P.H., I. Mehdi, R.J. Dengler, J.E. Oswald, A. Pease, T.W. Crowe, W. Bishop, Y. Li, R.J. Mattauch, S. Weinreb, J. East, and T. Lee, "Heterodyne radiometer development for the Earth Observing System Microwave Limb Sounder," in *Infrared and Millimeter-Wave Engineering, SPIE 1874*, 124, 1993.

Smith, C.A., J.D. Haigh, R. Toumi, "Radiative forcing due to trends in stratospheric water vapor," *Geophys. Res. Lett. 28*, 179-182, 2001.

Solomon, S., S. Borrmann, R.R. Garcia, R. Portmann, L. Thomason, L.R. Poole, D. Winker, and M.P. McCormick, "Heterogeneous chlorine chemistry in the tropopause region," *J. Geophys. Res. 102*, 21411, 1997.

Solomon, S., "Stratospheric Ozone Depletion: A Review of Concepts and History," *Rev. Geophys. 37*, 275, 1999.

Spencer, R.W., W.D. Braswell, "How dry is the tropical free troposphere? Implication for global warming theory," *Bull. Amer. Meteor. Soc. 78*, 1097-1106, 1997.

Stachnik, R.A., J.C. Hardy, J.A. Tarsala, J.W. Waters, and N.R. Erickson, "Submillimeterwave heterodyne measurements of stratospheric ClO, HCl, O_3, and HO_2: First results," *Geophys. Res. Lett. 19*, 1931, 1992.

Staehelin, J., N.R.P. Harris, C. Appenzeller, J. Eberhard, "Ozone trends: A review," *Rev. Geophys. 39*, 231-290, 2002.

Subcommittee on Global Change Research, 'Our Changing Planet: The FY99 U.S. Global Change Research Program,' a supplement to the President's Fiscal Year 1999 budget, available from the Global Change Research Information Office User Services, 2250 Pierce Road, University Center MI 48710 (http://www.gcrio.org). Document available on-line at http://www.gcrio.org/ocp99/toc.html, 1998.

Tabazadeh, A., M.L. Santee, M.Y. Danilin, H.C. Pumphrey, P.A. Newman, P.J. Hamill, J.L. Mergenthaler, "Quantifying denitrification and its effect on ozone recovery," *Science 288*, 1407-1411, 2000.

Tabazadeh, A., K. Drdla, M.R. Schoeberl, P. Hamill, O.B. Toon, "Arctic 'ozone hole' in a cold volcanic stratosphere," *Proc. Natl. Acad. Sci. U.S.A. 99*, 2609-2612, 2002.

Thompson, A.M., "The Oxidizing Capacity of Earth's Atmosphere: Probable Past and Future Changes," *Science 256*, 1157-1165, 1992.

Thompson, A.M., K.E. Pickering, D.P. McNamara, M.R. Schoeberl, R.D. Hudson, J.H. Kim, E.V. Browell, V. W. J. H. Kirchhoff, and D. Nganga, "Where did tropospheric ozone over southern Africa and the tropical Atlantic come from in October 1992? Insights from TOMS, GTE TRACE A, and SAFARI 1992," *J. Geophys. Res. 101*, 24278, 1996.

Thompson, D.W.J., and J.M. Wallace, "The Arctic Oscillation signature in the wintertime geopotential height and temperature fields," *Geophys. Res. Lett. 25*, 1297, 1998.

Wagner, P.A., "EOS MLS Level 2 File Description with Data Dictionary," Version 1.43, 2004. (available from the MLS Science Team)

Wang, Y., and D.J. Jacob, "Anthropogenic forcing on tropospheric ozone and OH since preindustrial times," *J. Geophys. Res. 103*, 31123-31135, 1998.

Waters, J.W. J.J. Gustincic, R.K. Kakar, H.K. Roscoe, P.N. Swanson, T.G. Phillips, T. DeGraauw, A.R. Kerr, and R.J. Mattauch, "Aircraft search for millimeter wavelength emission by stratospheric ClO," *J. Geophys. Res. 84,* 6934, 1979.

Waters, J.W., J.C. Hardy, R.F. Jarnot, and H.M. Pickett, "Chlorine monoxide radical, ozone, and hydrogen peroxide: Stratospheric measurements by microwave limb sounding," *Science 214*, 61, 1981.

Waters, J.W., "Microwave Limb Sounding," in *Atmospheric Remote Sensing by Microwave Radiometry* (M.A. Janssen, ed.), chapter 8, New York: John Wiley, 1993.

Waters, J.W., W.G. Read, L. Froidevaux, T.A. Lungu, V.S. Perun, R.A. Stachnik, R.F. Jarnot, R.E. Cofield, E.F. Fishbein, D.A. Flower, J.R. Burke, J.C. Hardy, L.L. Nakamura, B.P. Ridenoure, Z. Shippony, R.P. Thurstans, L.M. Avallone, D.W. Toohey, R.L. deZafra, and D.T. Shindell, "Validation of UARS Microwave Limb Sounder ClO measurements," *J. Geophys. Res. 101*, 10,091, 1996.

Waters, J.W., W.G. Read, L. Froidevaux, R.F. Jarnot, R.E. Cofield, D.A. Flower, G.K. Lau, H.M. Pickett, M.L. Santee, D.L. Wu, M.A. Boyles, J.R. Burke, R.R. Lay, M.S. Loo, N.J. Livesey, T.A. Lungu, G.L. Manney, L.L. Nakamura, V.S. Perun, B.P. Ridenoure, Z. Shippony, P.H. Siegel, R.P. Thurstans, R.S. Harwood, H.C. Pumphrey, M.J. Filipiak, "The UARS and EOS Microwave Limb Sounder Experiments," *J. Atmos. Sci. 56*, 194-218, 1999.

Weinreb, S., P.C. Chao, and W. Copp, "Full Waveguide Band, 90 to 140 GHz MMIC Amplifier Module," *1997 IEEE MTT-S Digest*, 127, 1997.

Wu, D.L., and J.W. Waters, "Gravity-wave-scale temperature fluctuations seen by the UARS MLS," *Geophys. Res. Lett. 23*, 3289, 1996.

Wu, D.L., W.G. Read, A.E. Dessler, S.C. Sherwood, J.H. Jiang, "UARS MLS Cloud Ice Measurements and Implications for H_2O Transport near the Tropopause," J. Atmos. Sci., submitted, 2004.

Wu, D.L., J.H. Jiang, "EOS MLS Algorithm Theoretical Basis for Cloud Measurements," Jet Propulsion Laboratory Document D-19299**,** Version 1.0, 2004.

Yienger, J.J., M. Galanter, T.A. Holloway, M.J. Phadnis, S.K. Guttikunda, G.R. Carmichael, W.J. Moxim, H. Levy II, "The episodic nature of air pollution transport from Asia to North America," *J. Geophys. Res. 105*, 26,931-26,945, 2000.